Abstract

JOYNER, MICHELE LYNN. An Application of a Reduced Order Computational Methodology for Eddy Current Based Nondestructive Evaluation Techniques (Under the direction of H. Thomas Banks)

In the field of nondestructive evaluation, new and improved techniques are constantly being sought to facilitate the detection of hidden corrosion and flaws in structures such as airplanes and pipelines. In this dissertation, we explore the feasibility of detecting such damages by application of an eddy current based technique and reduced order modeling.

We begin by developing a model for a specific eddy current method in which we make some simplifying assumptions reducing the three-dimensional problem to a two-dimensional problem. (We do this for proof-of-concept.) Theoretical results are then presented which establish the existence and uniqueness of solutions as well as continuous dependence of the solution on the parameters which represent the damage. We further discuss theoretical issues concerning the least squares parameter estimation problem used in identifying the geometry of the damage.

To solve the identification problem, an optimization algorithm is employed which requires solving the forward problem numerous times. To implement these methods in a practical setting, the forward algorithm must be solved with extremely fast and accurate solution methods. Therefore in constructing these computational methods, we employ reduced order Proper Orthogonal Decomposition (POD) techniques which allows one to create a set of basis elements spanning a data set consisting of either numerical simulations or experimental data.

We investigate two different approaches in forming the POD approximation, a POD/Galerkin technique and a POD/Interpolation technique. We examine the error in the approximation using one approach versus the other as well as present results of the parameter estimation problem for both techniques.

Finally, results of the parameter estimation problem are given using both simulated data with relative noise added as well as experimental data obtained using a giant magnetoresistive (GMR) sensor. The experimental results are based on successfully using actual experimental data to form the POD basis elements (instead of numerical simulations) thus illustrating the effectiveness of this method on a wide range of applications. In both instances the methods are found to be efficient and robust. Furthermore, the methods were fast; our findings suggest a *significant* reduction in computational time.

AN APPLICATION OF A REDUCED ORDER COMPUTATIONAL METHODOLOGY FOR EDDY CURRENT BASED NONDESTRUCTIVE EVALUATION TECHNIQUES

BY

MICHELE LYNN JOYNER

A DISSERTATION SUBMITTED TO THE GRADUATE FACULTY OF

NORTH CAROLINA STATE UNIVERSITY

IN PARTIAL FULFILLMENT OF THE

REQUIREMENTS FOR THE DEGREE OF

DOCTOR OF PHILOSOPHY

APPLIED MATHEMATICS

COMPUTATIONAL MATHEMATICS CONCENTRATION

RALEIGH

JUNE 2001

APPROVED BY:

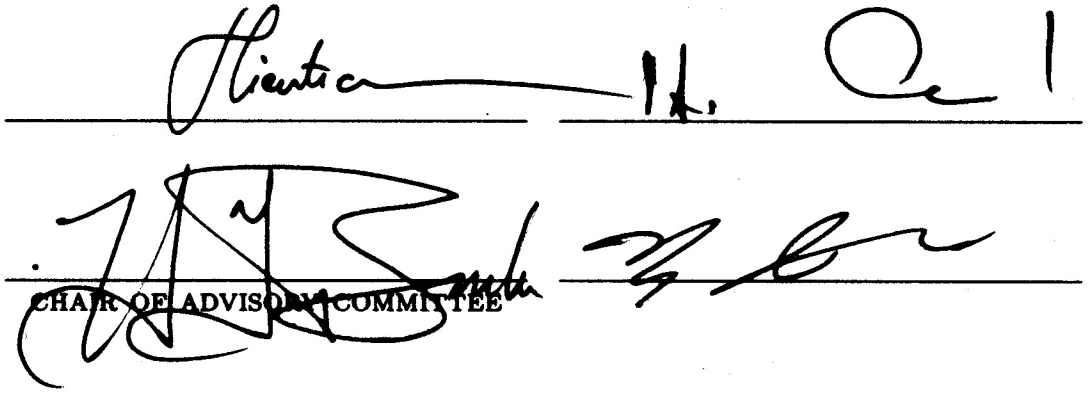

CHAIR OF ADVISORY COMMITTEE

I dedicate this work to my husband, Jason, who has given me his unconditional love and support for these past six years, to my son, Nicholas, who has made my life and work so much more meaningful, and to my parents, Don and Evelyn Meade, and brother, Lee Meade, who believed in me from the start.

Biography

The author was born in Baltimore, Maryland on December 11, 1972 where she spent the first nine years of her life before moving to King, North Carolina where she spent the next three years. At the age of 12, she moved to Bainbridge, Georgia where she graduated from Bainbridge High School in 1990. She then attended Georgia Southern University for two years before transferring to the Georgia Institute of Technology in Atlanta, Georgia. In 1995 she graduated from Georgia Tech with highest honors, receiving a Bachelor of Science degree in Applied Mathematics. In August, 1995, she started attending North Carolina State University where she received her Master of Science in Applied Mathematics in May 1999 and a Doctor of Philosophy in Applied Mathematics, Computational Mathematics Concentration in August, 2001. She has a accepted a position with MIT Lincoln Laboratory in Lexington, Massachusetts.

Acknowledgements

There are many people without whom this dissertation wouldn't have been possible. I would first and foremost like to thank my advisor, Dr. H.T. Banks. He has always been eager and willing to share his expertise with his students and co-workers, and his enthusiasm for his work has been instrumental in sparking my interest in mathematics and research. His influence, both as a mentor and friend, is directly responsible for my current success and for the bright prospects ahead for my professional career. I would like to especially thank him for always believing in me and in my ability as a mathematician and as a person. He and his wife Sue have always had an open door for both me and my family.

Secondly, I would like to thank Dr. Hien Tran who first introduced me to mathematical modeling in the course he co-taught with Dr. Banks. In addition, he was the person who first sought out a summer research project for me under the direction of Dr. Banks. Many thanks also to my other advisory committee members, Dr. Pierre Gremaud who always had an open door, and Dr. Kazufumi Ito for his enthusiasm for my project.

Others besides my committee have been indispensable in my research work. I greatly appreciate the expertise and advice of my collaborators at NASA Langley Research Center, Dr. Bill Winfree and Dr. Buzz Wincheski. They have continually brought insight to the project and were always willing to try something new. Special thanks to them and their colleagues in the collection of the data necessary for a large portion of the research presented in this dissertation.

Financial support has been given through the NASA Langley Graduate Researcher's Program under Grant NGT-1-52196 as well as the Air Force Office of Scientific Research under Grant AFSOR F49620-98-1-0180 and AFSOR F49620-98-1-0430.

I would also like to thank the Center for Research in Scientific Computation, and Department of Mathematics as a whole, for the wonderful program they have built and continue to improve upon. Special thanks goes out to those who were always willing to lend a helping hand: Rory Schnell, Brenda Currin, April Jackson, July Duran, Dianne Hartgrove and Carolyn Gunton.

I am especially thankful to the friends and fellow students who have been with me throughout this long journey. Thanks to Melissa Choi, Julie Raye, Ric del Rosario, Mandy Matthews, Rebecca Segal, Todd and Kristy Coffey, and Mike Jeffries. I would like to give a special thanks to Grant Hargett and Shree Whitaker, who have given me laughter and memories to last a lifetime. I especially want to thank Cammey Cole and Laura Potter for those long summer days studying for prelims, the lunches when we just needed to get away, and for the occasional babysitting duties. Your support in both my academic life and personal life has blessed me and my family tremendously.

Finally, I thank my family for their love, support, and encouragement. To my father-in-law and mother-in law, Harold and Carol Joyner, thank you for believing in me and welcoming me into your family. A special thank you goes out to my brother, Lee Meade, who was always willing to help when things didn't go as smoothly as planned, and to my parents, Don and Evelyn Meade, because there aren't words to express the gratitude I feel for you and your love. I can honestly say that without you, I would not be where I am today. Thank you! And to my son, Nicholas, who is the light of my life. Thank you for all the smiles and hugs that make each day special. Finally, I give my greatest thanks to my husband, Jason, for his never-ending love and for the life we continue to build together. You have been my anchor, always believing in me, supporting me, and especially loving me. Without you, none of this would have been possible.

Table of Contents

List of Figures **ix**

List of Tables **xii**

1 Introduction **1**

2 Model Formulation **5**
2.1 Phasors 8
2.2 Formulation of Forward Problem 10
2.3 Dependence of Magnetic Flux Density on the Damage 17

3 Well-Posedness **19**
3.1 Formation of Integro-Differential Equation 20
3.2 Existence of Weak Solution 22
3.2.1 Existence and Uniqueness with Displacement Current Density Included 23
3.2.2 Existence and Uniqueness with Displacement Current Density Neglected 26
3.3 Continuous Dependence on Parameters 27
3.4 Convergence Results 32

4 Computational Method **36**
4.1 The POD Method 37
4.2 Determination of POD coefficients 40
4.2.1 POD/Galerkin Method 40
4.2.2 POD/Interpolation Method 46
4.2.3 Summary of POD/Galerkin vs. POD/Interpolation Methods . 49
4.3 Optimization Algorithm 50

5 Simulated Results **52**
5.1 Cost Criterion for Simulated Results 52
5.2 Estimating One Parameter 55
5.2.1 Determining the Length of the Damage 55
5.2.2 Determining the Thickness of the Damage 62
5.2.3 Determining the Depth of the Damage 64
5.3 Estimating Two Parameters 70
5.4 Conclusions 74

6 Experimental Results **76**
6.1 Comparison of Experimental Data and Ansoft Simulations 77
6.2 Analysis of the Data at Various Frequencies 82
6.2.1 Depth of Penetration 82
6.2.2 Analysis of Data Using Raw Phase Information 84
6.2.3 Analysis of Data Using "Shifted" Phase Information 89
6.2.4 Analysis of Data Using "Averaged" Phase Information 93
6.3 Estimating the Damage 98
6.3.1 Determining the Length of the Damage 98
6.3.2 Determining the Depth of the Damage 115
6.3.3 Determining the Length *and* Depth of the Damage 118
6.4 Conclusions 120

7 Conclusions and Future Research Directions **124**
7.1 Concluding Remarks 124
7.2 Future Work 126
7.2.1 Collection and Analysis of More Experimental Data 126
7.2.2 A Three-Dimensional Eddy Current Model 127

A The POD/Galerkin vs POD/Interpolation Methods **128**
A.1 The POD/Galerkin Method - Condition of the Linear System 128
A.2 Relative Error Depending on the Method 129
A.2.1 POD/Galerkin Method 129
A.2.2 POD/Interpolation Method 130

B Simulated Results: Estimating Depth **132**
B.1 Estimation of Depth Depending on the Number N of POD Basis Elements Used 132
B.2 Estimation of Depth With 10% Relative Noise 141

C Supplementary Experimental Results **146**
C.1 Determination of Length with Frequency 250Hz 147
C.2 Determination of Length with Frequency 500Hz 148
C.3 Determination of Length with Frequency 1kHz 149
C.4 Determination of Length with Frequency 2kHz 151

List of References **153**

List of Figures

2.1 3-D Schematic of Eddy Current Inspection Process 6
2.2 2-D Schematic of Problem 7
2.3 Illustration of Phasor Notation 10
2.4 Intensity Plot for B_2 for Samples with Various Damages 18
2.5 Magnitude of B_2 Along a Line Located $1mm$ above the Conducting Sheet 18

3.1 Schematic of Quadrilateral 28
3.2 The Area Represented by $\delta\hat{\Omega}$ 29
3.3 Schematic of the Parameters Which Describe the Geometry of the Damage 29

4.1 Finite Element Simulations vs. POD Approximations formed using the POD/Galerkin Method with $N = 1$ and $N = 2$ Basis Elements 44
4.2 Finite Element Simulations vs. POD Approximations formed using the POD/Galerkin Method with $N = 3$ and $N = 4$ Basis Elements 44
4.3 Finite Element Simulations vs. POD Approximations formed using the POD/Galerkin Method with $N = 8$ and $N = 21$ Basis Elements . . . 45
4.4 Finite Element Simulations vs. POD Approximations formed using the POD/Interpolation Method with $N = 1$ and $N = 2$ Basis Elements . 47
4.5 Finite Element Simulations vs. POD Approximations formed using the POD/Interpolation Method with $N = 3$ and $N = 4$ Basis Elements . 48
4.6 Nelder-Mead Algorithm 50

6.1 Experimental Setup 76
6.2 Schematic of the Damaged Layer 77
6.3 Altered Schematic of 2-D Problem 78
6.4 Comparison of Experimental Data and Ansoft Simulations 79
6.5 Initial Lack of Pattern in Experimental Data 81
6.6 Pattern of Experimental Data 82

6.7 Data using Frequency 250Hz with Raw Phase Information at fixed depth $3mm$ 85
6.8 Data using Frequency 500Hz with Raw Phase Information at fixed depth $3mm$ 85
6.9 Data using Frequency 1kHz with Raw Phase Information at fixed depth $3mm$ 86
6.10 Data using Frequency 2kHz with Raw Phase Information at fixed depth $3mm$ 86
6.11 Data using Frequency 1kHz with Raw Phase Information at fixed depth $2mm$ 87
6.12 Data using Frequency 1kHz with Raw Phase Information at fixed depth $1mm$ 87
6.13 Data using Frequency 2kHz with Raw Phase Information at fixed depth $2mm$ 88
6.14 Data using Frequency 2kHz with Raw Phase Information at fixed depth $1mm$ 88
6.15 Comparison of Phase When Using a Frequency of 500Hz vs. 1kHz . . 89
6.16 Schematic of Right Hand Rule 90
6.17 Data using Frequency 250Hz with Shifted Phase Information at fixed depth $3mm$ 91
6.18 Data using Frequency 500Hz with Shifted Phase Information at fixed depth $3mm$ 92
6.19 Data using Frequency 1kHz with Shifted Phase Information at fixed depth $3mm$ 92
6.20 Data using Frequency 2kHz with Shifted Phase Information at fixed depth $3mm$ 93
6.21 Data using Frequency 250Hz with "Averaged" Phase Information at fixed depth $3mm$ 94
6.22 Data using Frequency 500Hz with "Averaged" Phase Information at fixed depth $3mm$ 94
6.23 Data using Frequency 1kHz with "Averaged" Phase Information at fixed depth $3mm$ 95
6.24 Data using Frequency 2kHz with "Averaged" Phase Information at fixed depth $3mm$ 95
6.25 Data using Frequency 250Hz with Shifted *and* Averaged Phase Information at fixed depth $3mm$ 96
6.26 Data using Frequency 500Hz with Shifted *and* Averaged Phase Information at fixed depth $3mm$ 96
6.27 Data using Frequency 1kHz with Shifted *and* Averaged Phase Information at fixed depth $3mm$ 97

6.28 Data using Frequency 2kHz with Shifted *and* Averaged Phase Information at fixed depth $3mm$ 97
6.29 Comparison of POD Approximations and Data at Frequency 500Hz . 99
6.30 Comparison of POD Approximations and Data with Raw Phase Information at Frequency 250Hz 104
6.31 Comparison of POD Approximations and Data with Shifted Phase Information at Frequency 250Hz 104
6.32 Comparison of POD Approximations and Data with "Averaged" Phase Information at Frequency 250Hz 105
6.33 Comparison of POD Approximations and Data with Shifted *and* Averaged Phase Information at Frequency 250Hz 105
6.34 Comparison of POD Approximations and Data with Raw Phase Information at Frequency 500Hz 107
6.35 Comparison of POD Approximations and Data with Shifted Phase Information at Frequency 500Hz 107
6.36 Comparison of POD Approximations and Data with "Averaged" Phase Information at Frequency 500Hz 108
6.37 Comparison of POD Approximations and Data with Shifted *and* Averaged Phase Information at Frequency 500Hz 108
6.38 Comparison of POD Approximations and Data with Raw Phase Information at Frequency 1kHz 111
6.39 Comparison of POD Approximations and Data with Shifted Phase Information at Frequency 1kHz 111
6.40 Comparison of POD Approximations and Data with "Averaged" Phase Information at Frequency 1kHz 112
6.41 Comparison of POD Approximations and Data with Shifted and Averaged Phase Information at Frequency 1kHz 112
6.42 Comparison of POD Approximations and Data with Raw Phase Information at Frequency 2kHz 114
6.43 Comparison of POD Approximations and Data with Shifted Phase Information at Frequency 2kHz 114
6.44 Comparison of POD Approximations and Data with "Averaged" Phase Information at Frequency 2kHz 115
6.45 Comparison of POD Approximations and Data with Shifted and Averaged Phase Information at Frequency 2kHz 115

List of Tables

4.1 Energy Captured with N Basis Elements using Snapshots of A while Varying Length 42
4.2 Energy Captured with N Basis Elements using Snapshots of B_2 while Varying Length 43
4.3 Condition Number of Linear System for POD/Galerkin Coefficients . 45
4.4 Relative Error of POD/Galerkin Approximations 46
4.5 Relative Error of POD/Interpolation Approximations 48

5.1 Determination of Length $l^* = 1.3mm$ Using POD/Galerkin Method with 10% Relative Noise Added 58
5.2 Determination of Length $l^* = 2.5mm$ Using POD/Galerkin Method with 10% Relative Noise Added 59
5.3 Determination of Length $l^* = 5mm$ Using POD/Galerkin Method with 10% Relative Noise Added 59
5.4 Determination of Length $l^* = 1.3mm$ Using the POD/Interpolation Method with 10% Relative Noise Added 60
5.5 Determination of Length $l^* = 2.5mm$ Using the POD/Interpolation Method with 10% Relative Noise Added 61
5.6 Determination of Length $l^* = 5mm$ Using the POD/Interpolation Method with 10% Relative Noise Added 61
5.7 Energy Captured with N Basis Elements using Snapshots of A while Varying Thickness 62
5.8 Energy Captured with N Basis Elements using Snapshots of B_2 while Varying Thickness 63
5.9 Determination of Thickness $h^* = 1.3mm$ Using POD/Interpolation Method with 10% Relative Noise Added 63
5.10 Energy Captured with N Basis Elements using Snapshots of A while Varying Depth 64
5.11 Energy Captured with N Basis Elements using Snapshots of B_2 while Varying Depth 65

5.12 Determination of Depth with No Noise Added Using $N = 5$ 66
5.13 Determination of Depth with No Noise Added Using $N = 10$ 67
5.14 Determination of Depth $d^* = 3mm$ with 10% Relative Noise Added Using $N = 5$ 69
5.15 Determination of Depth $d^* = 8mm$ with 10% Relative Noise Added Using $N = 5$ 69
5.16 Determination of Depth $d^* = 11mm$ with 10% Relative Noise Added Using $N = 5$ 70
5.17 Energy Captured with N Basis Elements using Snapshots of B_2 while Varying Length *and* Depth 71
5.18 Determination of Depth *and* Length Simultaneously 72
5.19 Relative Error In Determination of Depth *and* Length Simultaneously 72
5.20 Determination of Depth $d^* = 2mm$ and Length $l^* = 1cm$ Simultaneously with 10% Relative Noise Added to Data 73
5.21 Determination of Depth $d^* = 4mm$ and Length $l^* = 2cm$ Simultaneously with 10% Relative Noise Added to Data 73
5.22 Determination of Depth $d^* = 6mm$ and Length $l^* = 3cm$ Simultaneously with 10% Relative Noise Added to Data 74

6.1 Depth of Penetration for Aluminum Alloy 2024 83
6.2 Determination of Length using (6.1) at a Depth of $2mm$ with Frequency 500Hz 99
6.3 Determination of Length at a Frequency of 250Hz Using (6.11) 103
6.4 Determination of Length at a Frequency of 250Hz Using (6.13) 103
6.5 Determination of Length at a Frequency of 500Hz Using (6.11) 106
6.6 Determination of Length at a Frequency of 500Hz Using (6.13) 106
6.7 Determination of Length at a Frequency of 1kHz using (6.15) 110
6.8 Determination of Length at a Frequency of 1kHz using (6.16) 110
6.9 Determination of Length at a Frequency of 2kHz using (6.12) 113
6.10 Determination of Length at a Frequency of 2kHz using (6.14) 113
6.11 Determination of Depth with Fixed Length $1.0cm$ 116
6.12 Determination of Depth with Fixed Length $1.5cm$ 117
6.13 Determination of Depth with Fixed Length $2.0cm$ 117
6.14 Determination of Depth *and* Length Simultaneously with Frequency 500Hz 119
6.15 Relative Error when Determining Depth *and* Length Simultaneously with Frequency 500Hz 119
6.16 Determination of Depth *and* Length Simultaneously with Frequency 1kHz 119

6.17 Relative Error when Determining Depth *and* Length Simultaneously with Frequency 1kHz 120

A.1 Condition Numbers of Linear System for POD/Galerkin Coefficients of POD Approximation for $N = 1$ to $N = 21$ 129
A.2 Relative Error of POD/Galerkin Approximations 130
A.3 Relative Error of POD/Interpolation Approximations 131

B.1 Determination of Depth $d^* = 1mm$ with No Noise 132
B.2 Determination of Depth $d^* = 2mm$ with No Noise 133
B.3 Determination of Depth $d^* = 3mm$ with No Noise 133
B.4 Determination of Depth $d^* = 4mm$ with No Noise 134
B.5 Determination of Depth $d^* = 5mm$ with No Noise 134
B.6 Determination of Depth $d^* = 6mm$ with No Noise 135
B.7 Determination of Depth $d^* = 7mm$ with No Noise 135
B.8 Determination of Depth $d^* = 8mm$ with No Noise 136
B.9 Determination of Depth $d^* = 9mm$ with No Noise 136
B.10 Determination of Depth $d^* = 10mm$ with No Noise 137
B.11 Determination of Depth $d^* = 11mm$ with No Noise 137
B.12 Determination of Depth $d^* = 12mm$ with No Noise 138
B.13 Determination of Depth $d^* = 13mm$ with No Noise 138
B.14 Determination of Depth $d^* = 14mm$ with No Noise 139
B.15 Determination of Depth $d^* = 15mm$ with No Noise 139
B.16 Determination of Depth $d^* = 16mm$ with No Noise 140
B.17 Determination of Depth $d^* = 17mm$ with No Noise 140
B.18 Determination of Depth $d^* = 1mm$ with 10% Relative Noise Added Using $N = 5$ 141
B.19 Determination of Depth $d^* = 2mm$ with 10% Relative Noise Added Using $N = 5$ 141
B.20 Determination of Depth $d^* = 4mm$ with 10% Relative Noise Added Using $N = 5$ 142
B.21 Determination of Depth $d^* = 5mm$ with 10% Relative Noise Added Using $N = 5$ 142
B.22 Determination of Depth $d^* = 6mm$ with 10% Relative Noise Added Using $N = 5$ 143
B.23 Determination of Depth $d^* = 7mm$ with 10% Relative Noise Added Using $N = 5$ 143
B.24 Determination of Depth $d^* = 9mm$ with 10% Relative Noise Added Using $N = 5$ 144

B.25 Determination of Depth $d^* = 10mm$ with 10% Relative Noise Added Using $N = 5$ 144
B.26 Determination of Depth $d^* = 12mm$ with 10% Relative Noise Added Using $N = 5$ 145

C.1 Determination of Length at a Frequency of 250Hz Using (C.1) 147
C.2 Determination of Length at a Frequency of 250Hz Using (C.2) 148
C.3 Determination of Length at a Frequency of 500Hz Using (C.1) 148
C.4 Determination of Length at a Frequency of 500Hz Using (C.2) 149
C.5 Determination of Length at a Frequency of 1kHz Using (C.1) 149
C.6 Determination of Length at a Frequency of 1kHz Using (C.2) 150
C.7 Determination of Length at a Frequency of 1kHz Using Imaginary Part of (C.1) 150
C.8 Determination of Length at a Frequency of 1kHz Using Imaginary Part of (C.2) 151
C.9 Determination of Length at a Frequency of 2kHz Using (C.1) 151
C.10 Determination of Length at a Frequency of 2kHz Using (C.2) 152

Chapter 1

Introduction

Nondestructive evaluation (NDE) is the process of examining a material or article without impairing its future usefulness. NDE is sometimes referred to as nondestructive testing (NDT) or nondestructive inspection (NDI), although there may be subtle differences in their definitions depending on the author. For the purposes of this dissertation, however, we will use the terminology interchangeably.

The process of examining a material using nondestructive evaluation techniques has been around for decades and is becoming increasingly important as technology continually advances. According to the American Society of Nondestructive Testing, the term NDT includes many methods that can: (i) detect internal or external imperfections, (ii) determine structure, composition, or material properties, or (iii) measure geometric characteristics. Some typical structures or products inspected through the use of NDE technology are airplanes, motor vehicles, pipelines, bridges, trains, and power stations.

From an industrial point of view, nondestructive testing is used to evaluate the state or quality of a material to determine whether a material or part will continue to perform its intended function or whether it is at risk of failure. Furthermore, since examination of the material using NDE techniques does not destroy the product's future usefulness, NDE can be used throughout all phases of a product's life, including

design, assembly, quality control and maintenance. As a result, these techniques provide many benefits including improvement of product reliability, reduced failures and prevention of accidents, more efficient product designs, and control in manufacturing processes [9, 40, 42]. This in turn leads to economic benefits such as reduced cost and better customer satisfaction resulting directly in increased production.

Nondestructive evaluation techniques can be broken down into seven main categories: (i) visual inspection, (ii) liquid penetration inspection, (iii) radiography and radiation testing, (iv) electromagnetic testing, (v) acoustic emission monitoring, (vi) magnetic methods, and (vii) ultrasonic testing. Each of these categories is broad, containing within them several specific testing techniques. The choice of an appropriate NDE technique depends on the specific application. We will not go into detail about the benefits and limitations of each method, but will instead refer the reader to [9, 11, 20, 22, 40, 42] for a thorough discussion. In this paper, we will only focus on a particular electromagnetic testing method, called the eddy current method.

Eddy currents are currents found in any conducting material which is subject to a time-varying magnetic field. They are useful for NDE purposes, because if a flaw is present within a conducting material, the flow of the eddy currents will be disrupted in some manner. From this disruption, and its effect on the magnetic flux density, we can discern information about the damage or defect within the material. A thorough analysis of eddy currents and their behavior can be found in [46].

Since eddy currents are only found in a conducting material, the use of eddy current methods is limited; however, these methods have been proven extremely useful when examining pipeline structures and aging aircrafts. There are many devices and eddy current techniques in use today including the self-nulling eddy current probe [52] along with conformal mapping techniques [53], the magneto-optic/eddy current imager [18, 47] in conjunction with eddy current imaging [19, 21], the SQUID (Superconducting Quantum Interference Device) through the use of either injected current methods or induced eddy current methods [13, 15, 24, 39, 41, 51] and the GMR (Giant Magnetoresistive) sensor based on the self-nulling probe design [54, 55]. Each of these

instruments have unique features, making some instruments easier to use than others or more practical depending on the circumstances. Some of the instruments provide images of the damage, while others provide quantitative data. In this dissertation, we wish to estimate a damage or flaw within a material using quantitative data taken by an appropriate instrument. However, instruments providing images of the damage may give us valuable *a priori* information about the defect, allowing us to obtain a more accurate estimate of the damage.

To this end, we first analyze a specific implementation of the eddy current method and develop a model describing the behavior of the magnetic flux density as a relationship to the total current in Chapter 2. As a consequence, we will be able to obtain information about the damage from the relationship between the disruption in the eddy current and the resulting magnetic flux density.

Chapter 3 provides well-posedness results for the derived model. We first argue the existence and uniqueness of the weak solution and following arguments similar to those in [5], we show the solution depends continuously on the parameters which identify the damage. Furthermore, we provide theoretical results for the parameter estimation problem.

The parameter estimation problem is formulated using a least squares criterion in which we want to estimate the parameters describing the damage based on the magnetic flux density detected by a given instrument. Although standard numerical approximations are sufficient for the parameter identification problem, these methods are extremely time consuming. Therefore, in Chapter 4 we introduce a reduced order computational method based on Karhunen-Loeve or Proper Orthogonal Decomposition (POD) approximation techniques. Recently these techniques have been successfully used in reduced order methodologies for feedback control design [2, 3, 14, 27, 34] as well as open loop control design [38]. Here we propose for the first time the use of such techniques in electromagnetic based damage detection problems. The only other reference (to our knowledge) in which POD reduced order model techniques are used in conjunction with inverse problems is [49] in which the authors seek

to reconstruct distributed conductivities from surface voltage measurements in the classical electrical impedance tomography problem.

Finally, in Chapter 5, we present simulated results based on the proposed methodology and in Chapter 6 we summarize the estimation of damages when using experimental data obtained from a GMR sensor. We then conclude with some final remarks and prospects for future work.

Chapter 2

Model Formulation

In this chapter, we develop a model based on the eddy current method for nondestructive evaluation. The model describes the relationship between the magnetic flux density and total current from which we hope to discern information about the integrity of the material structure (which we will call a sample) we're examining. As discussed in Chapter 1, eddy currents are currents found in any conducting material subjected to some time-varying magnetic field and can be induced in a variety of ways. In this dissertation, we limit our discussion to only one implementation: we examine the process of inducing eddy currents within a sample by placing a thin conducting sheet carrying a uniform current above the sample. The current within the sheet produces a magnetic field perpendicular to it that in turn produces eddy currents within the sample. The presence of a flaw within the sample causes a disruption in the flow of the eddy currents and this disruption manifests itself in the magnetic flux density which can be measured by a device placed above the conducting sheet. A schematic of the inspection process is shown in Figure 2.1.

By assuming uniformity in the direction of the current flow in the conducting sheet (labeled the negative z direction, denoting the coordinate for the width of the sample), we are able to reduce the three-dimensional setup described above to a two-dimensional problem in the xy plane, where x denotes the coordinate of the length of the sample and y denotes the coordinate of the thickness of the sample. We

make this simplifying assumption for proof-of-concept, to illustrate the feasibility of reconstructing the geometry of a damage. In addition, in order to disregard boundary effects along the edges of the sample, we assume the sample and conducting sheet are infinitely long, i.e., they are infinite in the x direction. If the conducting sheet and sample are not of infinite extent, we have to take into account the discontinuities in the current flow at the boundaries. Furthermore, the damage (which we shall refer to as a "crack") is assumed to be rectangular in shape and centered along the length of the sample (along the x direction).

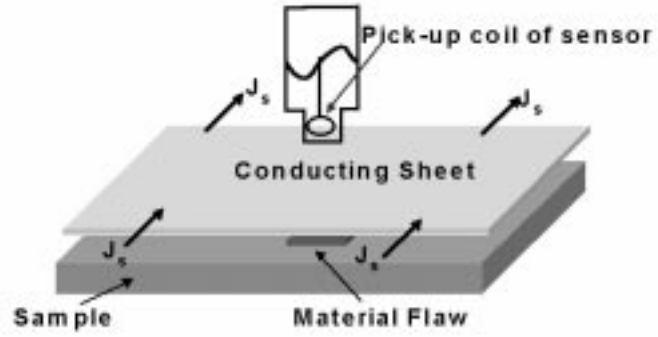

Figure 2.1: 3-D Schematic of Eddy Current Inspection Process

For computational purposes, we examine a finite "window" of the overall problem, which is called the computational domain Ω. In choosing the boundaries of the computational domain along the length of the sample (x boundaries), we recall that the sample and conducting sheet are assumed to be of infinite extent. Therefore, we can arbitrarily choose these boundaries by assigning evenly symmetric boundary conditions to account for the infinite extent of the materials. However, since the damage is centered along the length of the sample, we need to only consider half of the sample for computational purposes. The other half will behave in the same manner. Therefore, we choose the left boundary to be located at the center of the crack in the x direction, labeled $x = 0$, with the crack symmetric through the yz plane at $x = 0$, and the right boundary is chosen at $x = 50mm$. The y boundaries, or top and bottom boundaries, are at $y = -35mm$ and $y = 35mm$ and are assumed

to be far enough away from the sample that the field is approximately zero at these boundaries. Indeed, the magnetic flux density at a point is inversely proportional to the distance between the source current and the point. Hence the field tends to zero as the distance from the source current or conducting sheet increases. A schematic of the resulting two-dimensional problem is depicted in Fig. 2.2 where it is assumed that the sample (which is $20mm$ thick) is composed of aluminum and the conducting sheet (which is $0.1mm$ thick) is made up of copper. Thus the computational domain which we will use for the purposes of developing the model can be explicitly defined by

$$\Omega = \{(x, y, z) \in \mathbb{R}^3 : 0mm \leq x \leq 50mm, -35mm \leq y \leq 35mm\}.$$

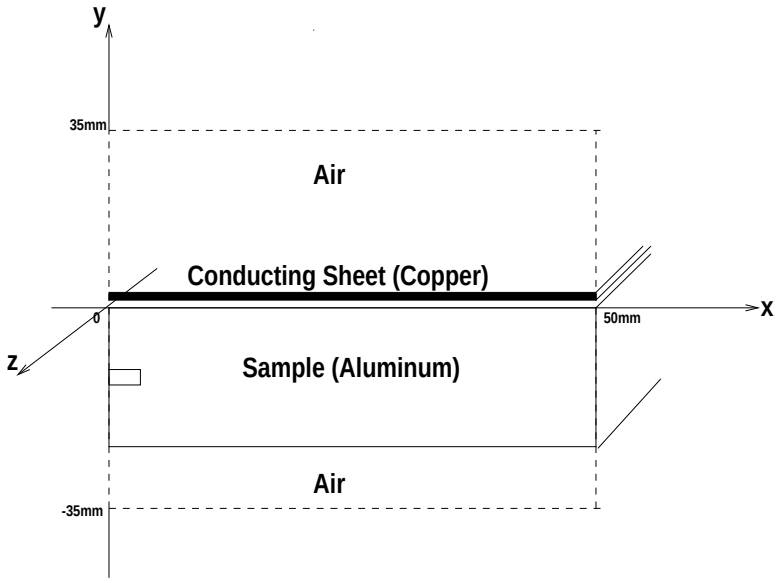

Figure 2.2: 2-D Schematic of Problem

Although certain simplifications are made in the two-dimensional case, the two-dimensional analysis may be relevant to special three-dimensional cases. In a "true" three-dimensional case, the sample will be of finite length (finite in the x direction). However, if the crack is located "far enough" away from the boundaries of the sample in the x direction, we can assume the boundary effects are not sufficiently significant to effect the measurements taken by the sensor. In this case, the infinite extent of

the sample in the test problem will fairly accurately portray the finite sample in the three-dimensional case. Similarly, in the two-dimensional test problem, we assume the sample along with the damage or crack to have an infinite width. Again, in the three-dimensional process, the crack will have a finite width. If data is taken by scanning along the length of the sample on a line fixed at a certain height and the line upon which we are scanning is fixed in the z direction (along the width of the sample) so that the line is "far enough" away from the edges of the crack in the z direction (along the width of the crack), we may still be able to use the two-dimensional analysis to determine the feasibility of identifying length, thickness and depth of the crack in the sample with appropriate sensor data. Thus, the development of the two-dimensional model and computational methods for the model will allow us to determine feasibility of the proposed methods before considering a "true" three-dimensional design.

2.1 Phasors

We begin the development of the model by introducing a mathematical tool, called phasors, which is typically used in the field of electromagnetic nondestructive evaluation whenever periodic interrogating inputs are employed. As mentioned in the previous section, a conducting sheet (copper in our example) carrying a uniform current is placed above the sample to induce eddy currents within the sample. Without loss of generality, we assume the source current has the form

$$\tilde{\tilde{\mathbf{J}}}_s = J_s cos(\omega t)\hat{\mathbf{k}} = J_s Re(e^{i\omega t})\hat{\mathbf{k}}$$

where J_s is the magnitude of the source current. This current produces a magnetic field $\tilde{\tilde{\mathbf{H}}}(x, y, t)$ described by Maxwell's equations. At the surface of the sample, the magnetic field has the same time dependence as the source current,

$$\tilde{\tilde{\mathbf{H}}}(x, y, t) = \tilde{\mathbf{H}}(x, y)cos(\omega t).$$

However, as the magnetic field penetrates into the sample, a phase lag occurs due to the finite conductivity of the sample (aluminum in our example). In other words, the

magnetic field takes the form

$$\tilde{\tilde{\mathbf{H}}}(x, y, t) = \tilde{\mathbf{H}}(x, y)cos(\omega t + \theta(x, y)), \tag{2.1}$$

where the term $\theta(x, y)$ takes into account the depth of penetration. Hence, $\tilde{\mathbf{H}}(x, y)$ is a vector field quantity which keeps track of the magnitude and direction of $\tilde{\tilde{\mathbf{H}}}$ at each point in space while $\theta(x, y)$ denotes the phase shift from the original cosine wave at the same point in space. If we were to use the expression in (2.1) involving the cosine function in the derivation of the model, whenever differentiation or integration of the function is involved, we would introduce both cosine and sine functions into the problem. As a result, we would be required to combine sine and cosine functions which is a tedious process. Instead, since the only quantities of interest in (2.1) are $\tilde{\mathbf{H}}(x, y)$ and $\theta(x, y)$, we can use vector phasors to keep track of these quantities, denoting the magnitude, direction, and phase lag which simplify the expressions.

A phasor ([1, 12]) is a complex quantity which completely defines the magnitude and phase shift for $\tilde{\tilde{\mathbf{H}}}(x, y, t)$. Figure 2.3 illustrates how the magnitude and phase shift are defined through the complex number. Given a complex number, the point represented by the complex number can be drawn in the complex plane with a vector from the origin to the point.

Then the magnitude of $\tilde{\tilde{\mathbf{H}}}$ is represented by the radius of the circle made by the vector, and the phase shift is given by the angle the complex vector makes with the real axis. Thus, the vector phasor $\mathbf{H}$ and the explicit time dependent field $\tilde{\tilde{\mathbf{H}}}(x, y, t)$ are related in the following way

$$\tilde{\tilde{\mathbf{H}}}(x, y, t) = Re(\mathbf{H}(x, y)e^{i\omega t}) = Im(\mathbf{H}(x, y)e^{i(\omega t + \pi/2)}) \tag{2.2}$$

in which all of the phase information and direction is captured in the complex vector phasor $\mathbf{H}$. For this reason, in the remainder of the paper we will assume no explicit time dependence in the fields examined, but instead consider the fields to be complex vector phasors, denoted $\mathbf{H}$, $\mathbf{B}$, etc, and account for the time dependence of the fields through phase shifts contained in the phasors.

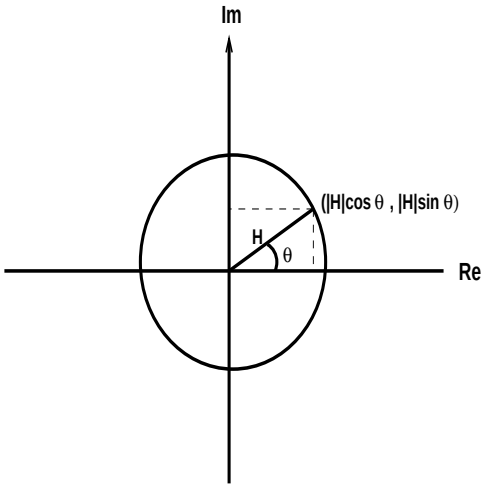

Figure 2.3: Illustration of Phasor Notation

2.2 Formulation of Forward Problem

The underlying theory for electromagnetic testing of all kinds relies on Maxwell's equations as the basis for describing electromagnetic phenomena. Maxwell's equations, as derived from first principles (e.g., Coulomb's law, the Lorentz transformation and relativity theory - see [16]), is given by

$$\nabla \cdot \tilde{\tilde{\mathbf{B}}} = 0, \tag{2.3}$$

$$\nabla \cdot \tilde{\tilde{\mathbf{D}}} = \rho, \tag{2.4}$$

$$\nabla \times \tilde{\tilde{\mathbf{E}}} = -\frac{\partial}{\partial t}\tilde{\tilde{\mathbf{B}}}, \tag{2.5}$$

and

$$\nabla \times \tilde{\tilde{\mathbf{H}}} = \tilde{\tilde{\mathbf{J}}} + \frac{\partial}{\partial t}\tilde{\tilde{\mathbf{D}}} \tag{2.6}$$

where

$\tilde{\tilde{\mathbf{B}}}$ is the magnetic flux density in T,

$\tilde{\tilde{\mathbf{D}}}$ is the electric displacement in C/m^2,

$\tilde{\tilde{\mathbf{E}}}$ is the electric field intensity in V/m,

$\tilde{\tilde{\mathbf{H}}}$ is the magnetic field intensity in A/m,

$\tilde{\tilde{\mathbf{J}}}$ is the current density in A/m^2, and

ρ is the electric charge density in C/m^3.

However, since we are expressing the various fields in terms of phasors which depend on space coordinates but not explicitly on time, we want to express time-dependent Maxwell's equations in terms of phasors as well. To examine the relationship between the explicit time-dependent Maxwell's equations and Maxwell's equations in terms of phasors, we examine the relationship in (2.2). From (2.2), the time derivative for $\tilde{\tilde{\mathbf{H}}}(x, y, t)$ (and other fields similarly) is given by

$$\frac{\partial}{\partial t}\tilde{\tilde{\mathbf{H}}}(x, y, t) = \omega Re(i\mathbf{H}(x, y)e^{i\omega t}) = \omega Im(i\mathbf{H}(x, y)e^{i(\omega t+\pi/2)}). \tag{2.7}$$

Substituting the appropriate form of (2.2) and (2.7) into (2.3) - (2.6), we obtain the completely equivalent phasor form of Maxwell's equations

$$\nabla \cdot \mathbf{B} = 0, \tag{2.8}$$

$$\nabla \cdot \mathbf{D} = \rho, \tag{2.9}$$

$$\nabla \times \mathbf{E} = -i\omega\mathbf{B}, \tag{2.10}$$

and

$$\nabla \times \mathbf{H} = \mathbf{J} + i\omega\mathbf{D}. \tag{2.11}$$

These are the equations we will use as the basis for all of the following derivations.

We first would like to make a couple of notes regarding (2.8) - (2.11). To begin with, our system is considered to be electrically neutral, i.e., the internal electric charge density ρ equals zero. Secondly, by examining the conductivity, σ, of aluminum and copper ($\sigma_{al} = 3.72 \times 10^7 S/m$ and $\sigma_{cu} = 5.8 \times 10^7 S/m$ respectively) and by using Ohm's law

$$\mathbf{J} = \sigma\mathbf{E}, \tag{2.12}$$

we can argue $\mathbf{J} \approx 10^7\mathbf{E}$. On the other hand, the constitutive law

$$\mathbf{D} = \epsilon\mathbf{E}, \tag{2.13}$$

where ϵ is the electric permittivity ($\epsilon \approx \epsilon_0 \approx \frac{1}{36\pi} \times 10^{-7} F/m$), indicates $\mathbf{D} \approx 10^{-10}\mathbf{E}$. Therefore, for the source frequencies we consider within the scope of this dissertation (f_s = 60Hz - 2kHz), $\omega\mathbf{D} < 10^{-6}\mathbf{E}$ where $\omega = 2\pi f_s$ is the angular frequency. Consequently, in the sample and conducting sheet $\mathbf{J} >> \omega\mathbf{D}$ which implies we could assume $\omega\mathbf{D} \approx 0$ in both the sample and conducting sheet in (2.11). In other words, the term $\omega\mathbf{D}$ is only significant in the air. However, both the literature and the finite element software employed in the computations (Ansoft Maxwell 2D Field Simulator) neglect the displacement current density in the air as well [30, 31, 32, 33, 50]. In our initial computational efforts, we formulated the problem both including as well as neglecting the displacement current density and compared the corresponding solutions. Our findings agreed with the literature; there was no discernible change in the solution when the displacement current density was ignored. However, the presence of this term *does* alter the theoretical results slightly (see Chapter 3) and for this reason, we choose to include this term in the derivation of the model.

We use the Ansoft finite element solver ([1]) in our computational efforts; therefore, we continue our derivation in the same manner as done in Ansoft by introducing a magnetic vector potential $\mathbf{A}$. Based upon (2.8) and vector null identities, $\mathbf{B}$ can be represented as the curl of a vector potential $\mathbf{A}$ (called the magnetic vector potential),

$$\mathbf{B} = \nabla \times \mathbf{A}. \tag{2.14}$$

Therefore, given the magnetic vector potential $\mathbf{A}$, both the magnetic field $\mathbf{H}$ and magnetic flux density $\mathbf{B}$ can be derived. Accordingly, we want to combine Maxwell's equations to obtain equations in conjunction with boundary conditions which completely determine the behavior of the magnetic vector potential $\mathbf{A}$ in Ω.

Using the identity $\mathbf{B} = \nabla \times \mathbf{A}$ in (2.10), we have

$$\nabla \times \mathbf{E} = -i\omega(\nabla \times \mathbf{A}) \quad \text{or} \quad \nabla \times (\mathbf{E} + i\omega\mathbf{A}) = 0.$$

Again, using vector null identities, $\nabla \times (\mathbf{E} + i\omega\mathbf{A}) = 0$ implies $\mathbf{E} + i\omega\mathbf{A}$ can be written as the gradient of a scalar potential, denoted by ϕ. As a result,

$$\mathbf{E} = -i\omega\mathbf{A} - \nabla\phi. \tag{2.15}$$

Finally, we can use (2.11) and (2.15) in conjunction with Ohm's law (2.12), the constitutive law given by (2.13) and the constitutive law $\mathbf{H} = \frac{1}{\mu}\mathbf{B}$ (μ is the magnetic permeability in H/m), to obtain

$$\nabla \times \left(\frac{1}{\mu}\nabla \times \mathbf{A}\right) = (\sigma + i\omega\epsilon)(-i\omega\mathbf{A} - \nabla\phi) \quad \forall x, y \in \Omega. \tag{2.16}$$

In the above equality, the right side represents the total current density made up of the source current density, eddy current density, and displacement current density. The source current density $\mathbf{J}_s$ is due to differences in electric potential; therefore, $\mathbf{J}_s$ is represented by the term $-\sigma\nabla\phi$. The term $-i\omega\sigma\mathbf{A}$ represents the eddy current density $\mathbf{J}_e$ produced by a time-varying magnetic field. Finally, the displacement current density $\mathbf{J}_d$ due to time-varying electric fields is given by the term $i\omega\epsilon(-i\omega\mathbf{A} - \nabla\phi)$.

Since (2.16) contains two unknowns, $\mathbf{A}$ and ϕ, we need an additional equation to uniquely determine solutions of the system. In the literature ([10],[12, pp. 327-328], [23, pp. 219-221], [33]), the uncoupling of the equations is usually accomplished by exploiting the arbitrariness involved in the definition of $\mathbf{A}$. By Helmholtz's theorem, a vector field is determined within an additive constant if both its divergence and its curl are specified everywhere ([12, p. 63]); although the curl of $\mathbf{A}$ is determined according to (2.14), the divergence of $\mathbf{A}$ is still arbitrary. Therefore, a "gauge" is normally chosen which specifies the divergence of $\mathbf{A}$.

In time-varying problems a Lorentz gauge is often imposed, because it allows the equations to be decoupled. However, there are different Lorentz gauges which are more or less acceptable depending on the problem. In our formulation of the problem, called the A-ϕ formulation, an appropriate choice for the Lorentz gauge depends on whether or not the displacement current density is included or neglected. When the displacement current density is included, the Lorentz condition given by

$$\nabla \cdot \mathbf{A} + i\omega\mu\epsilon\phi = 0, \tag{2.17}$$

allows one to decouple the equations [12, 23]. However, if the displacement current density is neglected, this condition is no longer an appropriate choice and instead one

should normally use

$$\nabla \cdot \mathbf{A} + \mu\sigma\phi = 0 \tag{2.18}$$

to decouple the equations [10, 33].

On the other hand, based upon the geometry in our test problem, $\nabla \cdot \mathbf{A} = 0$ is naturally imposed. This follows since the only nonzero component of $\mathbf{A}$ is A_3, the component of $\mathbf{A}$ in the z direction (the direction of the current density $\mathbf{J}$). Therefore, $\nabla \cdot \mathbf{A} = \frac{\partial A_3}{\partial z} = 0$ by uniformity in the z direction. Indeed, this is the Coulomb gauge [23, pp. 221-222].

Since the Coulomb gauge is naturally imposed, it provides no additional information in our problem. It is therefore necessary to use an integral constraint to obtain a second equation relating the magnetic vector potential $\mathbf{A}$ to the scalar potential ϕ, or more precisely $\nabla\phi$. For the integral constraint, we take the relationship

$$I = \int_S \mathbf{J}_t \cdot \mathbf{n} da = \int_S (\sigma + i\omega\epsilon)(-i\omega\mathbf{A} - \nabla\phi) \cdot \mathbf{n} da \tag{2.19}$$

where I is the total measurable current flowing in a conducting surface (S) and $\mathbf{J}_t$ is the total current density within the conducting surface. Since we are only able to control the current flowing in the conducting sheet, we use the equivalent equation in the conducting sheet

$$I_{cs} = \int_{cs} \mathbf{J}_t \cdot \mathbf{n} da = \int_{cs} (\sigma + i\omega\epsilon)(-i\omega\mathbf{A} - \nabla\phi) \cdot \mathbf{n} da \tag{2.20}$$

where I_{cs} is the total current flowing in the conducting sheet (cs). However, since (2.20) only provides a relationship between $\mathbf{A}$ and $\nabla\phi$ in the conducting sheet, we still need either a relationship between the potentials or a condition on one of the potentials in both the sample and air.

Using a few underlying assumptions, we can justify $\nabla\phi \equiv 0$ in the sample. We explore two different arguments which in the end result in this conclusion. One approach is to examine the source current density term caused by changes in potential across the material given by $\mathbf{J}_s = -\sigma\nabla\phi$. Since we only apply a current, and hence effectively a potential, across the conducting sheet, the source current density (due

to changes in potential) only exists in the conducting sheet. Consequently, $\mathbf{J}_s = -\sigma\nabla\phi = 0$ in the sample. Since the conductivity of aluminum σ_{al} does not equal zero, $\nabla\phi$ must be identically zero for all (x, y) in the sample. A second alternative is to assume the sample is a passive conductor modeling a short circuit (which is done in Ansoft). In general, a passive conductor is a conductor which has no component of source current (as discussed above). In other words, the only currents considered to be flowing in a passive conductor are eddy currents and displacement currents (when considered). In addition, a short circuit conductor is treated as a conducting ring which loops back on itself. In this case, using concepts of a closed circuit, the change in potential across the loop is zero [1, 48], i.e.,

$$\nabla\phi = 0 \quad \forall(x, y) \in sample. \tag{2.21}$$

The only other region left to consider is the air. When the displacement current density is ignored, it is not necessary to require an additional constraint on $\nabla\phi$ in the air since (2.16) reduces to

$$\nabla \times \left(\frac{1}{\mu}\nabla \times \mathbf{A}\right) = 0 \quad \forall(x, y) \in air. \tag{2.22}$$

However, we will make an intuitive argument for why $\nabla\phi$ should be taken to be zero in the air as well. We use an argument similar to that one used for the sample. The source current density, as discussed previously, is only present in the conducting sheet and hence not in the air. However, by examining the equations alone, this does not give us any knew information. It simply states that $J_s = -\sigma\nabla\phi$ must equal zero in the air which is already true since σ is identically zero in the air. On the other hand, we can intuitively argue that the source current density is due to changes in potential, and, therefore, if no source current density is present in a region, there should be no change in potential in that region as well. Using this reasoning, we take $\nabla\phi = 0$ in the air. Although not explicitly stated in the technical notes for Ansoft Maxwell 2D Field Simulator ([1]), the software effectively uses $\nabla\phi = 0$ in the air when estimating the displacement current density given the approximate finite element solution A

determined by (2.20) and (2.21). (In the actual calculations produced by the Ansoft software, displacement current density is ignored totally.)

Therefore, combining all the above we have two coupled equations (2.16) and (2.20) and the additional condition $\nabla\phi = 0$ for points (x, y) in the sample and air. Using these equations, the magnetic vector potential $\mathbf{A}$ can be uniquely determined if appropriate boundary conditions on $\mathbf{A}$ are specified.

Recall that we assume evenly symmetric x boundaries due to the symmetry of the crack and the infinite extent of the materials. In other words on the x boundaries, we assume the fields on both sides of the boundary oscillate in the same direction. To account for the even symmetry, we assign Neumann boundary conditions to these boundaries. In a similar manner, we assume the y boundaries are "sufficiently far" away from the sample and scanning area to not effect the overall measurements. We mentioned previously that as one moves farther away from the sample and conducting sheet, the magnetic vector potential $\mathbf{A}$ tends to zero. Thus, on the y boundaries, we assign Dirichlet boundary conditions to indicate the boundary is "sufficiently far" away from the materials so that $\mathbf{A} \approx \mathbf{0}$. Therefore, the magnetic vector potential $\mathbf{A}$ is determined according to

$$\nabla \times \left(\frac{1}{\mu(x,y)} \nabla \times \mathbf{A}(x,y) \right) = (\sigma(x,y) + i\omega\epsilon(x,y))(-i\omega\mathbf{A}(x,y) - \nabla\phi) \quad \forall x, y \in \Omega, \tag{2.23}$$

$$I_{cs} = \int_{cs} \mathbf{J}_t \cdot \mathbf{n} da = \int_{cs} (\sigma(x,y) + i\omega\epsilon(x,y))(-i\omega\mathbf{A}(x,y) - \nabla\phi) \cdot \mathbf{n} da \tag{2.24}$$

and

$$\nabla\phi = 0 \quad \forall x, y \in \Omega \setminus cs \tag{2.25}$$

with

$$\begin{aligned} \mathbf{A}(x,-35) &= 0 = \mathbf{A}(x,35) \\ \nabla\mathbf{A} \cdot \mathbf{n}|_{(0,y)} &= 0 = \nabla\mathbf{A} \cdot \mathbf{n}|_{(50,y)}. \end{aligned}$$

2.3 Dependence of Magnetic Flux Density on the Damage

In the previous section we derived the boundary value problem for the magnetic vector potential $\mathbf{A}$. Now, we explore how the magnetic vector potential, and hence the magnetic flux density, varies with damages in the sample. The damage affects the magnetic vector potential in (2.23) mostly through the conductivity, σ. In fact, $\sigma = \sigma(x, y)$ is given by

$$\sigma(x,y) = \begin{cases} \sigma_{cu} &= 5.8 \times 10^7 \ S/m & \text{for } (x,y) \in cs \\ \sigma_{al} &= 3.72 \times 10^7 \ S/m & \text{for } (x,y) \in sample \\ \sigma_{air} &= 0 \ S/m & \text{for } (x,y) \in air \end{cases}$$

Therefore, when a damage is present, there is a sudden change in conductivity at the edges of the crack; the conductivity changes from a factor of 10^7 S/m to 0 S/m. This sudden change in conductivity effects the magnetic vector potential through (2.23) and (2.24). Thus, the magnetic flux density detected by the sensor is also altered.

Figure 2.4 displays two simulated color intensity plots of the variation in the perpendicular component B_2 of the magnetic flux density as a function of the length of a damage within the sample when the thickness of the damage is fixed at $2mm$ and the depth is fixed at $9mm$ below the surface. The first plot in Figure 2.4 shows the variation in B_2 when there is a damage of length $1mm$ compared to the second plot in Figure 2.4 when the damage has a length of $4mm$. The variation in B_2 is largest around the edges of the damage; however, there is a slight variation which should be able to be detected by a sensor scanning along a line above the conducting sheet. By looking at the magnetic flux density data similar to that depicted in Figure 2.4 along a single line $1mm$ above the conducting sheet, we obtain the plot in Figure 2.5. This gives an indication of the type of data the sensor would obtain when scanning along a line. As depicted in Figure 2.5, there is a definite pattern in the magnitude of the magnetic flux density as a function of the length of the damage within the sample.

This suggests that if a sensor is sensitive enough to detect the variation in the data, we should be able to discern information about the damage from the data taken.

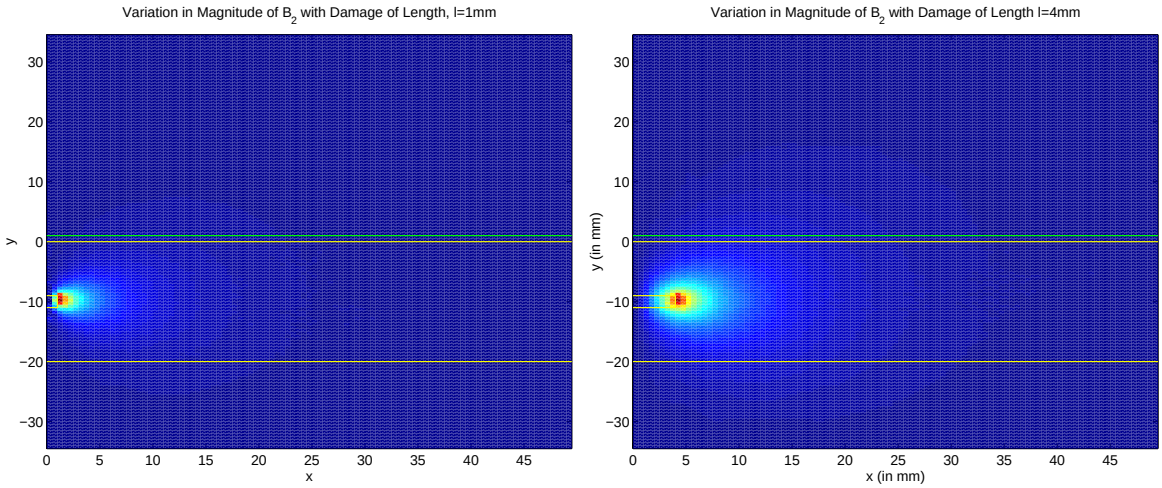

Figure 2.4: Intensity Plots for B_2: The first plot is for a sample containing a damage with length $1mm$ while the second plot is for a sample containing a damage with length $4mm$ (thickness of the damage is fixed at $2mm$ and depth at $9mm$)

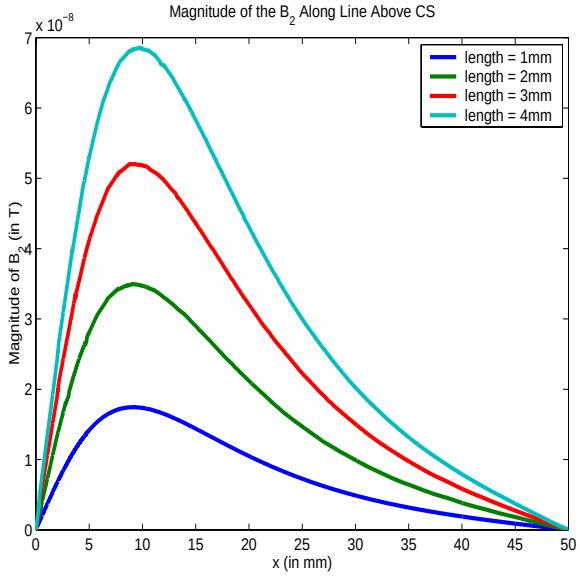

Figure 2.5: Magnitude of B_2 Along a Line Located $1mm$ above the Conducting Sheet for Several Lengths of Damage

Chapter 3

Well-Posedness

In Chapter 2 we developed a model for the magnetic vector potential $\mathbf{A}$ given a source current I_{cs}. The boundary value problem is given in terms of two unknowns $\mathbf{A}$ and ϕ satisfying (2.23) and (2.24) with the additional condition given by (2.25) which uniquely determines the solution when coupled with appropriate boundary conditions. We begin this chapter by combining (2.23), (2.24), and (2.25) into an integro-differential equation as done in [30, 31, 33]. Using the integro-differential equation, we formulate the variational form of the boundary value problem which will be used for exploring theoretical questions as well as provide a basis for numerical considerations in Chapter 4.

In this chapter, we consider ideas such as well-posedness, including the existence and uniqueness of the weak solution of the boundary value problem. We noted in Chapter 2 that for computational purposes it is not necessary for the displacement current density to be included in the model; however, including versus neglecting the displacement current density *does* alter theoretical results. As a result, we present arguments for existence and uniqueness of the weak solution for both cases (when the displacement current density is included as well as when it is neglected). Furthermore, as discussed in Section 2.3 the magnetic vector potential is effected by a damage within the sample through the conductivity $\sigma(x, y)$; therefore, in Section 3.3, we consider a general damage and define a vector of parameters to represent this damage.

Given this representation, we establish continuous dependence of the solution on the parameters. Finally, we end the chapter by considering convergence results for the parameter estimation problem.

3.1 Formation of Integro-Differential Equation

Recall from Section 2.2, the boundary value problem describing the system (including displacement currents) is given by

$$\nabla \times \left(\frac{1}{\mu(x,y)} \nabla \times \mathbf{A}(x,y) \right) = (\sigma(x,y) + i\omega\epsilon(x,y))(-i\omega\mathbf{A}(x,y) - \nabla\phi) \quad \forall x, y \in \Omega, \tag{3.1}$$

$$I_{cs} = \int_{cs} \mathbf{J}_t \cdot \mathbf{n} da = \int_{cs} (\sigma(x,y) + i\omega\epsilon(x,y))(-i\omega\mathbf{A}(x,y) - \nabla\phi) \cdot \mathbf{n} da, \tag{3.2}$$

and

$$\nabla\phi = 0 \quad \forall x, y \in \Omega \setminus cs \tag{3.3}$$

with

$$\begin{array}{rcccl} \mathbf{A}(x, -35mm) & = & 0 & = & \mathbf{A}(x, 35mm) \\ \nabla\mathbf{A} \cdot \mathbf{n}|_{(0mm,y)} & = & 0 & = & \nabla\mathbf{A} \cdot \mathbf{n}|_{(50mm,y)} \end{array}.$$

To reduce the above system to an integro-differential equation, we need to observe that for the two-dimensional problem, $\nabla\phi$ is piecewise constant. From (2.15), $\nabla\phi = -\mathbf{E}(x,y) - i\omega\mathbf{A}(x,y)$. Since both $\mathbf{E}$ and $\mathbf{A}$ vary as functions of only x and y, we can write $\nabla\phi = g(x,y)$ for some function g (not dependent on z). Furthermore, as discussed in the previous chapter, both $\mathbf{E}$ and $\mathbf{A}$ have only one nonzero component, E_3 and A_3 respectively. Consequently, since $\nabla\phi$ is given by

$$\nabla\phi = \frac{\partial\phi}{\partial x}\hat{i} + \frac{\partial\phi}{\partial y}\hat{j} + \frac{\partial\phi}{\partial z}\hat{k},$$

we have $\frac{\partial\phi}{\partial x} = 0 = \frac{\partial\phi}{\partial y}$ by component equality. This implies $\phi = \phi(z)$ is a function of z which readily gives $\nabla\phi = \frac{\partial\phi}{\partial z} = f(z)$ for some function f. The only way both of these conditions can be satisfied is if $\nabla\phi$ is constant or piecewise constant. We can

immediately see that $\nabla\phi$ is piecewise constant since $\nabla\phi$ satisfies (3.2) for all (x, y) in the conducting sheet but $\nabla\phi \equiv 0$ elsewhere.

Since $\nabla\phi$ is constant throughout the conducting sheet, we can use (3.2) to solve for $\nabla\phi$ in terms of $\mathbf{A}$ for all (x, y) in the conducting sheet. For simplicity, let's denote $\mathbf{A}$ by its nonzero component A and $\nabla\phi$ by $K(x, y)$, the nonzero component of $\nabla\phi$ where we note that K is not a "true" function of x and y but instead a piecewise constant function in which the point (x, y) determines the constant:

$$K(x,y) = \begin{cases} 0 & \text{for} \quad (x,y) \in \Omega \setminus cs \\ K_{cs} & \text{for} \quad (x,y) \in cs \end{cases}$$

(K_{cs} represents the value of K in the conducting sheet).

Using $\nabla\phi = K_{cs}$ in (3.2), we have

$$\begin{aligned} I_{cs} &= \int_{cs} (\sigma(x,y) + i\omega\epsilon(x,y))(-i\omega A(x,y) - K_{cs}) \cdot n da \\ &= \int_{cs} (\sigma_{cu} + i\omega\epsilon_{cu})(-i\omega A(x,y) - K_{cs}) \cdot n da \\ &= \int_{0.9mm}^{1mm} \int_{0mm}^{50mm} (\sigma_{cu} + i\omega\epsilon_{cu})(-i\omega A(x,y) - K_{cs}) dx dy \end{aligned}$$

where σ_{cu} is the conductivity of the conducting sheet (copper). Separating terms and integrating, we obtain

$$K_{cs} = -\frac{I_{cs}}{\Delta_{cs}(\sigma_{cu} + i\omega\epsilon_{cu})} - \frac{i\omega}{\Delta_{cs}} \int_{0.9mm}^{1mm} \int_{0mm}^{50mm} A(x,y) dx dy \tag{3.4}$$

where $\Delta_{cs} = 5 \times 10^{-6} m^2$ is the cross-sectional surface area (i.e., in the xy plane) of the conducting sheet. Therefore, $K(x, y)$ is defined by

$$K(x,y) = \begin{cases} 0 & \text{for} \quad (x,y) \in \Omega \setminus cs \\ -\frac{I_{cs}}{\Delta_{cs}(\sigma_{cu} + i\omega\epsilon_{cu})} - \frac{i\omega}{\Delta_{cs}} \int_{cs} A da & \text{for} \quad (x,y) \in cs \end{cases}. \tag{3.5}$$

Substituting (3.5) into (3.1), where $\nabla\phi = K(x, y)$, we have a boundary value problem in terms of A alone (simplifying the left side of (3.1)):

$$-\left(\frac{\partial^2 A(x,y)}{\partial x^2} + \frac{\partial^2 A(x,y)}{\partial y^2}\right) + \mu(x,y)(\sigma(x,y) + i\omega\epsilon(x,y))(i\omega A(x,y) + K(x,y)) = 0, \tag{3.6}$$

with

$$\begin{aligned} A(x,-35mm) &= 0 = A(x,35mm), \\ \tfrac{\partial A}{\partial x}(0mm,y) &= 0 = \tfrac{\partial A}{\partial x}(50mm,y). \end{aligned}$$

3.2 Existence of Weak Solution

In this section we consider the existence and uniqueness of a weak solution to (3.6) on a general domain given by

$$\tilde{\Omega} = \{(x,y,z) \in \mathbb{R}^3 : x_{min} \leq x \leq x_{max}, y_{min} \leq y \leq y_{max}\}$$

for which our test problem is a specific example. Then, let $H = L_2(\tilde{\Omega})$ and $V = \{\psi \in H^1(\tilde{\Omega}) | \psi(x,y_{min}) = 0 = \psi(x,y_{max})\}$ where we use the standard Sobolev space notation, $H^1(\tilde{\Omega}) = \{\psi \in L^2(\tilde{\Omega}) : \nabla\psi \in L^2(\tilde{\Omega})\}$ and note that we interpret pointwise evaluation of functions (along the boundary and elsewhere) in terms of a trace operator for which we suppress notation throughout this thesis [17]. We denote by $\langle \phi, \psi \rangle \equiv \int_{\tilde{\Omega}} \phi\overline{\psi} da$ the standard inner product in H and $\langle \phi, \psi \rangle_V \equiv \int_{\tilde{\Omega}} \nabla\phi \cdot \overline{\nabla\psi} da$ the (H^1-equivalent) inner product in V.

Then using integration by parts together with natural boundary conditions and imposed conditions on test functions $\psi \in V$, the variational form of (3.6) is given by

$$\left(\langle \frac{\partial A}{\partial x}, \frac{\partial \psi}{\partial x} \rangle + \langle \frac{\partial A}{\partial y}, \frac{\partial \psi}{\partial y} \rangle \right) + \langle i\omega\mu(\sigma + i\omega\epsilon)A, \psi \rangle + \langle \mu(\sigma + i\omega\epsilon)K, \psi \rangle = 0 \qquad (3.7)$$

or more precisely

$$\langle \nabla A, \nabla\psi \rangle + \langle \beta_1 A, \psi \rangle + \beta_2 \int_{cs} A da \int_{cs} \overline{\psi} da = \int_{cs} f\overline{\psi} da. \qquad (3.8)$$

where $\beta_1 = i\omega\mu(\sigma + i\omega\epsilon)$, $\beta_2 = -\frac{i\omega\mu_{cu}(\sigma_{cu} + i\omega\epsilon_{cu})}{\Delta_{cs}}$, and $f = \frac{\mu_{cu} I_{cs}}{\Delta_{cs}}$.

We note that this is the variational form when the displacement current density is *included*. In this section we consider the existence and uniqueness of the solution A to (3.8) as well as its equivalent formulation when the displacement current density is neglected. We consider this in the context of a Gelfand triple setting $V \hookrightarrow H \simeq H^* \hookrightarrow V^*$. We have that the embedding $V \hookrightarrow H$ is dense and continuous with

$$|\psi|_H \leq k|\psi|_V \quad \text{for all } \psi \in V. \qquad (3.9)$$

where the norm in V will be denoted by $|\cdot|_V$ and $|\cdot|$ will denote the norm in H for the rest of this section.

3.2.1 Existence and Uniqueness with Displacement Current Density Included

We define a sesquilinear form $B : V \times V \to \mathbb{C}$ by

$$B(\phi,\psi) = \langle \nabla\phi, \nabla\psi\rangle + \langle \beta_1\phi, \psi\rangle + \beta_2 \int_{cs} \phi da \int_{cs} \overline{\psi} da. \tag{3.10}$$

Then (3.8) can be written as

$$B(\phi,\psi) = \int_{cs} f\overline{\psi} da. \tag{3.11}$$

We intend to prove B is V-continuous and for certain frequencies is V-elliptic. We will then invoke the Lax-Milgram theorem to prove the existence and uniqueness of the weak solution A to (3.8).

Lemma 3.2.1 *B is V-continuous, i.e., there exists some constant c_1 such that*

$$|B(\phi,\psi)| \le c_1 |\phi|_V |\psi|_V. \tag{3.12}$$

Proof: Using the triangle inequality, Cauchy-Schwartz inequality, properties of L^1, Holder's inequality and (3.9), we have

$$\begin{aligned}
|B(\phi,\psi)| &= |\langle \nabla\phi, \nabla\psi\rangle + \langle \beta_1\phi, \psi\rangle + \beta_2 \textstyle\int_{cs} \phi da \int_{cs} \overline{\psi} da| \\
&\le |\langle \nabla\phi, \nabla\psi\rangle| + |\langle \beta_1\phi, \psi\rangle| + |\beta_2 \textstyle\int_{cs} \phi da \int_{cs} \overline{\psi} da| \\
&= |\langle \phi, \psi\rangle_V| + |\langle \beta_1\phi, \psi\rangle| + |\beta_2 \textstyle\int_{cs} \phi da \int_{cs} \overline{\psi} da| \\
&\le |\phi|_V |\psi|_V + |\beta_1|_\infty |\phi||\psi| + |\beta_2 \textstyle\int_{cs} \phi da \int_{cs} \overline{\psi} da| \\
&\le |\phi|_V |\psi|_V + |\beta_1|_\infty |\phi||\psi| + |\beta_2| \textstyle\int_{cs} |\phi| da \int_{cs} |\overline{\psi}| da \\
&\le |\phi|_V |\psi|_V + |\beta_1|_\infty |\phi||\psi| + |\beta_2| \textstyle\int_{\Omega} |\phi| da \int_{\Omega} |\psi| da \\
&= |\phi|_V |\psi|_V + |\beta_1|_\infty |\phi||\psi| + |\beta_2| |\phi|_{L^1(\Omega)} |\psi|_{L^1(\Omega)} \\
&\le |\phi|_V |\psi|_V + |\beta_1|_\infty |\phi||\psi| + |1|^2 |\beta_2| |\phi||\psi| \\
&\le |\phi|_V |\psi|_V + k^2 |\beta_1|_\infty |\phi|_V |\psi|_V + k^2 |1|^2 |\beta_2| |\phi|_V |\psi|_V \\
&= (1 + k^2 |\beta_1|_\infty + k^2 |1|^2 |\beta_2|) |\phi|_V |\psi|_V.
\end{aligned}$$

Let $c_1 = 1 + k^2|\beta_1|_\infty + k^2|1|^2|\beta_2|$. Then

$$|B(\phi,\psi)| \leq c_1|\phi|_V|\psi|_V.$$

Lemma 3.2.2 *There exists $\mathcal{F} = \mathcal{F}(\mu,\epsilon,\tilde{\Omega})$ such that for $f_s < \mathcal{F}(\mu,\epsilon,\tilde{\Omega})$, there exists a constant $c_2 > 0$ such that B satisfies*

$$|B(\phi,\phi)| \geq c_2|\phi|_V^2. \tag{3.13}$$

Proof: By (3.10) and the definition of β_1 and β_2

$$\begin{aligned} ReB(\phi,\phi) &= \langle\nabla\phi,\nabla\phi\rangle - \omega^2\langle\mu\epsilon\phi,\phi\rangle + \tfrac{\omega^2\mu_{cu}\epsilon_{cu}}{\Delta_{cs}}\int_{cs}\phi da\int_{cs}\overline{\phi}da \\ &= \langle\nabla\phi,\nabla\phi\rangle - \omega^2\langle\mu\epsilon\phi,\phi\rangle + \tfrac{\omega^2\mu_{cu}\epsilon_{cu}}{\Delta_{cs}}|\int_{cs}\phi da|^2. \end{aligned}$$

Therefore,

$$\begin{aligned} ReB(\phi,\phi) &\geq \langle\nabla\phi,\nabla\phi\rangle - \omega^2\langle\mu\epsilon\phi,\phi\rangle \\ &\geq \langle\nabla\phi,\nabla\phi\rangle - \omega^2|\mu\epsilon|_\infty|\phi|^2. \end{aligned}$$

Denoting $a = max(|y_{min}|,|y_{max}|)$, we have $|y| \leq a$. Hence for $\phi \in V$,

$$\begin{aligned} |\phi|^2 &= \int_{\tilde{\Omega}} 1\cdot\phi\overline{\phi}da \\ &= \int_{x_{min}}^{x_{max}}\int_{y_{min}}^{y_{max}} 1\cdot\phi\overline{\phi}dydx \\ &= -\int_{\tilde{\Omega}} y\tfrac{\partial\phi}{\partial y}\overline{\phi}da - \int_{\tilde{\Omega}} y\tfrac{\partial\overline{\phi}}{\partial y}\phi da + \int_{x_{min}}^{x_{max}} y\phi\overline{\phi}|_{y_{min}}^{y_{max}}dx \\ &= -\langle y\tfrac{\partial\phi}{\partial y},\phi\rangle - \langle y\phi,\tfrac{\partial\phi}{\partial y}\rangle \\ &\leq |\langle y\tfrac{\partial\phi}{\partial y},\phi\rangle| + |\langle y\phi,\tfrac{\partial\phi}{\partial y}\rangle| \\ &\leq 2a|\phi||\nabla\phi| \\ &\leq \tfrac{2a}{4\gamma}|\phi|^2 + 2a\gamma|\nabla\phi|^2 \\ &= \tfrac{2a}{4\gamma}|\phi|^2 + 2a\gamma|\phi|_V^2. \end{aligned}$$

Thus,

$$\left(1 - \frac{2a}{4\gamma}\right)|\phi|^2 \leq 2a\gamma|\phi|_V^2$$

which gives us

$$|\phi|_V^2 - \left(1 - \frac{2a}{4\gamma}\right)|\phi|^2 \geq (1-2a\gamma)|\phi|_V^2.$$

We want to choose $0 < \gamma < \frac{1}{2a}$ such that

$$1 - \frac{2a}{4\gamma} = \omega^2 |\mu\epsilon|_\infty$$

or

$$\gamma = \frac{2a}{4(1 - \omega^2 |\mu\epsilon|_\infty)}.$$

In order to satisfy conditions on γ, an initial source frequency must be chosen such that

$$\omega < \sqrt{\frac{1 - a^2}{|\mu\epsilon|_\infty}}$$

or

$$f_s < \frac{1}{2\pi}\sqrt{\frac{1 - a^2}{|\mu\epsilon|_\infty}}$$

where $\omega = 2\pi f_s$. Let $\mathcal{F} = \mathcal{F}(\mu, \epsilon, \tilde{\Omega}) = \frac{1}{2\pi}\sqrt{\frac{1-a^2}{|\mu\epsilon|_\infty}}$, then for $f_s < \mathcal{F}$,

$$ReB(\phi, \phi) \geq |\phi|_V^2 - \omega^2 |\mu\epsilon|_\infty |\phi|^2 \geq c_2 |\phi|_V^2$$

with $c_2 = 1 - 2a\gamma > 0$.

We note that for our test problem, $\mu \approx \mu_0 = 4\pi \times 10^{-7}$, $\epsilon \approx \epsilon_0 \approx \frac{1}{36\pi} \times 10^{-7}$ and the term a discussed in the proof is given by $a = 3.5 \times 10^{-2}$. Hence, $\mathcal{F} \approx 4.77$ MHz. All of our computational results use source frequencies $f_s < 2kHz$. Furthermore, frequencies much larger than these are not appropriate for this type of eddy current problem.

A consequence of the Lax-Milgram theorem, as discussed in [56, pp. 271-275], gives an existence and uniqueness theorem for solutions:

Theorem 3.2.1 *Let $V \hookrightarrow H \hookrightarrow V^*$ be a Gelfand triple. Let $B : V \times V \to \mathbb{C}$ satisfy:*

(A1) $|B(\phi, \psi)| \leq c_1 |\phi|_V |\psi|_V$ *for all* $\phi, \psi \in V$,

(A2) $|B(\phi, \phi)| \geq c_2 |\phi|_V^2$ *for all* $\phi \in V$,.

Then there exists an operator $L : V \to V^*$ given by

$$B(\phi, \psi) = \langle L\phi, \psi \rangle_{V^*,V}, \quad \phi, \psi \in V \tag{3.14}$$

such that $L : V \to V^*$ is a linear topological isomorphism between the spaces V and V^*, and for the norms we have

$$|L| \leq c_1, \quad |L^{-1}| \leq \frac{1}{c_2}. \tag{3.15}$$

Put otherwise, the weak equation

$$L\phi = f, \quad f \in V^*, \tag{3.16}$$

interpreted as

$$B(\phi, \psi) = \langle f, \psi \rangle \quad \textit{for all } \psi \in V,$$

possesses for each $f \in V^*$ a unique solution $\phi \in V$, and this solution depends continuously on f.

Theorem 3.2.1 and Lemmas 3.2.1 and 3.2.2 readily give

Theorem 3.2.2 *There exists $\mathcal{F} = \mathcal{F}(\mu, \epsilon, \tilde{\Omega})$ such that for $f_s < \mathcal{F}(\mu, \epsilon, \tilde{\Omega})$, there exists a unique weak solution A to (3.8).*

3.2.2 Existence and Uniqueness with Displacement Current Density Neglected

If the displacement current density is ignored, the variational form is given by

$$\langle \nabla A, \nabla \psi \rangle + \langle \tilde{\beta}_1 A, \psi \rangle + \tilde{\beta}_2 \int_{cs} A da \int_{cs} \overline{\psi} da, = \int_{cs} f \overline{\psi} da \tag{3.17}$$

where the coefficients $\tilde{\beta}_1 = i\omega\mu\sigma$ and $\tilde{\beta}_2 = -\frac{i\omega\mu_{cu}\sigma_{cu}}{\Delta_{cs}}$. We define a new sesquilinear form $\tilde{B}$ by

$$\tilde{B}(\phi, \psi) = \langle \nabla \phi, \nabla \psi \rangle + \langle \tilde{\beta}_1 \phi, \psi \rangle + \tilde{\beta}_2 \int_{cs} \phi da \int_{cs} \overline{\psi} da. \tag{3.18}$$

Then following the same arguments in Lemma 3.2.1 and replacing β_1 and β_2 with $\tilde{\beta}_1$ and $\tilde{\beta}_2$ respectively, we have the following lemma.

Lemma 3.2.3 *$\tilde{B}$ is V-continuous, i.e., there exists some constant $\tilde{c}_1$ such that*

$$|\tilde{B}(\phi,\psi)| \leq \tilde{c}_1 |\phi|_V |\psi|_V. \tag{3.19}$$

Furthermore, we can now prove $\tilde{B}$ is globally V-elliptic.

Lemma 3.2.4 *$\tilde{B}$ satisfies*

$$|\tilde{B}(\phi,\phi)| \geq |\phi|_V^2. \tag{3.20}$$

Proof: By (3.18) and the definition of $\tilde{\beta}_1$ and $\tilde{\beta}_2$

$$Re\tilde{B}(\phi,\phi) = \langle \nabla\phi, \nabla\phi \rangle.$$

Therefore,

$$|\tilde{B}(\phi,\phi)| \geq Re\tilde{B}(\phi,\phi) = |\phi|_V^2.$$

which gives us the desired result.

Consequently, Lemmas 3.2.3 and 3.2.4 together with Theorem 3.2.1 give us Theorem 3.2.3.

Theorem 3.2.3 *There exists a unique weak solution A to (3.17).*

3.3 Continuous Dependence on Parameters

In Section 2.3, we briefly discussed the dependence of the magnetic vector potential (and hence the magnetic flux density) on the damage within the sample, giving graphical illustrations of variation in the field as a function of the damage. In this section, we give theoretical results showing the solution A to (3.8) depends continuously on the parameters representing the damage which will also give us a basis for convergence results in the next section.

We begin by considering a general representation of a damage and define a parameter to represent this damage. Although we only consider rectangular damages centered along the length of the sample in our computational efforts, we will allow for

any four sided polygon or quadrilateral in the theory. We will then relate our specific problem to the more general theory considered here.

Any quadrilateral can be represented by its four corners as depicted in Figure 3.1. Therefore, we let $\tilde{\mathbf{q}} \equiv [(x_1, y_1), (x_2, y_2), (x_3, y_3), (x_4, y_4)]$ be a vector in $\mathbb{R}^4 \times \mathbb{R}^2$ or equivalently $\mathbb{R}^8$ which represents the quadrilateral. We denote by $\tilde{Q}_{ad}$ the set of admissible parameters $\tilde{\mathbf{q}}$ where it is assumed $\tilde{Q}_{ad}$ is a compact subset of $\mathbb{R}^8$. We note that it is possible to pick $\tilde{Q}_{ad}$ to be compact since the damage is restricted to being within a sample of finite length and thickness. We also allow for the case in which no damage is present and represent this case by "collapsing" the quadrilateral into a single point (with zero area), i.e, we define $\tilde{\mathbf{q}}$ as a vector of identical points.

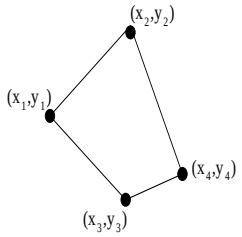

Figure 3.1: Schematic of Quadrilateral

Then for any two damages given by parameters $\hat{\mathbf{q}}$ and $\tilde{\mathbf{q}}$ in $\tilde{Q}_{ad}$, let

$$\tilde{d}(\hat{\mathbf{q}}, \tilde{\mathbf{q}}) = ||\hat{\mathbf{q}} - \tilde{\mathbf{q}}|| = \left[(\hat{x}_1 - x_1)^2 + (\hat{y}_1 - y_1)^2 + ... + (\hat{x}_4 - x_4)^2 + (\hat{y}_4 - y_4)^2\right]^{1/2} \tag{3.21}$$

to be the standard Euclidean norm in $\mathbb{R}^8$. We denote by $\delta\hat{\Omega}$ (Figure 3.2) the points in Ω which are either in the damage represented by $\hat{\mathbf{q}}$ or $\tilde{\mathbf{q}}$ but which are not in both. In other words, let $\Omega_{\hat{\mathbf{q}}}$ represent the points (x, y) in Ω within the damage given by $\hat{\mathbf{q}}$ and $\Omega_{\tilde{\mathbf{q}}}$ the points (x, y) in Ω within the damage given by $\tilde{\mathbf{q}}$. Then $\delta\hat{\Omega} = \Omega_{\hat{\mathbf{q}}} \cup \Omega_{\tilde{\mathbf{q}}} - \Omega_{\hat{\mathbf{q}}} \cap \Omega_{\tilde{\mathbf{q}}}$. The area of $\delta\hat{\Omega}$ is directly related to the distance between parameters $\hat{\mathbf{q}}$ and $\tilde{\mathbf{q}}$. Indeed, $\tilde{d}(\hat{\mathbf{q}}, \tilde{\mathbf{q}}) \to 0$ if and only if $\tilde{x}_1 \to x_1$, $\tilde{y}_1 \to y_1$, ..., $\tilde{x}_4 \to x_4$, $\tilde{y}_4 \to y_4$, i.e., the four corners of the two damages approach one another. Therefore, $\tilde{d}(\hat{\mathbf{q}}, \tilde{\mathbf{q}}) \to 0$ implies $\delta\hat{\Omega} \to \emptyset$ and hence the area of $\delta\hat{\Omega} \to 0$.

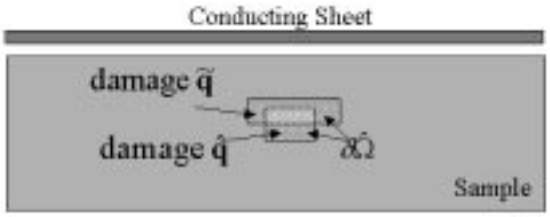

Figure 3.2: The Area Represented by $\delta\hat{\Omega}$

To relate this terminology to the computational examples we present in the rest of this dissertation, the only damages we consider computationally are those rectangular in shape and centered along the length of the axis. We only take into account half of the damage such that the left boundary of the portion we consider is located at $x = 0$ in the xy plane. Therefore, the only variation in the damage is in its length l, thickness h and depth d (Figure 3.3).

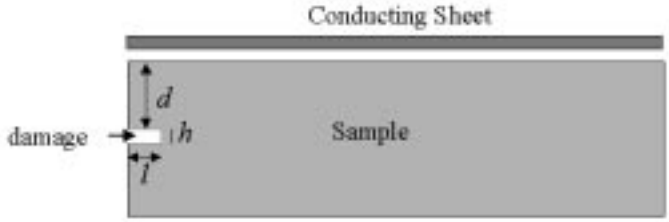

Figure 3.3: Schematic of the Parameters Which Describe the Geometry of the Damage

We let $\mathbf{q}$ be a parameter representing only these variations, i.e., $\mathbf{q}$ is a vector in some compact subset Q_{ad} of either $\mathbb{R}^1$, $\mathbb{R}^2$, or $\mathbb{R}^3$. For example, if we wish to only estimate the length of the damage, we assume the depth and thickness are fixed and hence $\mathbf{q} = q = l$ is in a compact subset of $\mathbb{R}^1$. However, if we wish to estimate parameters such as length and thickness while keeping the depth of the damage fixed, $\mathbf{q} = (l, h)$ and hence Q_{ad} is a subset of $\mathbb{R}^2$. If we allow all parameters to vary, $\mathbf{q} = (l, h, d) \in Q_{ad} \subset \mathbb{R}^3$. Therefore, given $\mathbf{q}$ (along with any fixed parameters) we have l, h, and d for which we can define $\tilde{\mathbf{q}} = [(0, -d), (l, -d), (l, -d - h), (0, -d - h)]$ to be the vector of corner points for the damage. This yields a formulation of the damage in terms of $\mathbf{q}$ that is equivalent to the formulation in terms of $\tilde{\mathbf{q}}$ given with

metric $\tilde{d}$. Thus, if the solution depends continuously on $\tilde{\mathbf{q}}$, the solution will also depend continuously on the parameters we estimate given by $\mathbf{q}$.

Let $V(\delta\hat{\Omega}) = \{\psi \in H^1(\delta\hat{\Omega}) | \psi(x, y_{min}) = 0 = \psi(x, y_{max})\}$ with the equivalent inner product $\langle \phi, \psi \rangle_{V(\delta\hat{\Omega})} = \int_{\delta\hat{\Omega}} \nabla\phi\nabla\overline{\psi} da$. Then given the terminology above, we first prove the sesquilinear form B depends continuously on $\tilde{\mathbf{q}}$ and use this result to obtain the continuous dependence of A on $\tilde{\mathbf{q}}$. We note that whether we include or neglect the displacement current density results in either frequency dependent or independent results, respectively. We only present the remaining theory with the displacement current density included.

Lemma 3.3.1 *There exists a positive constant K independent of the parameters $\hat{\mathbf{q}}, \tilde{\mathbf{q}}$ such that for all $\hat{\mathbf{q}}, \tilde{\mathbf{q}} \in \hat{Q}_{ad}$, the sesquilinear form $B(\tilde{\mathbf{q}})(\cdot, \cdot)$ satisfies*

$$|B(\tilde{\mathbf{q}})(\phi, \psi) - B(\hat{\mathbf{q}})(\phi, \psi)| \leq K|\phi|_{V(\delta\hat{\Omega})}|\psi|_V \tag{3.22}$$

for all $\phi, \psi \in V$ where $|\cdot|_{V(\delta\hat{\Omega})} \to 0$ when $\tilde{d}(\hat{\mathbf{q}}, \tilde{\mathbf{q}}) \to 0$.

Proof: By definition of the sesquilinear form B in (3.10)

$$\begin{aligned} |B(\tilde{\mathbf{q}})(\phi, \psi) - B(\hat{\mathbf{q}})(\phi, \psi)| = |&\langle \nabla\phi, \nabla\psi \rangle + \langle \beta_1(\tilde{\mathbf{q}})\phi, \psi \rangle + \beta_2 \int_{cs} \phi da \int_{cs} \overline{\psi} da \\ &- \langle \nabla\phi, \nabla\psi \rangle - \langle \beta_1(\hat{\mathbf{q}})\phi, \psi \rangle - \beta_2 \int_{cs} \phi da \int_{cs} \overline{\psi} da| \end{aligned}$$

or simply

$$|B(\tilde{\mathbf{q}})(\phi, \psi) - B(\hat{\mathbf{q}})(\phi, \psi)| = |\langle (\beta_1(\tilde{\mathbf{q}}) - \beta_1(\hat{\mathbf{q}}))\phi, \psi \rangle|.$$

Using the definition of β_1, the Cauchy-Schwartz inequality and (3.9), we have

$$\begin{aligned} |\langle (\beta_1(\tilde{\mathbf{q}}) - \beta_1(\hat{\mathbf{q}}))\phi, \psi \rangle| &\leq |(\beta_1(\tilde{\mathbf{q}}) - \beta_1(\hat{\mathbf{q}}))\phi||\psi| \\ &\leq |i\omega||(\mu(\tilde{\mathbf{q}})(\sigma(\tilde{\mathbf{q}}) + i\omega\epsilon(\tilde{\mathbf{q}})) - \mu(\hat{\mathbf{q}})(\sigma(\hat{\mathbf{q}}) + i\omega\epsilon(\hat{\mathbf{q}})))\phi||\psi| \\ &= \omega|\mu_{al}(\sigma_{al} + i\omega\epsilon_{al}) - i\omega\mu_0\epsilon_0||\phi|_{L^2(\delta\hat{\Omega})}|\psi| \\ &\leq k^2\omega|\mu_{al}(\sigma_{al} + i\omega\epsilon_{al}) - i\omega\mu_0\epsilon_0||\phi|_{V(\delta\hat{\Omega})}|\psi|_V \end{aligned}$$

where $\delta\hat{\Omega}$ is defined above. Therefore, if we let $K = k^2\omega|\mu_{al}(\sigma_{al} + i\omega\epsilon_{al}) - i\omega\mu_0\epsilon_0|$, we have

$$|\langle (\beta_1(\tilde{\mathbf{q}}) - \beta_1(\hat{\mathbf{q}}))\phi, \psi \rangle| \leq K|\phi|_{V(\delta\hat{\Omega})}|\psi|_V. \tag{3.23}$$

Theorem 3.3.1 *Assume the admissible parameter set $\tilde{Q}_{ad}$ is a compact subset of $\mathbb{R}^8$. Then there exists $\mathcal{F} = \mathcal{F}(\mu, \epsilon, \tilde{\Omega})$ such that for source frequencies $f_s < \mathcal{F}(\mu, \epsilon, \tilde{\Omega})$, $\tilde{\mathbf{q}} \to A(\tilde{\mathbf{q}})$ is continuous from $\tilde{Q}_{ad}$ to V.*

Proof: Let $\tilde{\mathbf{q}}^n \to \tilde{\mathbf{q}} \in \tilde{Q}_{ad}$ and let $A(\tilde{\mathbf{q}}^n), A(\tilde{\mathbf{q}})$ be the corresponding solutions of (3.11). That is,

$$B(\tilde{\mathbf{q}}^n)(A(\tilde{\mathbf{q}}^n), \psi) = \langle f, \psi \rangle \quad \text{for } \psi \in V \tag{3.24}$$

$$B(\tilde{\mathbf{q}})(A(\tilde{\mathbf{q}}), \psi) = \langle f, \psi \rangle \quad \text{for } \psi \in V. \tag{3.25}$$

Subtracting (3.25) from (3.24), we have

$$B(\tilde{\mathbf{q}}^n)(A(\tilde{\mathbf{q}}^n), \psi) - B(\tilde{\mathbf{q}})(A(\tilde{\mathbf{q}}), \psi) = 0.$$

Adding and subtracting the term $B(\tilde{\mathbf{q}}^n)(A(\tilde{\mathbf{q}}), \psi)$ and simplifying, we have

$$B(\tilde{\mathbf{q}}^n)(A(\tilde{\mathbf{q}}^n) - A(\tilde{\mathbf{q}}), \psi) = -[B(\tilde{\mathbf{q}}^n) - B(\tilde{\mathbf{q}})](A(\tilde{\mathbf{q}}), \psi).$$

Let $\psi = A(\tilde{\mathbf{q}}^n) - A(\tilde{\mathbf{q}})$. Then

$$B(\tilde{\mathbf{q}}^n)(A(\tilde{\mathbf{q}}^n) - A(\tilde{\mathbf{q}}), A(\tilde{\mathbf{q}}^n) - A(\tilde{\mathbf{q}})) = -[B(\tilde{\mathbf{q}}^n) - B(\tilde{\mathbf{q}})](A(\tilde{\mathbf{q}}), A(\tilde{\mathbf{q}}^n) - A(\tilde{\mathbf{q}})).$$

Thus, using (3.22) we have

$$\begin{aligned} |B(\tilde{\mathbf{q}}^n)(A(\tilde{\mathbf{q}}^n) - A(\tilde{\mathbf{q}}), A(\tilde{\mathbf{q}}^n) - A(\tilde{\mathbf{q}}))| &= |[B(\tilde{\mathbf{q}}^n) - B(\tilde{\mathbf{q}})](A(\tilde{\mathbf{q}}), A(\tilde{\mathbf{q}}^n) - A(\tilde{\mathbf{q}}))| \\ &\leq K|A(\tilde{\mathbf{q}})|_{V(\delta\Omega^n)}|A(\tilde{\mathbf{q}}^n) - A(\tilde{\mathbf{q}})|_V \end{aligned}$$

Then we can use the above equality and (3.13) where we note that c_2 can be established independent of $\mathbf{q}^n$ by following the proof of Lemma 3.2.2 in which $|\mu\epsilon|_\infty$ can be taken independent of q^n. Thus, defining $\tilde{K} = \frac{K}{c_2}$ independent of $\mathbf{q}^n$, we obtain

$$|A(\tilde{\mathbf{q}}^n) - A(\tilde{\mathbf{q}})|_V \leq \tilde{K}|A(\tilde{\mathbf{q}})|_{V(\delta\Omega^n)}$$

where the right side goes to 0 as $\tilde{\mathbf{q}}^n \to \tilde{\mathbf{q}}$.

3.4 Convergence Results

One possible estimation problem consists of minimizing over some set Q_{ad} of admissible parameters the least squares functional

$$J(\mathbf{q}) = \frac{1}{2}\sum_{i=1}^{n}\sum_{j=1}^{m} |A(x_i, y_j, \mathbf{q}) - \hat{A}^{ij}|^2 \tag{3.26}$$

where $\{\hat{A}^{ij}\}$ are assumed to be some sampled data available at points $(x_i, y_j), i = 1, ..., n,\ j = 1, ..., m$. In practice, the computations for the minimizing problem are carried out using an approximate system. Here we will consider Galerkin type approximations in context of the variational formulation (3.8). Let H^N be a sequence of finite dimensional subspaces of H. We denote by P^N the orthogonal projection of H onto H^N. Then the parameter estimation problem can be formulated by seeking a $\mathbf{q} \in Q_{ad}$ which minimizes

$$J^N(\mathbf{q}) = \frac{1}{2}\sum_{i=1}^{n}\sum_{j=1}^{m} |A^N(x_i, y_j, \mathbf{q}) - \hat{A}^{ij}|^2. \tag{3.27}$$

The parameter estimation problem given above assumes we have sampled data $\hat{A}^{ij}$ along a grid of points (x_i, y_j), $i = 1, ..., n$, $j = 1, ..., m$ although it is not physically possible to obtain such data. Typically potentials, for example A, are only used for computational purposes. They allow one to overcome some of the difficulties which arise computationally when using field variables; the biggest complication being the number of equations which must be solved when using field variables [32]. The field $\mathbf{B}$ or $\mathbf{H}$, however, is the only measurable quantity.

Therefore we also explore an alternative problem which we use in much of our computational and experimental investigations. It involves cost functionals using observations of the magnetic flux density $\mathbf{B} = \nabla \times \mathbf{A} = (\frac{\partial A}{\partial y}, -\frac{\partial A}{\partial x}, 0) = (B_1, B_2, 0)$. In this case, as discussed in Chapter 5, (3.26) and (3.27) are replaced by

$$J(\mathbf{q}) = \frac{1}{2}\sum_{i=1}^{n}\sum_{j=1}^{m} |B_k(x_i, y_j, \mathbf{q}) - \hat{B}_k^{ij}|^2 \tag{3.28}$$

and

$$J^N(\mathbf{q}) = \frac{1}{2}\sum_{i=1}^{n}\sum_{j=1}^{m} |B_k^N(x_i, y_j, \mathbf{q}) - \hat{B}_k^{ij}|^2 \tag{3.29}$$

respectively, for $k = 1$ or 2 (see (5.2), (5.3)).

Using the theory developed in this chapter along with the notation $\tilde{\mathbf{q}}$ as described in the previous section, we obtain the following result.

Theorem 3.4.1 *Suppose*

(B1) The finite dimensional subspaces H^N satisfy $H^N \subset V$.

(B2) For each $\psi \in V, |P^N\psi - \psi|_V \to 0$ as $N \to \infty$.

Let $\tilde{\mathbf{q}}^N$ be arbitrary in $\tilde{Q}_{ad}$ such that $\tilde{\mathbf{q}}^N \to \tilde{\mathbf{q}}$ in $\tilde{Q}_{ad}$. Then as $N \to \infty$, there exists $\mathcal{F} = \mathcal{F}(\mu, \epsilon, \tilde{\Omega})$ such that for source frequencies $f_s < \mathcal{F}(\mu, \epsilon, \tilde{\Omega})$, we have $A^N(\tilde{\mathbf{q}}^N) \to A(\tilde{\mathbf{q}}) \in V$ where $A(\tilde{\mathbf{q}})$ is the solution to (3.11).

Proof: We have

$$B(\tilde{\mathbf{q}}^N)(A^N(\tilde{\mathbf{q}}^N), \psi^N) = \langle f, \psi^N \rangle \quad \text{for } \psi^N \in H^N \tag{3.30}$$

$$B(\tilde{\mathbf{q}})(A(\tilde{\mathbf{q}}), \psi) = \langle f, \psi \rangle \qquad \text{for } \psi \in V. \tag{3.31}$$

Then it follows that

$$|A^N(\tilde{\mathbf{q}}^N) - A(\tilde{\mathbf{q}})|_V \le |A^N(\tilde{\mathbf{q}}^N) - P^N A(\tilde{\mathbf{q}})|_V + |P^N A(\tilde{\mathbf{q}}) - A(\tilde{\mathbf{q}})|_V.$$

Hence from (B2) it suffices to prove

$$|A^N(\tilde{\mathbf{q}}^N) - P^N A(\tilde{\mathbf{q}})|_V \to 0 \quad \text{for } \tilde{\mathbf{q}}^N \to \tilde{\mathbf{q}} \in \tilde{Q}_{ad} \quad \text{as } N \to \infty.$$

Taking $\psi = \psi^N$ in (3.31) and subtracting from (3.30), we obtain

$$B(\tilde{\mathbf{q}}^N)(A^N(\tilde{\mathbf{q}}^N), \psi^N) - B(\tilde{\mathbf{q}})(A(\tilde{\mathbf{q}}), \psi^N) = 0$$

for $\psi^N \in H^N$. Furthermore, by adding and subtracting $B(\tilde{\mathbf{q}}^N)(P^N A(\tilde{\mathbf{q}}), \psi^N)$ and $B(\tilde{\mathbf{q}}^N)(A(\tilde{\mathbf{q}}), \psi^N)$ and simplifying, we have

$$B(\tilde{\mathbf{q}}^N)(A^N(\tilde{\mathbf{q}}^N) - P^N A(\tilde{\mathbf{q}}), \psi^N) + B(\tilde{\mathbf{q}}^N)(P^N A(\tilde{\mathbf{q}}) - A(\tilde{\mathbf{q}}), \psi^N) \\ + [B(\tilde{\mathbf{q}}^N) - B(\tilde{\mathbf{q}})](A(\tilde{\mathbf{q}}), \psi^N) = 0.$$

Choosing $\psi^N = \Delta^N = A^N(\tilde{\mathbf{q}}^N) - P^N A(\tilde{\mathbf{q}})$, we find that

$$B(\tilde{\mathbf{q}}^N)(\Delta^N, \Delta^N) + B(\tilde{\mathbf{q}}^N)(P^N A(\tilde{\mathbf{q}}) - A(\tilde{\mathbf{q}}), \Delta^N) + [B(\tilde{\mathbf{q}}^N) - B(\tilde{\mathbf{q}})](A(\tilde{\mathbf{q}}), \Delta^N) = 0.$$

Therefore,

$$|B(\tilde{\mathbf{q}}^N)(\Delta^N, \Delta^N)| = | - B(\tilde{\mathbf{q}}^N)(P^N A(\tilde{\mathbf{q}}) - A(\tilde{\mathbf{q}}), \Delta^N) - [B(\tilde{\mathbf{q}}^N) - B(\tilde{\mathbf{q}})](A(\tilde{\mathbf{q}}), \Delta^N)|.$$

However, using the triangle inequality, (3.12), (3.22), and the Cauchy-Schwartz inequality, we can bound the right side of the above by

$$| - B(\tilde{\mathbf{q}}^N)(P^N A(\tilde{\mathbf{q}}) - A(\tilde{\mathbf{q}}), \Delta^N) - [B(\tilde{\mathbf{q}}^N) - B(\tilde{\mathbf{q}})](A(\tilde{\mathbf{q}}), \Delta^N)| \leq \\ (c_1 |P^N A(\tilde{\mathbf{q}}) - A(\tilde{\mathbf{q}})|_V + K|A(\tilde{\mathbf{q}})|_{V(\delta\Omega^N)})|\Delta^N|_V$$

where c_1 is the constant in Lemma 3.2.1 and K is the constant in Lemma 3.3.1. We can conclude using (3.13) that

$$|\Delta^N|_V \leq \frac{c_1}{c_2}|P^N A(\tilde{\mathbf{q}}) - A(\tilde{\mathbf{q}})|_V + \frac{K}{c_2}|A(\tilde{\mathbf{q}})|_{V(\delta\Omega^N)}|A(\tilde{\mathbf{q}})|_V.$$

Thus, given any $\tilde{\mathbf{q}}^N \to \tilde{\mathbf{q}} \in \tilde{Q}_{ad}$, it follows from (B2) that $\Delta^N = A^N(\tilde{\mathbf{q}}^N) - P^N A(\tilde{\mathbf{q}}) \to 0$ as $N \to \infty$, giving us the desired results.

We note that the results above do not, strictly speaking, guarantee convergence in our minimization problem since $A^N(\tilde{\mathbf{q}}^N) \to A(\tilde{\mathbf{q}})$ in V only guarantees convergence of $\mathbf{B}^N(\mathbf{q}) \to \mathbf{B}(\mathbf{q})$ in L^2, not pointwise convergence in (x, y) of either A or $\mathbf{B}$. To obtain such a rigorous theory one must use averaged A or $\mathbf{B}$ data about the points (x_i, y_j), i.e., assume the observations $\hat{B}_k^{ij}$ are for the average

$$\frac{1}{\tilde{\Omega}_{ij}} \int_{\tilde{\Omega}_{ij}} B_k(x, y; \mathbf{q}) da \tag{3.32}$$

over small domain $\tilde{\Omega}_{ij}$ centered about the points (x_i, y_j). As the surface area of $\tilde{\Omega}_{ij}$ tends to zero, (3.32) tends to $B_k(x_i, y_j; \mathbf{q})$. We note that, in actuality, (3.32) may more accurately describe the experimental data obtained from a sensor. The sensor detects magnetic flux density across the entire surface area of the sensor and then outputs this data as data for a specific point. This must involve averaging of the data over the area in some fashion.

One might try an alternative approach and attempt to use additional assumptions on the problem and data to guarantee convergence of $A^N(\mathbf{q}^N) \to A(\mathbf{q})$ in a stronger norm (say the $H^3(\tilde{\Omega})$ norm) so that convergence is guaranteed in the pointwise sense for $\tilde{\Omega} \subset \mathbb{R}^2$ ([6, Chapter 6]). We then would have $A^N(\mathbf{q}^N) \to A(\mathbf{q})$ in $H^3(\tilde{\Omega})$ which would imply $\mathbf{B}^N(\mathbf{q}^N) = \nabla \times A^N(\mathbf{q}^N) \to \mathbf{B}(\mathbf{q}) = \nabla \times A(\mathbf{q})$ in $H^2(\tilde{\Omega})$. For $\tilde{\Omega} \subset \mathbb{R}^2$, we have $H^3(\tilde{\Omega}) \hookrightarrow C(\overline{\tilde{\Omega}})$ and $H^2(\tilde{\Omega}) \hookrightarrow C(\overline{\tilde{\Omega}})$ which readily gives pointwise convergence for both A and $\mathbf{B}$. However, since these are elliptic problems with discontinuous coefficients, the regularity and convergence (in $H^3(\tilde{\Omega})$) is not possible without some type of additional smoothing of problem data, e.g., modifying coefficients and solutions, which introduces another level of approximation. We choose however not to follow this latter approach. Instead, we interpret all of our data and entries in our cost functionals as averaged quantities over small domains $\tilde{\Omega}_{ij}$ as discussed above. With this interpretation, our convergence results gives a complete theory for the inverse problem considered.

Chapter 4

Computational Method

Our ultimate goal is determine the feasibility of using a portable sensing device in conjunction with inverse problem techniques to characterize the geometry of a hidden, i.e., subsurface, damage within a sample. To achieve this goal, we must develop fast and efficient forward computational methods to be used possibly numerous times in the inverse problem formulated in the next two chapters. To this end, we examine reduced order Karhunen-Loeve or Proper Orthogonal Decomposition (POD) techniques.

The POD technique is an attractive order reduction method, because basis elements are formed in an "optimal" way which span a data set consisting of either numerical simulations or experimental data. Since the POD basis is formed so that *each* basis element captures important aspects of the data set, only a small number of POD basis elements are needed in general to describe the solution [38]. Consequently, if the POD method is successful, implementation should result in a decrease of computational time.

In this chapter, we begin by presenting a general discussion of the POD method, including the formation of the POD basis, the choice of a reduced basis and the approximation of a solution using the (reduced) POD basis. In reference to the latter, the approximation using POD basis elements, we discuss two possible techniques one may use in forming the approximation, a POD/Galerkin method and

POD/Interpolation method, giving advantages and disadvantages of each method. We conclude the chapter with an overview of the optimization algorithm utilized in the parameter estimation problem in Chapters 5 and 6.

4.1 The POD Method

We summarize the use of the POD method in the context of the least squares inverse problem described in detail in Chapters 5 and 6. For further details on the general POD method, we refer the reader to [3, 7, 8, 14, 25, 28, 29, 34, 35, 36, 37, 38] and the extensive list of references contained therein.

The first step in forming the POD basis is to collect "snapshots" or solutions across time, space or a varied parameter. In our case, we let $\mathbf{q}$ be the vector parameter characterizing physical properties of the damage; i.e., as discussed in Section 3.3, $\mathbf{q}$ the geometry of the damage including the length, thickness, depth, etc. of the damage. For an ensemble of damages $\{\mathbf{q}_j\}_{j=1}^{N_s}$, we obtain corresponding solutions, $\{\mathbf{A}(\mathbf{q}_j)\}_{j=1}^{N_s}$, of (2.23) with (2.24), for magnetic vector potentials which we call our "snapshots". Alternatively, from the solution set $\{\mathbf{A}(\mathbf{q}_j)\}_{j=1}^{N_s}$, we can obtain the magnetic fluxes $\{\mathbf{B}(\mathbf{q}_j)\}_{j=1}^{N_s}$ and instead use these as our "snapshots" if we wish to treat magnetic fluxes as our basic state variable. (In [4] we compare results using one field versus the other as the basic state variable. The conclusions are summarized in Chapter 5.) For our explanation, we will consider snapshots on $\mathbf{A} = (0, 0, A_3)$ and hence our explanation will be for the scalar case. For the vector case, we would simply proceed componentwise [3, 14, 38]. Without loss of generality, we will denote the vector $\mathbf{A}$ by its scalar nonzero component A, i.e., the A_3 component of $\mathbf{A}$.

As explained in [38], we seek basis elements of the form

$$\Phi_i = \sum_{j=1}^{N_s} V_i(j) A(\mathbf{q}_j) \tag{4.1}$$

where the coefficients $V_i(j)$ are chosen such that each POD basis element Φ_i, $i =$

$1, 2, ..., N_s$, maximizes

$$\frac{1}{N_s}\sum_{j=1}^{N_s}|\langle A(\mathbf{q}_j), \Phi_i\rangle_{L^2(\Omega,\mathbb{C})}|^2$$

subject to $\langle \Phi_i, \Phi_i\rangle_{L^2(\Omega,\mathbb{C})} = ||\Phi_i||^2 = 1$. It is thus readily seen using standard arguments that the coefficients $V_i(j)$ are found by solving the eigenvalue problem

$$CV = \lambda V$$

where the covariant matrix C is given by

$$[C]_{ij} = \frac{1}{N_s}\langle A(\mathbf{q}_i), A(\mathbf{q}_j)\rangle_{L^2(\Omega,\mathbb{C})}.$$

Since the matrix C is a Hermitian positive semi-definite matrix, it possesses a complete set of orthogonal eigenvectors with corresponding nonnegative real eigenvalues. We order the eigenvalues along with their corresponding eigenvectors such that the eigenvalues are in decreasing order,

$$\lambda_1 \geq \lambda_2 \geq ... \geq \lambda_{N_s} \geq 0.$$

We then normalize the eigenvectors corresponding to the rule

$$V_i \cdot V_j = \frac{\delta_{ij}}{N_s\lambda_j}.$$

Then the i^{th} POD basis element is defined by (4.1) where $V_i(j)$ represents the j^{th} component of the i^{th} eigenvector of C. It can also be shown that $\{\Phi_i\}_{i=1}^{N_s}$ are orthonormal in $L^2(\Omega, \mathbb{C})$ and $span\{\Phi_i\}_{i=1}^{N_s} = span\{A(\mathbf{q}_j)\}_{j=1}^{N_s}$. Indeed, given any $A(\mathbf{q}_j)$, we have

$$A(\mathbf{q}_j) = \sum_{k=1}^{N_s}\alpha_k(\mathbf{q}_j)\Phi_k$$

where

$$\alpha_k(\mathbf{q}_j) = \langle A(\mathbf{q}_j), \Phi_k\rangle_{L^2(\Omega,\mathbb{C})}.$$

We remark that if any of the λ_i's are zero, say $\lambda_i = 0$ for $i = K+1, ..., N_s$, then even though the corresponding V_i are orthogonal (and of course linearly independent),

we will have $span\{\Phi_i\}_{i=1}^{K} = span\{\Phi_i\}_{i=1}^{N_s}$. Hence in this case we will only generate $K < N_s$ linearly independent POD basis elements. We refer the reader to a discussion of the relation between POD basis element formation and the popular singular value decomposition (SVD) methods in linear algebraic methods given in [34], for example.

To determine the reduced number N of POD basis elements required to accurately portray the ensemble of "snapshots" $\{A(\mathbf{q}_j)\}_{j=1}^{N_s}$, we examine

$$\sum_{j=1}^{N} \lambda_j / \sum_{j=1}^{N_s} \lambda_j \tag{4.2}$$

which represents the percentage of "energy" in $span\{A(\mathbf{q}_j)\}_{j=1}^{N_s}$ that is captured in $span\{\Phi_j\}_{j=1}^{N}$. The reduced basis consists of only the first N elements Φ_i, $i = 1, ..., N$, where N is chosen according to the percentage "energy" desired. We intuitively argue that the "energy" we are referring to is related to the total electrostatic energy. Simply stated, the matrix C contains terms of the form

$$\int_\Omega A\overline{A}da = \int_\Omega |A|^2 da.$$

which can be written in terms of the electric field E according to (2.15), $E = -i\omega A - \nabla\phi$. Therefore,

$$\int_\Omega |A|^2 da = C_1 \int_\Omega |E + \nabla\phi|^2 da.$$

where $C_1 = \frac{1}{\omega^2}$. Since $\nabla\phi$ is constant (which we proved in Chapter 3), the terms in the matrix C are a perturbation of terms associated with electrostatic energy given by

$$W_E = \frac{1}{2}\epsilon_0 \int_V |E|^2 dV.$$

Thus we conclude that when we snapshot on the magnetic vector potential, the ratio in (4.2) is a good indication of the electrostatic energy stored across Ω ([16]).

Using only the first N POD basis elements, we obtain the approximation $A^N(\mathbf{q}_j)$ for $A(\mathbf{q}_j)$ such that

$$A(\mathbf{q}_j) \approx A^N(\mathbf{q}_j) \equiv \sum_{k=1}^{N} \alpha_k(\mathbf{q}_j)\Phi_k.$$

To approximate $A^N(\mathbf{q})$ where $\mathbf{q}$ is a given parameter *not* in the set $\{\mathbf{q}_j\}_{j=1}^{N_s}$, we extend the approximation formula to obtain

$$A^N(\mathbf{q}) = \sum_{k=1}^{N} \alpha_k(\mathbf{q})\Phi_k \tag{4.3}$$

where two possible ways of computing $\alpha_k(\mathbf{q})$ are by using a POD/Galerkin method or a POD/Interpolation method (which we discuss in detail below).

Once we have the solution $A^N(\mathbf{q})$, we can recapture the explicit time dependence by referring to the formula (2.2) in Section 2.1 given by

$$\tilde{\tilde{A}}(x, y, t; \mathbf{q}) \approx \tilde{\tilde{A}}^N(x, y, t; \mathbf{q}) = Re(A^N(x, y; \mathbf{q})e^{i\omega t})$$

where

$$A^N(x, y; \mathbf{q}) = \sum_{k=1}^{N} \alpha_k(\mathbf{q})\Phi_k(x, y).$$

4.2 Determination of POD coefficients

There are different ways to determine the coefficients $\alpha_k(\mathbf{q})$ in (4.3) for $\mathbf{q}$ not in the set $\{\mathbf{q}_j\}_{j=1}^{N_s}$ upon which we snapshot. The traditional way is to use a POD/Galerkin method; however, there are many advantages in choosing a POD/Interpolation method instead. In this section, we will examine both methods and compare the advantages and disadvantages of each.

4.2.1 POD/Galerkin Method

The approach described in this section is essentially an application of Galerkin's method to the integro-differential equation (3.6) (from Section 3.1) in conjunction with the reduced order POD method. The POD/Galerkin method uses the approximation given in (4.3) in the variational form of the integro-differential equation where the test functions are chosen to be the reduced order POD basis elements $\{\Phi_i\}_{i=1}^{N}$.

The system then reduces into a linear system which we can solve for the coefficients $\alpha_k(\mathbf{q})$, $k = 1, ..., N$.

In our computational efforts we follow the literature ([30, 31, 32, 33, 50]) and neglect the displacement current in the numerical implementation. Therefore, we will use the variational form from Section 3.2.2:

$$\frac{1}{\mu_0}\left(\langle\frac{\partial A}{\partial x},\frac{\partial \psi}{\partial x}\rangle+\langle\frac{\partial A}{\partial y},\frac{\partial \psi}{\partial y}\rangle\right)+\langle i\omega\sigma A,\psi\rangle-\frac{i\omega\sigma_{cu}}{\Delta_{cs}}\int_{cs}Ada\int_{cs}\overline{\psi}da=\frac{I_{cs}}{\Delta_{cs}}\int_{cs}\overline{\psi}da. \tag{4.4}$$

Substituting (4.3) into (4.4) and letting $\psi = \Phi_l$, $l = 1, ..., N$, we obtain the system

$$\left(K+i\omega M-\frac{i\omega\sigma_{cu}}{\Delta_{cs}}b\overline{b}^T\right)\alpha=\frac{I_{cs}}{\Delta_{cs}}b \tag{4.5}$$

for $\alpha = [\alpha_1, \alpha_2, ..., \alpha_N]^T$ where

$$[K]_{lk}=\frac{1}{\mu_0}\left(\int_\Omega\frac{\partial\Phi_k}{\partial x}\overline{\frac{\partial\Phi_l}{\partial x}}da+\frac{\partial\Phi_k}{\partial y}\overline{\frac{\partial\Phi_l}{\partial y}}da\right),$$

$$[M]_{lk}=\int_\Omega\sigma\Phi_k\overline{\Phi_l}da,$$

and

$$[b]_l=\int_{cs}\overline{\Phi_l}da.$$

Recall the parameter vector $\mathbf{q}$ only changes the conductivity σ and therefore only effects the matrix M. Consequently, in the inverse problem, for each "new guess" of $\mathbf{q}$, only the matrix M must be calculated each time; this reduces the time required for each forward estimation and hence the total time for the entire inverse problem.

Next we consider the accuracy of the POD approximation

$$\mathbf{B}^N(\mathbf{q})=\nabla\times A^N(\mathbf{q}) \tag{4.6}$$

by comparing the approximation to the finite element simulation using Ansoft Maxwell 2D Field Simulator for a sample containing a damage of length $l = 1.3mm$ or equivalently $\mathbf{q} = l = 1.3mm$ with a fixed thickness of $2mm$ and depth of $9mm$. In the examples below, snapshots were taken of the magnetic vector potential for damages

having lengths $l = 0mm$ to $l = 4mm$ in increments of $0.2mm$. Therefore, $l = 1.3mm$ is a length *not* included in the snapshots. The approximate energy captured in the POD approximation for various values of N according to (4.2) is given in Table 4.1.

Table 4.1: Energy Captured using Snapshots of A while Varying Length

N	Energy Captured
1	99.999469355655%
2	99.999998707290%
3	99.999999918539%
4	99.999999978293%
5	99.999999987493%
6	99.999999990451%
7	99.999999992129%
8	99.999999993439%
9	99.999999994409%
10	99.999999995308%

However, as discussed previously, this energy is related to the electrostatic energy and hence not the energy stored in the magnetic field given by

$$W_m = \frac{1}{2}\mu_0^{-1}\int_V |\mathbf{B}|^2 = \frac{1}{2}\mu_0^{-1}\int_V \mathbf{B}\cdot\overline{\mathbf{B}}dV$$

as stated in [16]. Since we are comparing the reduced approximation for the magnetic flux density for various values of N, we can argue that N should be chosen based on the total magnetic energy captured (or similar energy) as opposed to electrostatic energy. In other words, we should consider the energy captured if we were to snapshot on B_2 (for example) instead of A. Table 4.2 gives the energy captured when taking snapshots of the B_2 field. We note that although the choice of N should intuitively be based on snapshots of B_2, the approximation for B_2 behaves in the same manner whether we snapshot on A first and then form B_2 according to (4.6) or if we snapshot on B_2 directly.

Table 4.2: Energy Captured using Snapshots of B_2 while Varying Length

N	Energy Captured
1	95.752844126957%
2	98.938760682215%
3	99.515414870549%
4	99.680555604825%
5	99.749219883487%
6	99.789119249012%
7	99.822617546932%
8	99.853187498393%
9	99.871258779223%
10	99.888757131260%

Figures 4.1, 4.2 and 4.3 give plots comparing the reduced order POD approximation for various values of N related to the finite element simulation for length $l = 1.3mm$. We first note that $N = 1$ POD basis element does not approximate the finite element solution well at all; however, when we use $N = 3$ POD basis elements, there is a considerable improvement in the approximation. Using only $N = 3$ POD basis elements, we were able to fairly accurately approximate the finite element solution which uses over 7000 finite elements in its approximation. However, as the value of N increases, the approximation continually worsens as the conditioning of the linear system we are solving deteriorates.

Table 4.3 gives the condition number of the matrix

$$K + i\omega M - \frac{i\omega\sigma_{cu}}{\Delta_{cs}} b\overline{b}^T,$$

used in (4.5) to solve for α for $N = 1 - 4, 8$ and 21, plotted in Figures 4.1, 4.2 and 4.3. A full table of condition numbers for all values of N can be found in Appendix A.1. When $N = 3$ basis elements are used, the condition number is approximately 80; however, the condition number jumps to approximately 360 when using $N = 4$ elements. Following the same pattern, the condition number is over 12,000 when all of the POD basis elements ($N = 21$) are used in the approximation. This behavior is not apparent when strictly looking at the percentage of energy captured (Table 4.2).

According to the percentage of energy capture, the approximation should continuously improve.

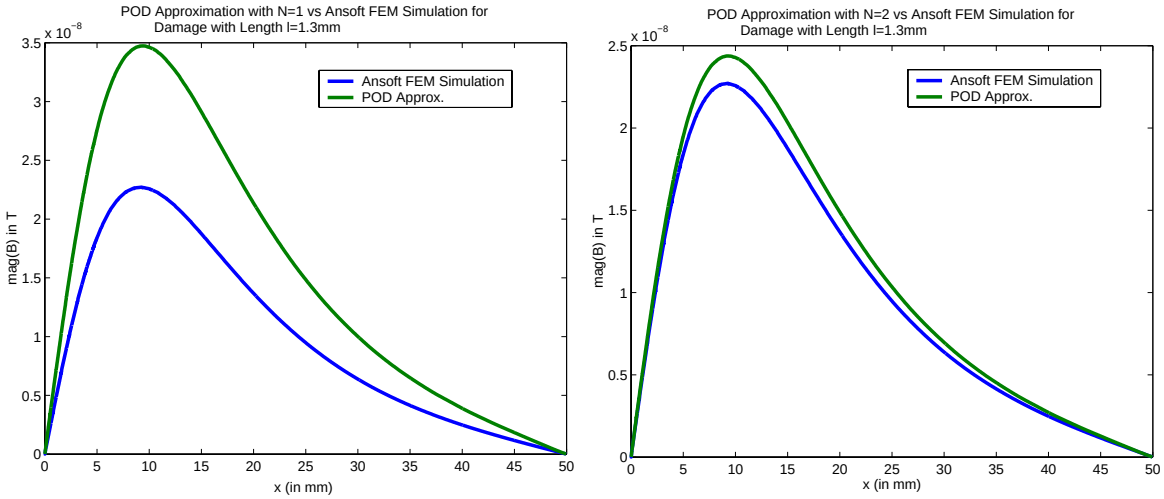

Figure 4.1: Finite Element Simulations vs. POD Approximations formed using the POD/Galerkin Method with $N = 1$ and $N = 2$ Basis Elements

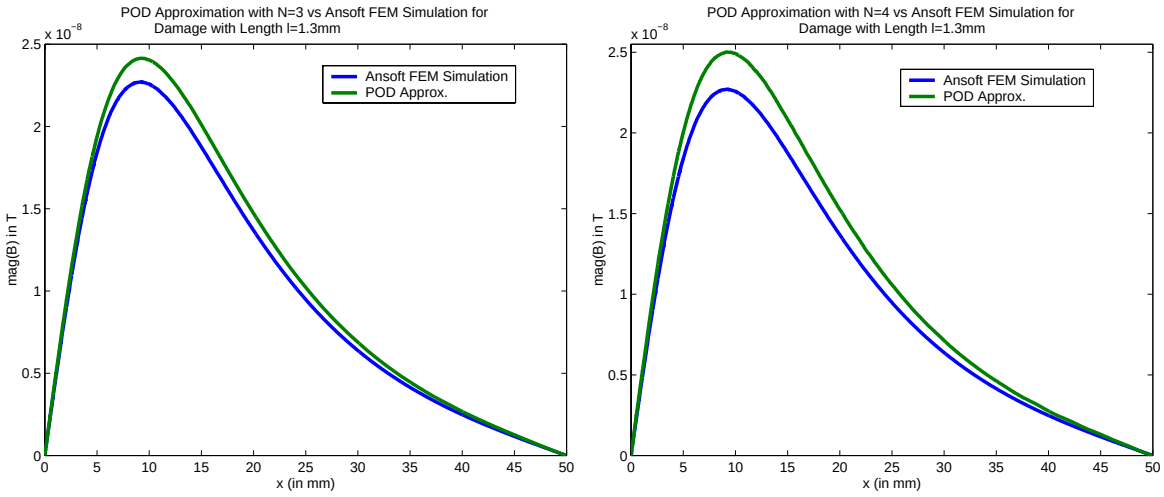

Figure 4.2: Finite Element Simulations vs. POD Approximations formed using the POD/Galerkin Method with $N = 3$ and $N = 4$ Basis Elements

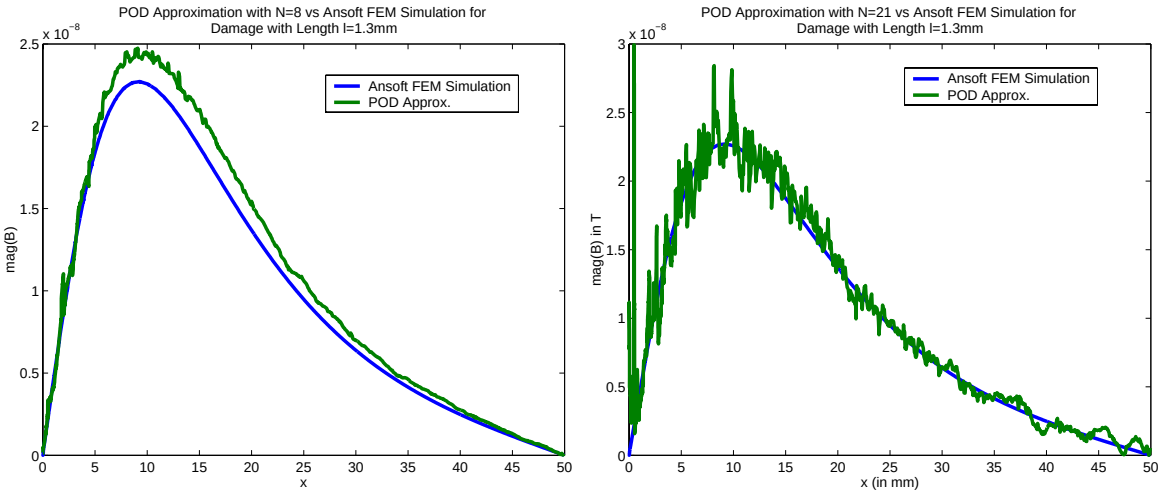

Figure 4.3: Finite Element Simulations vs. POD Approximations formed using the POD/Galerkin Method with $N = 8$ and $N = 21$ Basis Elements

However, the figures seem to illustrate that the accuracy of the approximation does not improve when N is greater than 3. This is indeed true. Table 4.4 gives the average relative error of approximating the finite element solution with a reduced POD approximation across the same line depicted in the figures for $N = 1$ to $N = 10$ (a full table can be found in Appendix A.2.1). The best approximation is found when $N = 3$ and continually worsens for larger values of N; therefore, the optimal value of N to use in the optimization problem appears to be $N = 3$.

Table 4.3: Condition Number of the Linear System (4.5) Used in Solving for α

N	Condition Number
1	1.0000
2	3.8635
3	80.7903
4	359.2911
8	2818.0875
21	12,431.3195

Table 4.4: Average Relative Error in the POD Approximation of $|B_2|$ across a Line Located $1mm$ above the Conducting Sheet using the POD/Galerkin Method

N	Average Relative Error
1	52.05%
2	7.16%
3	6.31%
4	10.97%
5	11.94%
6	15.70%
7	14.42%
8	15.15%
9	18.30%
10	26.92%

4.2.2 POD/Interpolation Method

The POD/Interpolation method relies entirely on the values of the coefficients $\alpha_k(\mathbf{q})$ for $\mathbf{q}$ in the set $\{\mathbf{q}_j\}_{j=1}^{N_s}$. Unlike the POD/Galerkin method, it does not take into account the boundary value problem which A satisfies.

Various interpolation methods may be chosen to evaluate $\alpha_k(\mathbf{q})$ such as linear interpolation, cubic spline interpolation or nearest neighbor interpolation. However, in the simulations presented, the built-in Matlab interpolation functions *interp1* or *interp2*, one-dimensional interpolation and two-dimensional interpolation respectively, were used in which the linear interpolation method was chosen for the one-parameter case and cubic spline interpolation was chosen for the two-parameter case. We chose these methods, because initial trials suggested this would be the best method to choose in order to achieve the most accurate results in the inverse problem.

For the one-parameter case, i.e., for $\mathbf{q} = q$ (the scalar case), the coefficients $\alpha_k(\mathbf{q})$ are defined through linear interpolation by

$$\alpha_k(q) \equiv \alpha_k(q_j) + (\alpha_k(q_{j+1}) - \alpha_k(q_j))\frac{q - q_j}{q_{j+1} - q_j} \tag{4.7}$$

where there exists j in $\{1, ..., N_s - 1\}$ such that $q_j < q < q_{j+1}$.

For the two-parameter case, more information was needed to achieve the most accurate results. Hence, we chose cubic spline interpolation which uses information from several of the known POD coefficients, instead of only the adjacent parameter values. For a more detailed discussion on spline interpolation, we will refer the reader to [44, pp. 348-353] and [45, pp. 93-106].

We return to the one-dimensional interpolation problem and carry out the same comparison as described in Section 4.2.1. We snapshot on length and compare the POD approximation using the POD/Interpolation method to the finite element approximation for a length of $l = 1.3mm$ as depicted in Figures 4.4 and 4.5. In this case, the POD/Interpolation method does a considerably better job at approximating the finite element simulation with only 2-3 basis elements. With $N = 2$ basis elements, there is still some visible error in the approximation, but using $N = 3$ POD basis elements with POD/Interpolation, the approximation appears to lie directly over the finite element simulation.

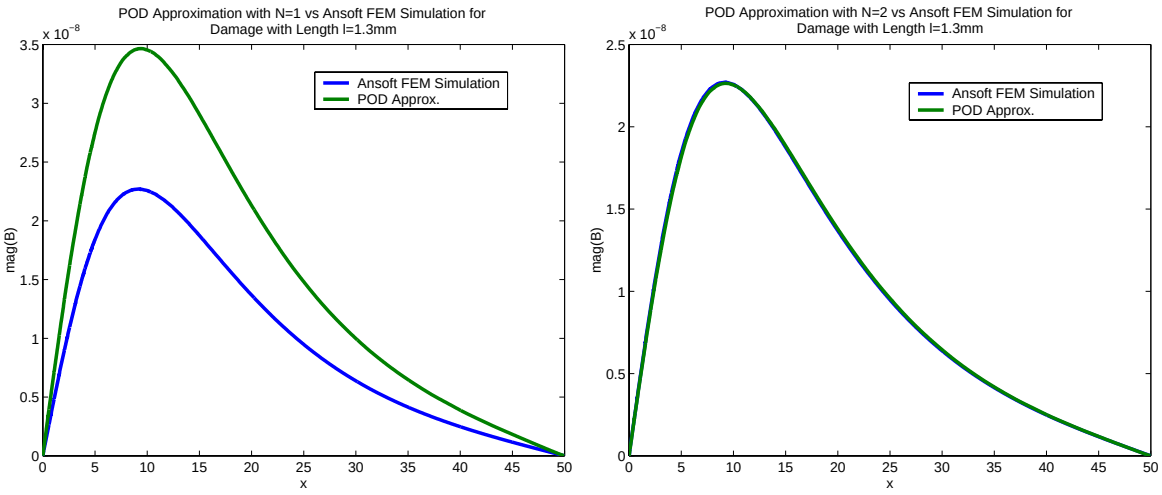

Figure 4.4: Finite Element Simulations vs. POD Approximations formed using the POD/Interpolation Method with $N = 1$ and $N = 2$ Basis Elements

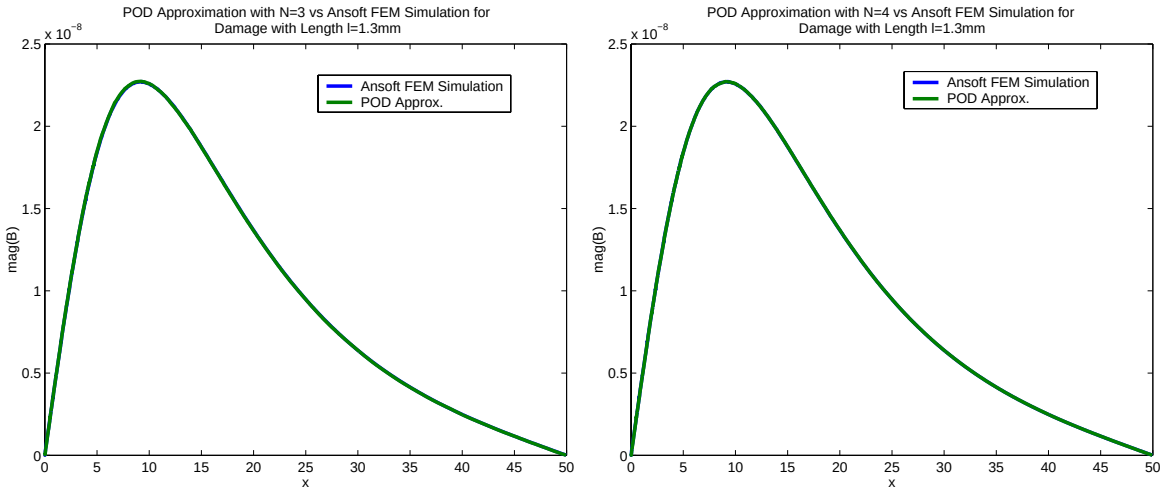

Figure 4.5: Finite Element Simulations vs. POD Approximations formed using the POD/Interpolation Method with $N = 3$ and $N = 4$ Basis Elements

Table 4.5 gives the average numerical error in the POD approximation for $N = 1$ to $N = 7$ (a full table can be found in Appendix A.2.2). The error reaches its minimum at $N = 5$, but either $N = 4$ or $N = 5$ looks like the best choice for N in the optimization problem for detecting length alone. In comparison, the POD approximation using POD/Interpolation with $N = 2$ yields less than a 2% relative error, a much better approximation than when using the POD/Galerkin method for any value of N (the *best* POD/Galerkin approximation results in a 6.31% relative error). However, in both cases, although the percentage of energy captured continuously increases, the approximation does not continually improve as N increases (Tables 4.4 and 4.5) when using either the POD/Galerkin method or the POD/Interpolation method.

Table 4.5: Average Relative Error in the POD Approximation of $|B_2|$ across a Line Located $1mm$ above the Conducting Sheet using the POD/Interpolation Method

N	Average Relative Error
1	51.69%
2	1.95%
3	1.14%
4	0.63%
5	0.55%
6	0.79%
7	0.79%

4.2.3 Summary of POD/Galerkin vs. POD/Interpolation Methods

We conclude this section with some final comparisons between the POD/Galerkin method and POD/Interpolation method used in conjunction with a reduced order POD approximation. First of all, for damages which are represented in the set of snapshots, i.e., for $\mathbf{q}$ in the set $\{\mathbf{q}_j\}_{j=1}^{N_s}$, the two methods are theoretically equivalent although random numerical error may impact the numerical approximations. Indeed if $\mathbf{q}$ is in the set $\{\mathbf{q}_j\}_{j=1}^{N_s}$, then $A(\mathbf{q})$ is a solution of the integro-differential equation and hence a solution to (4.4) (as A is a snapshot or solution for the particular damage represented by $\mathbf{q}$). Therefore, there exist a solution $\hat{\alpha} = [\hat{\alpha}_1, ..., \hat{\alpha}_{N_s}]$ to (4.5) such that

$$A(\mathbf{q}) = \sum_{k=1}^{N} \hat{\alpha}_k(\mathbf{q})\Phi_k.$$

Consequently, $\langle \Phi_k, \Phi_l \rangle = \delta_{kl}$ implies

$$\hat{\alpha}_l = \langle A(\mathbf{q}), \Phi_l \rangle = \alpha_l$$

by definition of α_l.

However, when $\mathbf{q}$ is not in the set $\{\mathbf{q}_j\}_{j=1}^{N_s}$, the two methods are not equivalent. Furthermore, from the examples described above, there are cases in which the POD/Interpolation method clearly produces more accurate results. We cannot make this generalization in all cases; nonetheless, one distinct advantage of the POD/Interpolation method is that *it does not rely on the equations describing the system.* This can be very useful in some experimental applications in which data is available but it is not easy to model the physical process corresponding to the data. In this case, if there is correlation in the data, the POD method may be a viable approximation method in which an appropriate option for determining the coefficients would be a POD/Interpolation method.

4.3 Optimization Algorithm

Using the reduced order computational methodology presented in the previous section for calculating the magnetic vector potential A given specific crack parameters, we shall try to identify parameters such as the length, thickness, and depth of a damage within a sample. In Chapters 5 and 6, we will discuss the specific inverse problem, defining the least squares criterion used in this optimization process depending on the application. When we use the POD/Linear Interpolation method in the POD approximation, the gradient of the least squares criterion is piecewise constant. Since gradient-based algorithms require a continuous gradient, we chose a direct search algorithm instead, the Nelder-Mead simplex algorithm. We will provide a brief discussion on the Nelder-Mead algorithm here. For a more detailed discussion, we refer the reader to [26, 43].

As mentioned, the Nelder-Mead algorithm is a direct search algorithm which does not explicitly use gradient information. Instead, given $M+1$ vertices, $\{x_i\}_{i=1}^{M+1}$, the algorithm sorts the vertices and labels the vertices in order of "best" to "worst" where the function evaluation at the vertex determines the rank of the vertex. If the function to be minimized is labeled f, the vertices are ranked according to

$$f(x_1) \leq f(x_2) \leq ... \leq f(x_{M+1})$$

with x_1 being the "best" vertex and x_{M+1} the "worst". The rest of the algorithm can best be described by examining the Nelder-Mead simplex in Figure 4.6 where x_3 is considered to be the "worst" choice and x_1 and x_2 are the other points of comparison.

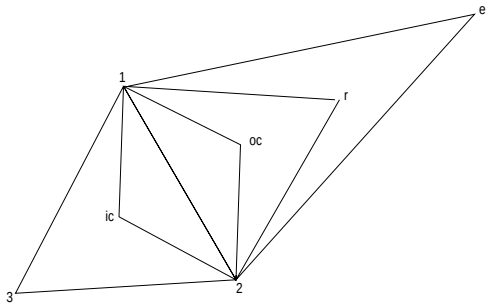

Figure 4.6: Nelder-Mead Algorithm

Once the vertices are sorted, the algorithm then tries to replace the worse point with a new point. The first point tried is the reflection (r) of the old point. If the reflected point is not better, the point is expanded (e). This point is then checked against the old point. When the new point is an improvement, the vertices are sorted again and the algorithm repeats. If the expanded point in no better, the algorithm next tries an outside contraction (oc) and then an inside contraction (ic). If none of the new points work, the entire simplex is altered by keeping only the best point x_1 and reducing the other points according to $x_i = x_1 - (x_i - x_1)/2$, $i = 2, ..., M + 1$. The process then starts over. This process repeats until the difference between the function evaluation at the best and worst points is below a desired tolerance. In the next two chapters, this algorithm is applied to a least squares criterion which will be explicitly defined.

Chapter 5

Simulated Results

In this chapter we present computational results for the least squares inverse problem based on the methodology developed in Chapter 4. We are concerned with identifying the geometry of a crack, i.e., estimating parameters such as the length, thickness, and depth of a crack within a sample. (Recall Figure 3.3.) To determine the feasibility of this task and to illustrate the use of the reduced order methodology, we first estimate a single parameter keeping the other two parameters fixed. We estimate length, thickness and depth separately, and then perform a two-dimensional parameter estimation problem, estimating both length and depth simultaneously.

5.1 Cost Criterion for Simulated Results

In [4], we performed several trials in which we assumed we had access to various types of data, such as the A field or the $\mathbf{B}$ field at various points (x_i, y_j) in Ω. We compared and contrasted the accuracy to which we could estimate the length l of the damage based on whether the A field or $\mathbf{B}$ field was used and whether we considered the field along a single line, multiple lines or within the entire region (which is not physically possible and was only tested for initial comparisons). In other words, we compared

and contrasted the results using the cost criterions given by either

$$J(l) = \frac{1}{2}\sum_{i=1}^{n}\sum_{j=1}^{m} |10^8 A^N(x_i, y_j, l) - 10^8 \hat{A}(x_i, y_j, l^*)|^2, \tag{5.1}$$

$$J(l) = \frac{1}{2}\sum_{i=1}^{n}\sum_{j=1}^{m} |10^8 B_1^N(x_i, y_j, l) - 10^8 \hat{B}_1(x_i, y_j, l^*)|^2 \tag{5.2}$$

or

$$J(l) = \frac{1}{2}\sum_{i=1}^{n}\sum_{j=1}^{m} |10^8 B_2^N(x_i, y_j, l) - 10^8 \hat{B}_2(x_i, y_j, l^*)|^2 \tag{5.3}$$

where 10^8 is a scaling factor accounting for the low order of magnitude of the field (A is on the order of $10^{-8} Wb/m$), $A^N(l)$ is the reduced order POD approximation to the magnetic vector potential given by (4.3), and $\hat{A}$ is "data" from a sample we wish to characterize. (In this chapter, $\hat{A}$ is obtained from finite element simulations to which noise has been added. Details are given below.) The approximations B_1^N and B_2^N in (5.2) and (5.3) respectively are the components of $\mathbf{B}^N$ given by

$$\mathbf{B}^N(l) = \nabla \times \mathbf{A}^N(l). \tag{5.4}$$

From the results presented in [4], we concluded that extremely accurate results were obtained *only* when the y component B_2 of the magnetic flux density was used in the cost criterion, i.e., when criterion (5.3) was used. We further tested the difference in results when we took snapshots of A versus snapshots on B_2 in the formation of the POD basis elements. The approximation B_2^N was then given either by (5.4) or by using the arguments discussed in Chapter 4 (replacing A by B_2), respectively. There was no significant difference in results as long as the B_2 field was used in the cost criterion. Furthermore, performing multi-line scans or using full region data improved the results only marginally and hence did not warrant the extra effort and time in collecting more extensive data sets. (In the one parameter estimation problems, snapshots of the magnetic vector potential are taken across the *entire* computational domain even though we only consider those points along a single line in the inverse problem.) Consequently the results presented in this dissertation involve only the

least squares difference in the B_2 field given by (5.3) along a single line located $1mm$ above the conducting sheet.

As mentioned above, we simulate data $\hat{B}_2$ using the commercial finite element software package Ansoft Maxwell 2D Field Simulator. However, in order to simulate the random error typically found when using experimental data, we added random noise to the simulated solution. This allowed us to give a more reasonable demonstration of how our algorithm might perform on experimental data.

To generate the noise, we used the Matlab function *randn* which generates a normally distributed set of random numbers with mean 0 and variance 1. A normally distributed set of random numbers has a 65% certainty of being within 1 standard deviation, 95% certainty of being within 2 standard deviations and 99.7% certainty of being within 3 standard deviations of the mean. In other words, there is a 65% chance the Matlab function *randn* will return a number in the interval $(-1, 1)$, 95% chance of returning a number in the interval $(-2, 2)$ and a 99.7% chance of producing a number in the interval $(-3, 3)$. Therefore, we can control the amount of noise in the simulated data by scaling the certainty intervals.

For example, assume we have generated the solution $\hat{A}(\mathbf{q}^*)$ given exact parameters $\mathbf{q}^*$. Furthermore, assume we desire to be 95% certain that the noise generated is within 1% of the actual data $\hat{A}(\mathbf{q}^*)$. At this level of noise, we want to scale the interval $(-2, 2)$ to $(-0.01, 0.01)$. Therefore, letting

$$\epsilon_1 = 0.005 * randn,$$

the data $\tilde{A}$ with 1% relative noise added at a 95% certainty level is given by

$$\tilde{A}(\mathbf{q}^*) = \hat{A}(\mathbf{q}^*)(1 + \epsilon_1).$$

Similarly, if we instead want to be 99.7% certain of noise within 1% of the simulated data, we scale the interval $(-3, 3)$ to $(-0.01, 0.01)$ or let

$$\epsilon_2 = 0.0033 * randn.$$

Data at this noise level is given by

$$\tilde{A}(\mathbf{q}^*) = \hat{A}(\mathbf{q}^*)(1 + \epsilon_2).$$

In the trials performed in [4], we simulated corrupted experimental data by generating noise at a 1% relative noise level with both 95% and 99.7% certainty as discussed above as well as noise at a 5% and 10% relative noise level with both degrees of certainty. There was not a significant improvement in the estimated parameters when the data contained only 1% noise versus 10% noise; therefore, the results in this dissertation only consider data containing 10% relative noise with a 99.7% certainty level.

5.2 Estimating One Parameter

5.2.1 Determining the Length of the Damage

Recall from Section 4.2 that there were two different approaches we considered for forming the reduced order POD approximation, using the POD/Galerkin method or POD/Interpolation method. In determining the length of the damage we consider both of these methods, first examining results obtained with the POD/Galerkin method and then comparing these results to those found with the POD/Interpolation method. In each method we begin by first forming the snapshots of the magnetic vector potential A.

To capture the length, we generated an ensemble of damages keeping the thickness fixed at $2mm$ with various crack lengths $\{l_j\}_{j=1}^{N_s}$ at a fixed depth of $9mm$. We varied the lengths from $0mm$ to $4mm$ in increments of $0.2mm$ resulting in $N_s = 21$ different damages. We then used the commercial software Ansoft Maxwell 2D Field Simulator to generate the snapshots $\{A(l_j)\}_{j=1}^{N_s}$ (finite element solutions to the model derived in Chapter 2).

In the parameter estimation problem we consider the estimation of three different lengths *not* included in those upon which we snapshot. We estimate a length of

$l^* = 1.3mm$, $l^* = 2.5mm$ and $l^* = 5mm$. The first two length values are within the range of those damages included in the snapshots ($0mm \leq l \leq 4mm$). However, $l^* = 5mm$ is outside this interval. In this case, the POD/Interpolation method cannot be used. We must consider POD/Extrapolation. To this end, we use the Matlab routine *interp1* (discussed in Section 4.2) which performs extrapolation for those values outside the given interval when the cubic spline method is the method of choice [45].

Furthermore, as discussed above, "data" is generated using finite element simulations with added random noise. Since the noise is random, we would expect to obtain a different optimized value based upon the noise added. Therefore, we performed 10 trial runs in which 10 different sets of random noise were added to the simulations at a 10% relative noise level (as discussed in Section 5.1). We then calculated the average estimated value and standard deviation across the 10 trials. From these results, we hope to discern how the POD method would work using actual experimental data.

Results Using the POD/Galerkin Method

When comparing the finite element solution for the magnetic flux density to the POD approximation in Section 4.2.1, we determined that the linear system (4.5) became ill-conditioned quickly (Table 4.3). Based on the condition numbers of the linear system as well as graphical representation (Figures 4.1, 4.2 and 4.3), we concluded the optimal choice for N is $N = 3$. If N is chosen much larger, the approximation becomes considerably worse.

Using $N = 3$ when estimating a length of $l^* = 1.3mm$ with no noise added, the optimal value found was $l = 1.2344mm$. Even with 10% relative noise added, there was still very little variation from this optimal value, see Table 5.1.

In the determination of $l^* = 2.5mm$, with no noise added to the data, the optimal value was $2.4121mm$ which resulted in a relative error of 3.52% . Similar to the previous trial, there was only slight fluctuation in the estimated value when 10% noise was added. Table 5.2 gives the optimal values.

Finally, we estimated $l^* = 5mm$ for which we obtained an optimal value of $l = 5.1797mm$ when no noise was added. Table 5.3 give the estimated values when performing the inverse problem using simulated data with 10% relative noise added. In this case, we saw *no* fluctuation in the estimated parameters. Examining the POD/Galerkin method a little closer, we can argue why there may be no fluctuation in the data even with 10% relative noise added.

We would typically expect to see some variation in the estimated parameters when different sets of random noise are added. Indeed we *do* have this variation when we use POD/Interpolation (see below). There are a few differences in the two methods which may play a factor in this redundancy, or lack of, between trials. First of all, recall the form of the linear system we solve in approximating the magnetic flux density, (4.5). The only matrix which changes with each new "guess" is M. However, instead of being able to literally compute M or the integral $\int_\Omega \sigma \Phi_k \overline{\Phi_l} da$, we numerically approximate the integral along the grid using the trapezoidal rule [45]. In general σ is defined by

$$\sigma(x,y) = \begin{cases} \sigma_{cu} &= 5.8 \times 10^7 S/m & \text{for } (x,y) \in cs \\ \sigma_{al} &= 3.72 \times 10^7 S/m & \text{for } (x,y) \in sample \\ \sigma_{air} &= 0 S/m & \text{for } (x,y) \in air \end{cases} .$$

Therefore, the conductivity σ is equal to 3.72×10^{-7} in the majority of the sample except at the location of the damage where σ equals 0. When estimating length alone, keeping the depth fixed at $9mm$ and thickness fixed at $2mm$, we can specifically define the conductivity in the sample for grid points (x_i, y_j) as a function of the estimated parameter l: $\sigma_{sample}(x_i, y_j) = 3.72 \times 10^7$ except for (x_i, y_j), $1 \le i \le n$, $1 \le j \le m$ where $-11 < y_j < -9$ and $0 < x_i < l$. As a result, for all values of l between two adjacent grid points x_i and x_{i+1}, the matrix M is the same, producing identical coefficients in (4.3) and hence the same approximation. Furthermore, the optimization routine goes through the same systematic process for each trial (recall Section 4.3). Therefore, if we start with the same initial guess for each trial and the "data" behaves similarly in each case (since we are adding *relative* noise), we can expect to obtain

similar results across trials, if not exact results, because the optimization routine steps through the same routine, i.e., uses the same set of vertices each time. As a result the estimated value indicates the "best" interval instead of the single best parameter value. To test this theory, we started with different initial guesses for each trial and indeed, the results varied based upon the initial guess.

Table 5.1: Determination of Length $l^* = 1.3mm$ Using POD/Galerkin Method with 10% Relative Noise Added Using $N = 3$

Trial	Est. Length (mm)	Relative Error
1	1.2373	4.82%
2	1.2344	5.05%
3	1.2344	5.05%
4	1.2344	5.05%
5	1.2344	5.05%
6	1.2344	5.05%
7	1.2344	5.05%
8	1.2344	5.05%
9	1.2344	5.05%
10	1.2373	4.82%
Mean (mm) 1.2350	Median (mm) 1.2344	Average Relative Error 5.00 %
Standard Deviation (mm) 0.0012	Variance (mm^2) 0.1526×10^{-5}	

Table 5.2: Determination of Length $l^* = 2.5mm$ Using POD/Galerkin Method with 10% Relative Noise Added Using $N = 3$

Trial	Est. Length (mm)	Relative Error
1	2.4062	3.75%
2	2.4121	3.52%
3	2.4062	3.75%
4	2.4121	3.52%
5	2.4062	3.75%
6	2.4121	3.52%
7	2.4062	3.75%
8	2.4062	3.75%
9	2.4121	3.52%
10	2.4121	3.52%
Mean (mm) 2.4092	Median (mm) 2.4092	Average Relative Error 3.6350 %
Standard Deviation (mm) 0.0031	Variance (mm^2) 0.9537×10^{-5}	

Table 5.3: Determination of Length $l^* = 5mm$ Using POD/Galerkin Method with 10% Relative Noise Added Using $N = 3$

Trial	Est. Length (mm)	Relative Error
1	5.1797	3.59%
2	5.1797	3.59%
3	5.1797	3.59%
4	5.1797	3.59%
5	5.1797	3.59%
6	5.1797	3.59%
7	5.1797	3.59%
8	5.1797	3.59%
9	5.1797	3.59%
10	5.1797	3.59%
Mean (mm) 5.1797	Median (mm) 5.1797	Average Relative Error 3.59%
Standard Deviation (mm) 0	Variance (mm^2) 0	

Results Using the POD/Interpolation Method

In Section 4.2 we compared the accuracy between the POD approximation and the finite element approximation when using the POD/Galerkin method versus the POD/Interpolation method. The POD/Interpolation method was found to produce a more accurate approximation. Consequently we might also expect to obtain more accurate estimates in the inverse problem (we do!). When estimating a length of $l^* = 1.3mm$ using $N = 4$ basis elements with no noise, we obtained an estimated length of $l = 1.2977mm$. (We ran the inverse problem using 1,2,3,4, and 5 POD basis elements with data containing no noise. There was no noticeable difference between using 4 and 5 basis elements; hence, we chose to use 4 basis elements.)

When estimating $l^* = 2.5mm$, the optimal length of $l = 2.4986mm$ was obtained (relative error of 0.69%). Even when the exact parameter value was outside the range of damages upon which we snapshot, the optimized length was still quite accurate. We obtained an optimal value of $l = 4.9763mm$ when estimating $l^* = 5mm$ (relative error 0.47%). Tables 5.4, 5.5, and 5.6 give the corresponding results when the data contains 10% relative error.

Table 5.4: Determination of Length $l^* = 1.3mm$ Using the POD/Interpolation Method with 10% Relative Noise Added Using $N = 4$

Trial	Est. Length (mm)	Relative Error
1	1.2976	0.18%
2	1.3001	0.01%
3	1.3052	0.40%
4	1.3007	0.05%
5	1.2919	0.62%
6	1.3032	0.25%
7	1.2992	0.06%
8	1.2869	1.01%
9	1.3002	0.02%
10	1.2920	0.62%
Mean (mm) 1.2977	Median (mm) 1.2977	Average Relative Error 0.32%
Standard Deviation (mm) 0.0057	Variance (mm^2) 0.3237×10^{-4}	

Table 5.5: Determination of Length $l^* = 2.5mm$ Using the POD/Interpolation Method with 10% Relative Noise Added Using $N = 4$

Trial	Est. Length (mm)	Relative Error
1	2.4984	0.06%
2	2.4952	0.19%
3	2.4990	0.04%
4	2.4957	0.17%
5	2.4998	0.01%
6	2.4979	0.08%
7	2.5002	0.01%
8	2.5016	0.06%
9	2.4972	0.11%
10	2.4974	0.10%
Mean (mm) 2.4982	Median (mm) 2.4981	Average Relative Error 0.08%
Standard Deviation (mm) 0.0020	Variance (mm^2) 0.4056×10^{-5}	

Table 5.6: Determination of Length $l^* = 5mm$ Using the POD/Interpolation Method with 10% Relative Noise Added Using $N = 4$

Trial	Est. Length (mm)	Relative Error
1	4.9788	0.42%
2	4.9882	0.24%
3	4.9775	0.45%
4	4.9754	0.49%
5	4.9726	0.55%
6	4.9767	0.47%
7	4.9704	0.59%
8	4.9849	0.30%
9	4.9873	0.25%
10	4.9705	0.59%
Mean (mm) 4.9782	Median (mm) 4.9771	Average Relative Error 0.44%
Standard Deviation (mm) 0.0066	Variance (mm^2) 0.4325×10^{-4}	

5.2.2 Determining the Thickness of the Damage

In determining the thickness of the damage, we proceed as we did in estimating the length of a damage, we generated an ensemble of cracks with varying thickness ranging from $0mm$ to $4mm$ in increments of $0.2mm$, $\{h_j\}_{j=1}^{N_s}$ ($N_s = 21$) keeping the crack length fixed at $2mm$ with fixed depth $9mm$. For each h_j, $j = 1, ..., N_s$, we have the corresponding solutions $\{A(h_j)\}_{j=1}^{N_s}$. Similar to our findings when taking snapshots on the length of a damage, 99.99% of the energy was captured in a single basis element when we took snapshots of A (Table 5.7). Furthermore, when taking snapshots on the B_2 field, we still captured 99% of the energy with only one basis element (Table 5.8).

When estimating the length of the damage in the previous section, only 4 basis elements were required to achieve an estimate with an accuracy of order $10^{-3}mm$. However, even though 99% of the energy is captured in a single basis element regardless of whether we snapshot on A or B_2 (Tables 5.7 and 5.8), more basis elements (at least 8) were required to achieve the same level of accuracy when estimating a thickness of $h = 1.3mm$. Therefore, we used 9 POD basis elements.

Table 5.7: Energy Captured with N Basis Elements using Snapshots of A while Varying Thickness

N	Energy Captured
1	99.999446453503%
2	99.999999666469%
3	99.999999935840%
4	99.999999961479%
5	99.999999972048%
6	99.999999980054%
7	99.999999984470%
8	99.999999987779%
9	99.999999990521%
10	99.999999992316%

With no noise added we obtained an optimal thickness of $h = 1.3036mm$. Although more basis elements were used, the total time required to complete the inverse

problem was still only 8 seconds. Furthermore, the results were accurate even in the presence of 10% noise, obtaining an average thickness of $1.3041mm$ with variance $0.2883 \times 10^{-4}mm^2$, see Table 5.9. Thus, just as in estimating the length of a crack, we can also recapture the thickness of a crack quite accurately and efficiently.

Table 5.8: Energy Captured with N Basis Elements using Snapshots of B_2 while Varying Thickness

N	Energy Captured
1	99.488023435913%
2	99.728234129540%
3	99.799825670140%
4	99.836722535293%
5	99.870058186819%
6	99.896958827131%
7	99.911070207772%
8	99.923141472559%
9	99.934263323537%
10	99.944776176825%

Table 5.9: Determination of Thickness $h^* = 1.3mm$ Using POD/Interpolation Method with 10% Relative Noise Added Using $N = 9$

Trial	Est. Length (mm)	Relative Error
1	1.3058	0.45%
2	1.3069	0.53%
3	1.3124	0.95%
4	1.2952	0.37%
5	1.3072	0.55%
6	1.3054	0.42%
7	1.2997	0.02%
8	1.3024	0.18%
9	1.2973	0.21%
10	1.3087	0.67%
Mean (mm)	Median (mm)	Average Relative Error
1.3041	1.3056	0.44%
Standard Deviation (mm)	Variance (mm^2)	
0.0054	0.2883×10^{-4}	

5.2.3 Determining the Depth of the Damage

In the field of electromagnetic nondestructive evaluation, researchers are continually trying to develop methods to detect damages located deep within a sample. Typically this is not possible due to the skin effect problem discussed in Chapter 6. Therefore, in this section we test our proposed methodology on several examples, trying to determine at what depth the estimation problem breaks down.

The first step in the estimation problem is to form snapshots of the magnetic vector potential as it varies with depth. Keeping the length fixed at $1.5mm$ and thickness fixed at $0.5mm$, we took snapshots on A for damages with depths ranging from $0.25mm$ to $19.25mm$ in increments of $0.5mm$ ($N_s = 39$ total snapshots). As usual, we examine the total energy captured when taking snapshots of A (Table 5.10) as well as that when taking snapshots of B_2 (Table 5.11). There is a significant difference in the energy captured depending on the choice. We noted previously that since we are using the magnetic flux density (more precisely B_2) in the inverse problem, it may be more accurate to look at the energy captured when taking snapshots of B_2 since this is associated with the energy stored in the magnetic field. Hence, the results in Table 5.11 seems to indicate that we must consider at least 7 POD basis elements if we want to capture at least 99% of the energy and even more basis elements are needed ($N = 20$) to capture 99.9% energy.

Table 5.10: Energy Captured with N Basis Elements using Snapshots of A while Varying Depth

N	Energy Captured
1	99.999956610233%
2	99.999994678147%
3	99.999998147470%
4	99.999999108470%
5	99.999999489923%
6	99.999999678331%
7	99.999999778790%
8	99.999999839735%
9	99.999999877726%
10	99.999999903696%

To test the accuracy of the results of the inverse problem with varying N, we compared the results with no noise using $N = 3$ to $N = 20$ reduced basis elements. The tables for these results are in Appendix B. Examining the tables, there is no *one* value of N which gives a "best" estimate for all the parameters. In some cases, using $N = 5$ or 6 produced as accurate (or more accurate) results as when using larger values of N. In other cases, it was obvious that it was necessary to choose a larger value of N. Since there is no "best" choice for N, we present results for the parameter estimation problem for various depths when no noise is added using both $N = 5$ (Table 5.12) and $N = 10$ (Table 5.13).

Table 5.11: Energy Captured with N Basis Elements using Snapshots of B_2 while Varying Depth

N	Energy Captured
1	74.613031947466%
2	89.514149513603%
3	94.706717888657%
4	96.922534304401%
5	98.035727130657%
6	98.664029837829%
7	99.044118008519%
8	99.288547725895%
9	99.451819020654%
10	99.567635237611%
11	99.652287106881%
12	99.713493423703%
13	99.761516459832%
14	99.798666688295%
15	99.827616663002%
16	99.850749554168%
17	99.869399850177%
18	99.885070376390%
19	99.897962625941%
20	99.908211078470%

We first note that when estimating depth the relative error does not truly indicate the accuracy of the estimation. For example, in Table 5.12, an approximation of $d = 1.0603mm$ for $d^* = 1mm$ results in a relative error of 6.03%. However, in the same table, an estimate of $d = 12.5207mm$ for $d^* = 13mm$ only calculates to a 3.69% error, almost half that for the estimation for $1mm$. However, looking at the actual error, it is obvious that we obtained a better estimate for $d^* = 1mm$ than for $d^* = 13mm$. Therefore, when examining these tables, it is important to not only look at the relative error but to also take into account the actual estimated value to discern whether or not an estimate would be considered "good".

Table 5.12: Determination of Depth with No Noise Added Using $N = 5$

Depth (mm)	Est. Depth (mm)	Relative Error
1	1.0603	6.03%
2	2.1396	6.98%
3	3.0359	1.20%
4	4.0379	0.95%
5	4.8333	3.33%
6	5.9103	1.50%
7	7.0592	0.85%
8	8.0659	0.82%
9	9.0200	0.22%
10	9.9888	0.11%
11	10.9199	0.73%
12	11.8120	1.57%
13	12.5207	3.69%
14	14.0560	0.40%
15	16.0989	7.33%
16	16.0123	0.08%
17	16.7500	1.47%

Table 5.13: Determination of Depth with No Noise Added Using $N = 10$

Depth (mm)	Est. Depth (mm)	Relative Error
1	1.0103	1.04%
2	1.9874	0.63%
3	3.0145	0.48%
4	4.0421	1.05%
5	4.9800	0.40%
6	5.9877	0.21%
7	7.0552	0.79%
8	7.9027	1.22%
9	9.0400	0.45%
10	9.8426	1.57%
11	11.0770	0.70%
12	12.0331	0.56%
13	12.4272	4.41%
14	13.9253	0.53%
15	14.3702	4.20%
16	17.7241	10.78%
17	17.8303	4.88%

In general, it is not obvious that the estimation becomes worse when trying to estimate a deeper damage as opposed to a shallow damage as one would expect. Instead, the accuracy of the estimate depends in part on the number of basis elements used in the approximation. For example, when using $N = 5$ basis elements, we obtained an estimate of $16.0123mm$ for a true depth of $d^* = 16mm$. However, when we use an approximation with $N = 10$ basis elements, we obtained a poor estimate, resulting in an estimated parameter value of $17.7241mm$, a 172.41% actual error. This pattern of variation can be seen even more clearly when examining the full set of tables in Appendix B. In general, when estimating depths from $d^* = 1mm$ to $d^* = 8mm$, using any N greater than $N = 6$ results in an estimate with an actual error less than approximately 10% (relative error less than 6%). One exception to this is for $d^* = 6mm$, in which we must use between $N = 5$ and $N = 15$ POD basis elements to achieve the same level of accuracy; however, the error is still less than 15% for values

of N greater than 15 (relative error less than 2.6%). For depths past $d^* = 8mm$, we can not make such overall conclusions; the results vary depending on depth. In general, it was difficult to estimate depths $d^* = 10mm$, $13mm$ and $15mm$. However, except for a few choices of N, we could fairly accurately estimate $d^* = 11mm$, $12mm$ and $14mm$. Due to the variation in the estimated parameter in these cases, it is not reasonable to conclude that we will always obtain an accurate estimate. To account for this variation, it would be possible to use two or three different values of N in the inverse problem, obtaining two or three different estimates, and compare these results. This *should* give a fairly accurate indication of the "true" depth. Thus, in general we could use the reduced order POD method in conjunction with the inverse problem and obtain accurate results, keeping in mind the possibility of performing the inverse problem a few times (two or three) for different values of N to obtain the most accurate results. We note that this approach (performing the inverse problem 2-3 times) would *still* be less time consuming than using a finite element routine (as discussed in the conclusions).

Even with 10% relative noise added to the data, we obtain just as accurate results. Tables 5.14, 5.15 and 5.16 give results obtained for estimating $d^* = 3mm$, $d^* = 8mm$ and $d^* = 11mm$ when 10% relative noise is added to the data using $N = 5$ basis elements with initial guesses of $0.5mm$ and $19mm$ (two are required in the one-parameter estimation problem using Nelder-Mead). In each case, the average across the trials is extremely close to the optimal parameter obtained when no noise is added to the data. This is true for all the depths tested, see Appendix B. Therefore, noise does not seem to hinder the accuracy of the approximation. Based upon these results as well as those when estimating length and thickness, we can assume we would obtain similar results with noise when using $N = 10$ basis elements.

Table 5.14: Determination of Depth $d^* = 3mm$ with 10% Relative Noise Added Using $N = 5$

Trial	Est. Depth (mm)	Relative Error
1	3.0438	1.46%
2	3.0247	0.82%
3	3.0350	1.17%
4	3.0487	1.62%
5	3.0397	1.32%
6	3.0347	1.16%
7	3.0341	1.14%
8	3.0165	0.55%
9	3.0157	0.52%
10	3.0445	1.48%
Mean (mm) 3.0337	Median (mm) 3.0349	Average Relative Error 1.12%
Standard Deviation (mm) 0.0115	Variance (mm^2) 0.1316×10^{-3}	

Table 5.15: Determination of Depth $d^* = 8mm$ with 10% Relative Noise Added Using $N = 5$

Trial	Est. Depth (mm)	Relative Error
1	8.0616	0.77%
2	8.0612	0.77%
3	8.0827	1.03%
4	8.0622	0.78%
5	8.0640	0.80%
6	8.0599	0.75%
7	8.0746	0.93%
8	8.0746	0.93%
9	8.0431	0.54%
10	8.0705	0.88%
Mean (mm) 8.0654	Median (mm) 8.0631	Average Relative Error 0.82%
Standard Deviation (mm) 0.0109	Variance (mm^2) 0.1180×10^{-3}	

Table 5.16: Determination of Depth $d^* = 11mm$ with 10% Relative Noise Added Using $N = 5$

Trial	Est. Depth (mm)	Relative Error
1	10.9262	0.67%
2	10.9143	0.78%
3	10.9039	0.87%
4	10.9112	0.81%
5	10.9379	0.56%
6	10.9173	0.75%
7	10.9243	0.69%
8	10.9173	0.75%
9	10.9365	0.58%
10	10.9195	0.73%
Mean (mm) 10.9208	Median (mm) 10.9184	Average Relative Error 0.72%
Standard Deviation (mm) 0.0107	Variance (mm^2) 0.1140×10^{-3}	

5.3 Estimating Two Parameters

In Chapter 6 we discuss in detail a need to modify the assumptions made in the original test problem to more accurately describe the behavior of experimental data obtained. In short, the computational domain was expanded beyond the edges of the sample and snapshots were taken of the magnetic flux density data on a single line above the conducting sheet (instead of the whole region). Recall that for the previous trials, we took snapshots of the magnetic vector potential for the entire computational domain even though in the inverse problem we only considered those data points along a single line. Furthermore, we considered data across the entire length of the sample, instead of just half the sample as done previously. (For more details , see Chapter 6.) As a result, we also implement these changes in the two parameter estimation problem.

We proceed as in the previous estimation problems by first generating an ensemble of damages. We consider damages with depths ranging from $1mm$ to $11mm$ in

increments of $2mm$ in combination with lengths from $0.5cm$ to $3.5cm$ in increments of $1cm$ (we now consider longer damages similar to those in Chapter 6). We keep the thickness fixed at $1mm$. A total of 24 snapshots, $\{B_2(d_i, l_j)\}$, $i = 1, ..., 6$, $j = 1, ..., 4$ were generated using Ansoft. Table 5.17 gives the percentage of energy captured (with snapshots on B_2).

Table 5.17: Energy Captured with N Basis Elements using Snapshots of B_2 while Varying Length *and* Depth

N	Energy Captured
1	83.134099453827%
2	97.439835438162%
3	99.618220536322%
4	99.921868550302%
5	99.995557011122%
6	99.997533916202%
7	99.998810647161%
8	99.999589493622%
9	99.999802712183%
10	99.999905405763%

Using (5.3) with $N = 4$ (as indicated from the table above), we obtain the results in Table 5.18 when no noise is added with the associated relative error given in Table 5.19. In each case, the POD method in conjunction with the inverse problem again provided extremely accurate results. We only consider a few representative length/depth combinations when estimating parameters with 10% relative noise added. We estimate a depth of $d^* = 2mm$ in conjunction with a length of $l^* = 1cm$, depth $d^* = 4mm$ with length $l^* = 2cm$, and finally a depth of $d^* = 6mm$ with a length $l^* = 3cm$. In each case, the POD method performed remarkably well even in the presence of considerable noise.

Table 5.18: Determination of Depth *and* Length Simultaneously

		Actual Length l^*		
		1cm	2cm	3cm
Actual Depth d^*	2mm	$l = 1.0184$ $d = 2.0484$	$l = 2.0106$ $d = 2.0035$	$l = 3.0686$ $d = 2.0234$
	4mm	$l = 0.9387$ $d = 4.0730$	$l = 1.9799$ $d = 4.0866$	$l = 3.0560$ $d = 4.1080$
	6mm	$l = 0.9642$ $d = 6.0199$	$l = 1.9692$ $d = 5.9433$	$l = 3.0370$ $d = 6.0288$
	8mm	$l = 1.0135$ $d = 8.1512$	$l = 1.9885$ $d = 8.1046$	$l = 3.0259$ $d = 8.1205$
	10mm	$l = 1.0090$ $d = 9.9954$	$l = 1.9763$ $d = 9.9707$	$l = 3.0032$ $d = 9.9866$

Table 5.19: Relative Error in Determination of Depth *and* Length

		Actual Length l^*		
		1cm	2cm	3cm
Actual Depth d^*	2mm	$R_l = 1.84\%$ $R_d = 2.42\%$	$R_l = 0.53\%$ $R_d = 0.18\%$	$R_l = 2.29\%$ $R_d = 1.17\%$
	4mm	$R_l = 6.13\%$ $R_d = 1.83\%$	$R_l = 1.01\%$ $R_d = 2.17\%$	$R_l = 1.87\%$ $R_d = 2.70\%$
	6mm	$R_l = 3.58\%$ $R_d = 0.33\%$	$R_l = 1.54\%$ $R_d = 0.95\%$	$R_l = 1.23\%$ $R_d = 0.48\%$
	8mm	$R_l = 1.35\%$ $R_d = 1.89\%$	$R_l = 0.58\%$ $R_d = 1.31\%$	$R_l = 0.86\%$ $R_d = 1.51\%$
	10mm	$R_l = 0.90\%$ $R_d = 0.05\%$	$R_l = 1.19\%$ $R_d = 0.29\%$	$R_l = 0.11\%$ $R_d = 0.13\%$

Table 5.20: Determination of Depth $d^* = 2mm$ and Length $l^* = 1cm$ Simultaneously with 10% Relative Noise Added to Data

Trial	Est. Depth (mm)		Est. Length (cm)	
1	2.0437		1.0204	
2	2.0526		1.0233	
3	2.0444		1.0130	
4	2.0500		1.0321	
5	2.0508		1.0137	
6	2.0446		1.0131	
7	2.0433		1.0127	
8	2.0549		1.0141	
9	2.0417		1.0058	
10	2.0465		1.0318	
	Mean (mm) 2.0473	Median (mm) 2.0456	Mean (cm) 1.0180	Median (cm) 1.0139
	Stand. Dev. (mm) 0.0045	Var. (mm^2) 0.2035×10^{-4}	Stand. Dev. (cm) 0.0087	Var. (cm^2) 0.7583×10^{-4}

Table 5.21: Determination of Depth $d^* = 4mm$ and Length $l^* = 2cm$ Simultaneously with 10% Relative Noise Added to Data

Trial	Est. Depth (mm)		Est. Length (cm)	
1	4.0793		1.9795	
2	4.0731		1.9762	
3	4.0847		1.9887	
4	4.0944		1.9724	
5	4.0776		1.9719	
6	4.0788		1.9775	
7	4.0918		1.9747	
8	4.0912		1.9704	
9	4.0863		2.0015	
10	4.0924		1.9878	
	Mean (mm) 4.0850	Median (mm) 4.0855	Mean (cm) 1.9801	Median (cm) 1.9769
	Stand. Dev. (mm) 0.0074	Var. (mm^2) 0.5516×10^{-4}	Stand. Dev. (cm) 0.0098	Var. (cm^2) 0.9632×10^{-4}

Table 5.22: Determination of Depth $d^* = 6mm$ and Length $l^* = 3cm$ Simultaneously with 10% Relative Noise Added to Data

Trial	Est. Depth (mm)		Est. Length (cm)	
1	6.0346		3.0452	
2	6.0340		3.0420	
3	6.0334		3.0460	
4	6.0252		3.0302	
5	6.0328		3.0336	
6	6.0290		3.0378	
7	6.0301		3.0350	
8	6.0322		3.0455	
9	6.0296		3.0427	
10	6.0355		3.0377	
	Mean (mm) 6.0316	Median (mm) 6.0325	Mean (cm) 3.0396	Median (cm) 3.0399
	Stand. Dev. (mm) 0.0031	Var. (mm^2) 0.0990×10^{-4}	Stand. Dev. (cm) 0.0055	Var. (cm^2) 0.3045×10^{-4}

5.4 Conclusions

In this chapter we tested the computational methodology formulated in the previous chapter by trying to estimate a damage using simulated data containing random relative noise. When using the B_2 field in the inverse problem, the methods proved to be accurate and robust, allowing us to accurately estimate the length, thickness, and depth of a damage within a sample as well as length and depth simultaneously even when the data contained considerable noise.

There are two significant findings with regard to the above results. First of all, in most cases *we were able to use 10 POD basis elements or less in each of the trials performed. We compare this to a total of over 7000 finite elements required to solve the boundary value problem initially* (using Ansoft Maxwell 2D Field Simulator). Hence, if one were to use the finite element software for each forward run, we could expect a time-intensive inverse problem. This leads us to the most *significant* finding with

regard to reduction in computational time which can be summarized as follows. If one were to use a software package such as Ansoft's Maxwell 2D Field Simulator to calculate the forward problem each time it is required in the inverse problem, it would take approximately 5-7 minutes for a *single* forward solve and hence any inverse algorithm based on this forward solver may require several minutes to several *hours* of time for the optimization problem. In using the reduced order POD methodology for the forward problem, the *entire inverse problem* takes approximately 8 seconds, less than $\frac{1}{40}$ the time required for a *single forward simulation.* As a forward algorithm is called numerous times, this is a substantial reduction in time required. For example, assuming an average of 20 iterative steps in the typical optimization procedure for these problems and a total forward simulation time of 5 minutes (300 seconds) to 7 minutes (420 seconds) for a finite element forward solve, the total computational time for the inverse problem would range from 1 hour 40 minutes (6000 seconds) to 2 hours 20 minutes (8400 seconds). Thus, we arrive at a speed up factor ranging from 750 to 1050, a factor of about 10^3.

Furthermore, most of the extensive computational time is required only in the initial collection of snapshots which would take place prior to implementation in a practical setting. This suggests that a *portable sensing device, when coupled with reduced order modeling in the inverse problem, might be plausible in practical damage detection applications.*

Chapter 6

Experimental Results

The simulations performed in Chapter 5 suggest a need to further our study with actual experimental data. Therefore, as the next step, we designed the experiment depicted in Figure 6.1, in which we try to detect and parameterize a damage within an aluminum sample using a giant magnetoresistive (GMR) sensor.

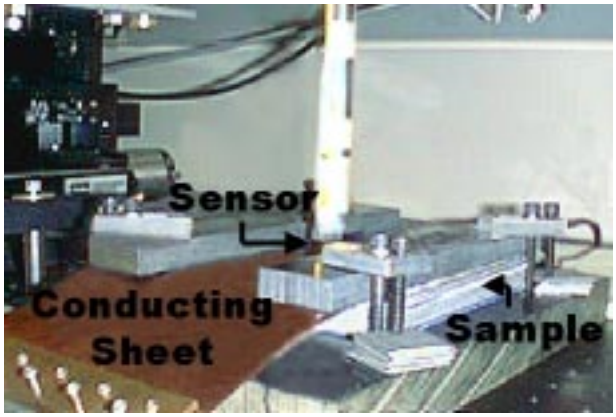

Figure 6.1: Experimental Setup

The sample is constructed of 17 layers of $1mm$ thick aluminum plates with a slice cut out of one of the layers to simulate a damage within the sample (see Figure 6.2). The "damaged" piece of aluminum is moved from one layer to another to simulate damages within the sample at different depths, and the length of the damage is varied by producing "gaps" of varying size from the aluminum plate (the thickness of the damage is always fixed at $1mm$). As a means of inducing current within the sample,

a thin sheet of copper carrying a uniform current of $3A$ is placed above the sample on top of a thin sheet of paper (to avoid direct physical contact between the sample and the conducting sheet). The GMR sensor measures the amplitude and phase of the magnetic flux density across a $2in$ line (along the length of the sample) every $0.635mm$. The data is then filtered through a lock-in amplifier and saved to a file.

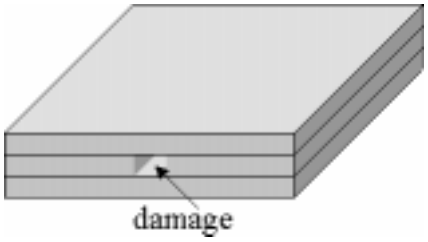

Figure 6.2: Schematic of the Damaged Layer

Given magnetic flux density data, $\hat{B}_2$, from the GMR sensor for a given damage at a specified depth d^* and with a given length l^*, we wish to estimate these parameters using the cost criterion,

$$J(\mathbf{q}) = \frac{1}{2}\sum_{j=1}^{n}\left|10^8 B_2^N(x_j;\mathbf{q}) - 10^8\hat{B}_2^j\right|^2 \tag{6.1}$$

where $\mathbf{q}$ is the vector containing the parameters we wish to estimate, $B_2^N(\mathbf{q})$ is the POD approximation described in Section 4.1 and $\hat{B}_2^i$ is GMR data at grid points x_j, $j = 1, ..., n$ with n total grid points. The first step in the optimization process is to generate snapshots representative of the experimental data across the various damages.

6.1 Comparison of Experimental Data and Ansoft Simulations

To generate the snapshots, we first explore the idea of using simulations obtained from the finite element solver Ansoft Maxwell 2D Field Simulator to form the POD basis elements as done in the previous chapter. However, in order for the snapshots to be

representative of the data, we needed to modify the assumptions made in the original test problem. We had originally assumed a sample of infinite length to disregard boundary effects from the edges of the material. Unfortunately, the experimental data showed significant boundary effects. Therefore, we modified the computational domain used in the finite element solver as depicted in Figure 6.3 to include the edges of the sample. Moreover, instead of only considering half of the sample, we now consider data across the entire length of the sample as done in the experimental setup.

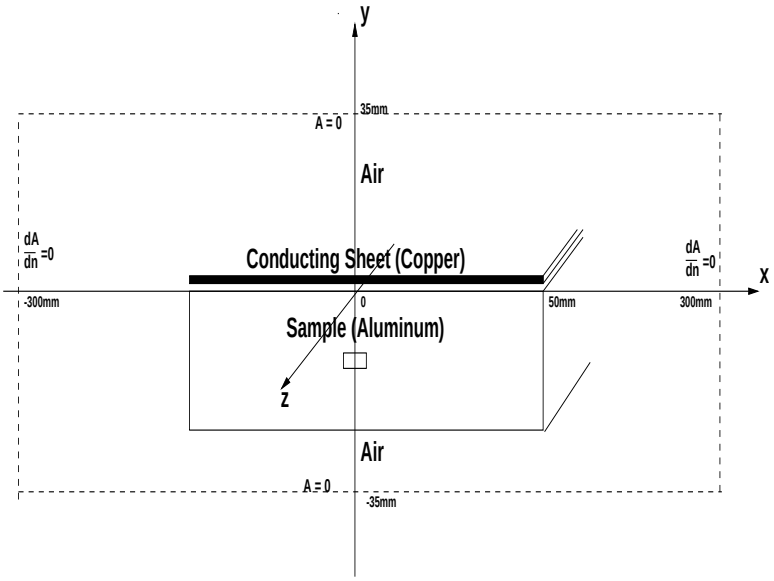

Figure 6.3: Altered Schematic of Problem

Using the cost criterion in (6.1) with the POD approximation formed with snapshots of Ansoft finite element simulations, we tried to recapture the length of the damage alone. However, we were unsuccessful. Trying to estimate a length of $l^* = 1cm$, we obtained an optimal value of $l = 2.4792cm$ when keeping the depth fixed at $1mm$ (layer 2) and an optimal value of $l = 2.2445cm$ with a fixed depth of $2mm$ (layer 3). After analyzing the experimental data and the Ansoft simulations, we noticed significant differences between the data and simulations, shown in Figure 6.4.

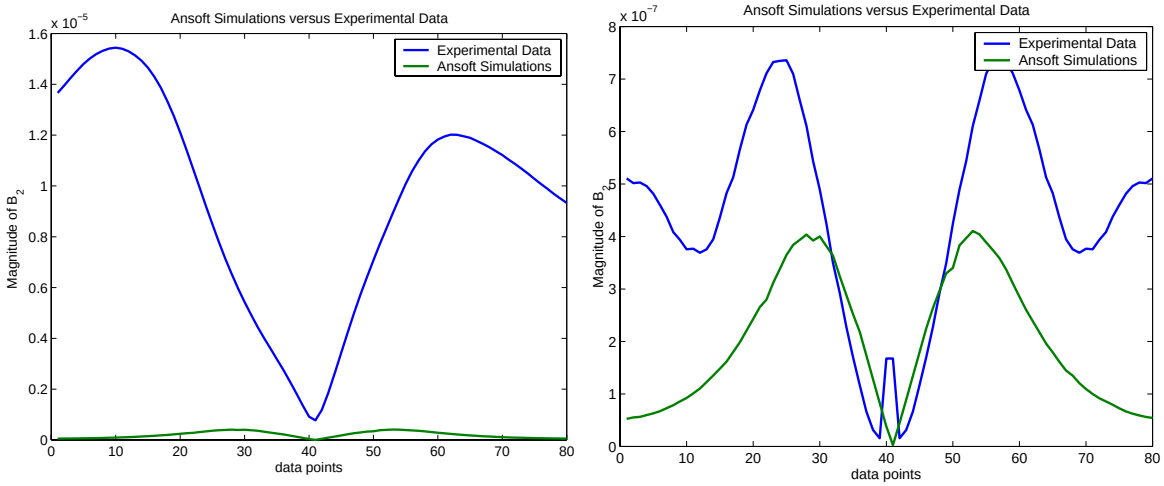

Figure 6.4: Comparison of Experimental Data and Ansoft Simulations for a Sample Containing a Damage $2mm$ Deep with a Length of $1.5cm$ at a Frequency of $350Hz$: The first plot compares Ansoft finite element simulations to raw experimental data. The second plot compares Ansoft finite element simulations to experimental data which has been modified by filtering out the background noise and averaging the magnitude across the center.

The first plot in Figure 6.4 shows the magnitude of the magnetic flux density for the raw experimental data compared to Ansoft simulations for a sample containing a damage $2mm$ deep with a length of $1.5cm$. We first note the scale of the amplitude does not match that of the simulations. Furthermore, the magnitude of the experimental data is not symmetric about the center of the damage. To adjust for these inconsistencies, we filtered out the background noise (data obtained when the sample contained no damage) and averaged the experimental data across the center of the damage. In other words, data to the left of the center was averaged with the transversed data to the right of the center to find the average magnitude. If $|\hat{B}_2^j|$ denotes the magnitude of the data at point x_j, then the magnitude after averaging is given by

$$|\hat{B}_2^j|_{avg} = \frac{1}{2}\left(|\hat{B}_2^j| + |\hat{B}_2^{n-j+1}|\right). \tag{6.2}$$

The second plot in Figure 6.4 compares Ansoft simulations to the experimental data after the modifications. There was a significant improvement; however, in order to

use the POD methodology, the snapshots must be a *good* representation of the data we wish to estimate.

Based upon the comparisons between Ansoft simulations and GMR data, there is an obvious discrepancy between the model we are using in Ansoft and the data. We offer some speculative reasons as to why the model may not accurately represent the experimental design. First of all, although we tried to mimic the two-dimensional test problem when designing the experiment, there may be certain three-dimensional effects that cannot be accurately captured with the two-dimensional model. Another possible reason may be inconsistencies between the material attributes of the actual design and those used in the simulations. Indeed, in the development and testing of the Galerkin/POD method discussed in Chapter 4, slight variations in the conductivity produced observable differences in the solution. In addition, the model does not incorporate the cables, equipment and other varying factors in the room which may also contribute to and cause variation in the magnetic flux density. Although these are possible reasons for the discrepancies, we do not explore these ideas at this time. However, until a model is designed which mimics the experimental data more closely, the simulations from the model cannot be used to form the POD approximation used in the inverse problem. Consequently, we chose to instead snapshot on the experimental data to form the POD basis elements.

First, we make one final comparison between Ansoft simulations and the experimental data. In Section 2.3, Figure 2.5, the magnitude of the magnetic flux density was plotted on a line above the conducting for samples containing damages of varying lengths. This figure depicted a definite pattern in the magnitude as a function of the length of the damage. This pattern seems to be important in estimating the magnetic flux density using the POD/Interpolation method. After closer examination of the data, we discovered that unlike Ansoft finite element simulations, there was no consistent pattern in the experimental data when varying the length of the damage within the sample, Figure 6.5.

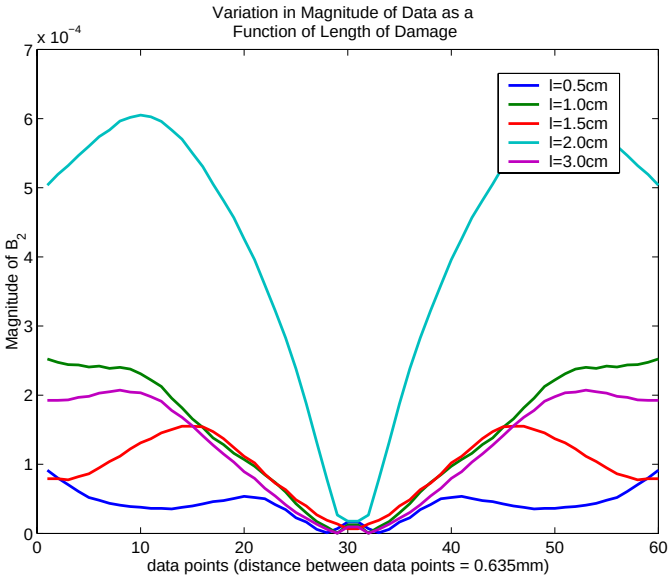

Figure 6.5: Initial Lack of Pattern in Experimental Data when Varying the Length of the Damage Keeping the Depth Fixed at 2mm (layer 3) Using a Frequency of 350Hz

We attributed the lack of pattern in the data to many factors. When we were taking the data we noticed that any perturbation in realignment from one scan to the next resulted in significant variation of the data. This was a problem since we had to dismantle the experimental setup each time we changed the damage within the sample. Consequently, there could be a noticeable variation in the data when changing from one damage to another that might be a result of perturbations in either the sample or conducting sheet as well as variation in the damage. Furthermore, if the conducting sheet was scratched slightly, the flow of the current would be altered which also produced variation in the data. In other words, there may be other factors affecting the the data instead of only the damage itself. To minimize these variations, the experimental design was made more stable by fixing the location of the sample and conducting sheet. Therefore, we knew from one scan to the next (from one damage to the next), the sample and conducting sheet were reassembled in the exact same position. In addition, a thicker piece of copper which could not be as easily scratched or bent was used. One other factor we considered was the amount of background

noise in the data. To filter out some of the noise, the GMR sensor was shielded, as in [54, 55]. With all these alterations in the design, new data was collected in a series of experiments. Figure 6.6 shows a noticeable pattern in the new data; there is a consistent increase in the maximum magnitude and location of the magnetic flux density as the length of the damage in the sample increases.

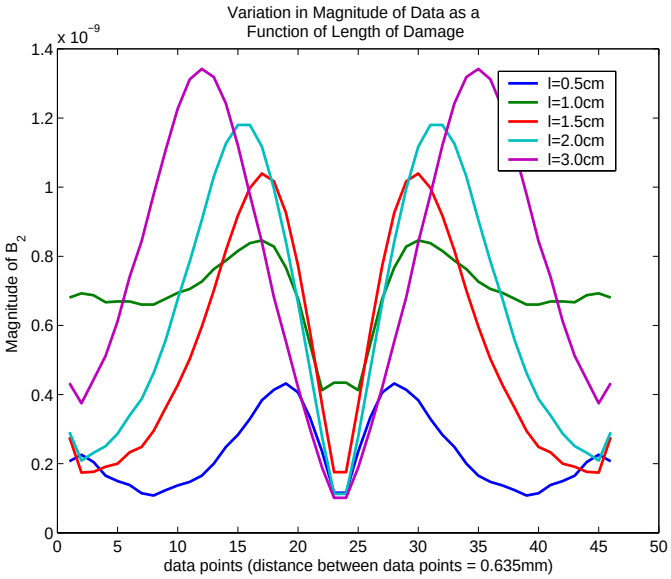

Figure 6.6: Pattern of Experimental Data when Varying the Length of the Damage Keeping the Depth Fixed at 2mm (layer 3) Using a Frequency of 500Hz

6.2 Analysis of the Data at Various Frequencies

Data was subsequently taken for samples with damages at depths $1mm$, $2mm$, $3mm$, $4mm$, $6mm$ and $8mm$ with lengths $0.5cm$, $1cm$, $1.5cm$, $2cm$, and $3cm$ at frequencies 250Hz, 500Hz, 1kHz and 2kHz. In this section, we analyze the similarities and differences between these data sets when only the source frequency is altered. This will give us a basis for the parameter estimation problem discussed in the next section.

6.2.1 Depth of Penetration

Frequency is a very important factor to consider when trying to detect and parameterize a damage. This is due to the depth of penetration of the eddy currents, also referred to as the "skin effect". Eddy currents are not uniformly distributed throughout a material but instead decay exponentially with depth in the material [42]. The distance at which the eddy current density has decreased by a factor of $1/e$ (36.8%) is called the *depth of penetration* and can be calculated by

$$\delta = \frac{1}{\sqrt{\pi f_s \mu \sigma}} \tag{6.3}$$

where f_s is the source frequency, μ is the magnetic permeability and σ is the conductivity of the material [12, p. 370]. Table 6.1 gives the calculated depth of penetration for the frequencies considered in this paper associated with the aluminum alloy used in the experimental design (aluminum alloy 2024, with heat treatment T4 or Al2024-T4; conductivity $1.734 * 10^7 S/m$).

Table 6.1: Depth of Penetration for Aluminum Alloy 2024-T4 for Various Frequencies

Frequency (Hz)	δ (mm)
250	7.64
500	5.41
1000	3.82
2000	2.70

In general, at higher frequencies the currents can be considered to be confined to the very top layers of the conducting surface thus making the task of estimating a damage at deeper depths quite difficult. However the sensitivity to the detection of discontinuities is relatively high for these frequencies. On the other hand, at lower frequencies the eddy currents are not as concentrated (they are more spread out) and therefore can penetrate deeper within the sample. Thus, using lower frequencies seems to be more feasible when estimating deeper damages; however, the deeper the depth of penetration, the less sensitive the fields are to the detection of discontinuities [11]. Consequently, it is often difficult to determine the "best" frequency for a problem.

6.2.2 Analysis of Data Using Raw Phase Information

We begin by analyzing the similarities and differences of the magnetic flux density data for samples containing damages with a fixed depth of $3mm$ and varying lengths. We will assume initially that the only modifications made to the data are the modifications in the amplitude discussed in Section 6.1. In other words, for data points x_j, we use the raw phase data, θ_j, $j = 1, ..., n$, and the modified amplitude $|\hat{B}_2^j|_{mod}$, $j = 1, ..., n$, in which the the amplitude has been averaged across the center of the damage and the background noise has been filtered out. (Although we are not using Ansoft to form our POD basis elements, these modifications are still necessary for the data to exhibit the pattern in Figure 6.6, a pattern which we have already noted was important in forming the POD approximation $B_2^N(\mathbf{q})$.)

Figures 6.7 - 6.10 display plots of the complex magnetic flux density data, real and imaginary parts respectively, for frequencies 250Hz (Figure 6.7), 500Hz (Figure 6.8), 1kHz (Figure 6.9) and 2kHz (Figure 6.10). In order to use the POD/Interpolation method for the POD approximation (the option of choice since we aren't using the model, recall Chapter 4), there must be a consistent pattern in the data between consecutive parameter values. Unfortunately, not all of the data contains the desired pattern.

When using a source frequency of 250Hz (Figure 6.7), the real part of the magnetic flux density does display a fairly uniform pattern in the location and value of the maximum and minimum when varying the length. Both the distance between the maximum and minimum and the absolute value of the maximum and minimum increase as the length of the damage increases. On the other hand, the imaginary portion is random with no observable pattern between the data and the length of the damage. This fortunately is not the case when using a source frequency of 500Hz (Figure 6.8). In this case, *both* the real and imaginary parts of the magnetic flux density exhibit a consistent pattern similar to the pattern in the real part of the data using 250Hz. In addition, the pattern seems to be even more uniform for 500Hz than for 250Hz with a more constant increase in the absolute value of the maximum and

minimum between consecutive lengths.

In Figure 6.9 the real and imaginary parts of the magnetic flux density are plotted for a source frequency of 1kHz. In this case, similar to the case for 250Hz, there is only a pattern in one component of the data. The imaginary part displays a partial pattern while the real part is random. However, in the previous two cases (250Hz and 500Hz), both the location and the absolute value of the maximum and minimum varied as a function of the length of the damage.

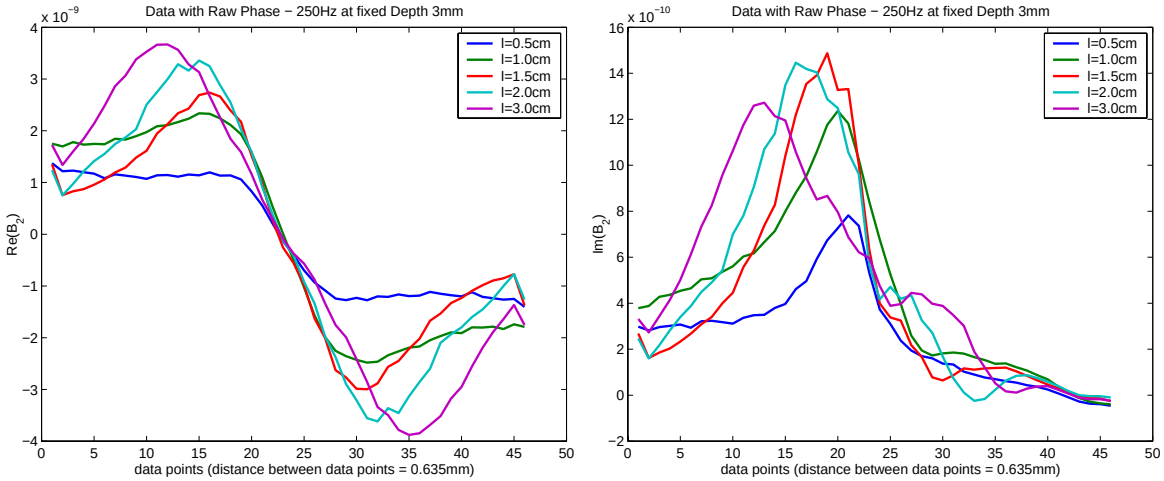

Figure 6.7: Variation in Complex Data as a Function of Length of the Damage using a Frequency of 250Hz While Keeping the Depth Fixed at $3mm$

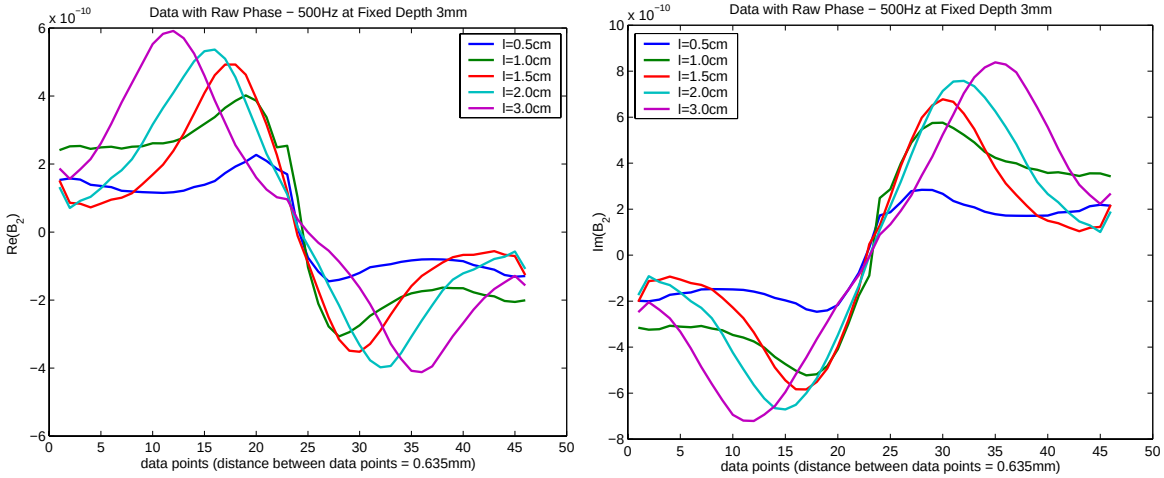

Figure 6.8: Variation in Complex Data as a Function of Length of the Damage using a Frequency of 500Hz While Keeping the Depth Fixed at $3mm$

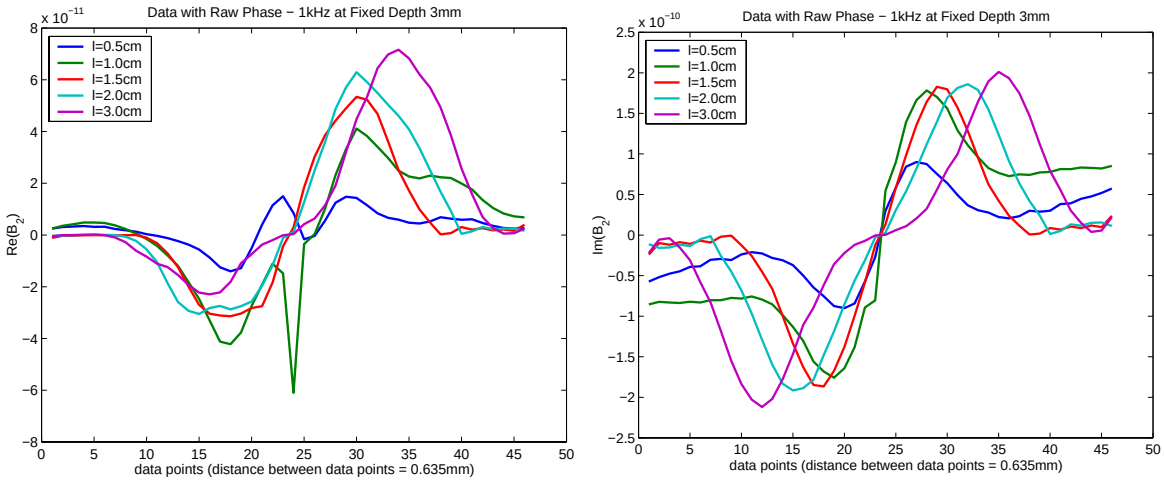

Figure 6.9: Variation in Complex Data as a Function of Length of the Damage using a Frequency of 1kHz While Keeping the Depth Fixed at $3mm$

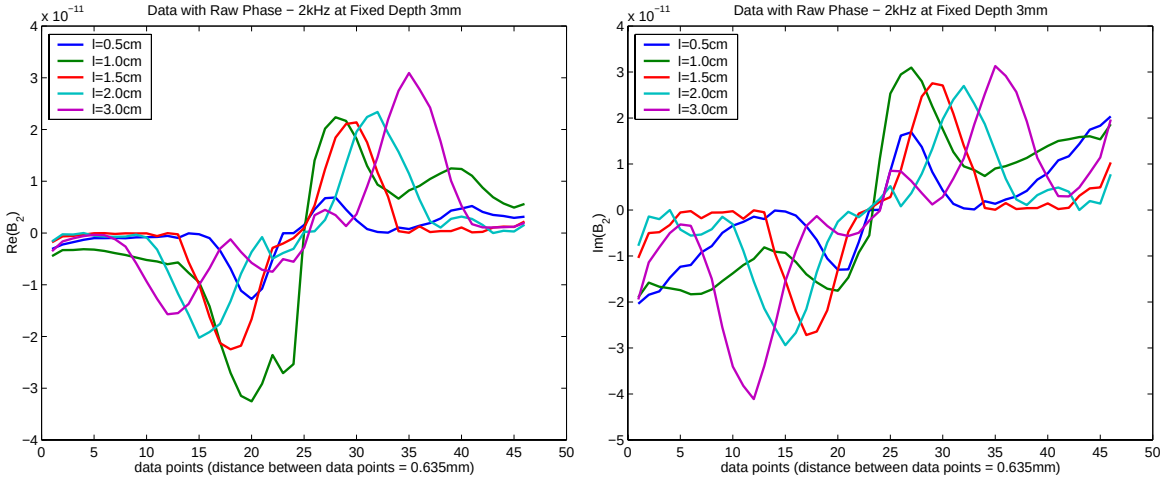

Figure 6.10: Variation in Complex Data as a Function of Length of the Damage using a Frequency of 2kHz While Keeping the Depth Fixed at $3mm$

With 1kHz, the distance between the maximum and minimum still increases as the length increases; however, the same is not true for the absolute value of the maximum and minimum. For lengths of $l = 1cm$, $l = 1.5cm$ and $l = 2cm$, the values of the maximum and minimum are approximately equal. There is only a slight variation in their values. Since the depth of penetration for 1kHz is $3.83mm$ (Table 6.1), skin depth may already be affecting the data detected by the sensor for a damage at depth

$3mm$. To test this concept, we plotted the magnetic flux density for a sample with damages at a fixed depth of $2mm$ and $1mm$, Figures 6.11 and 6.12 respectively. In each case, the real part is still random but the imaginary part now displays the same pattern as that for 250Hz and 500Hz. There is some variation in the smoothness when we consider a depth of $1mm$ but both the location and values of the maximum and minimum varying consistently with respect to length of the damage.

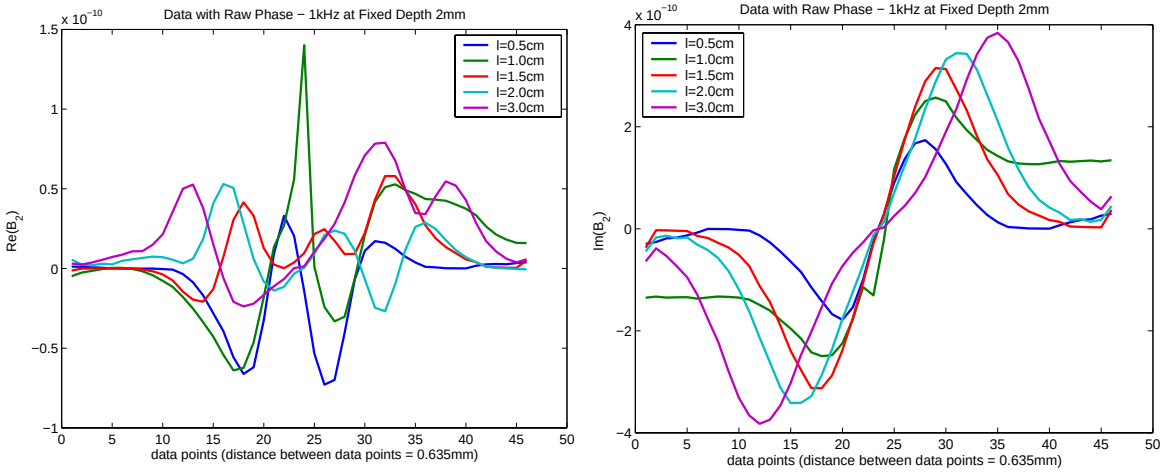

Figure 6.11: Variation in Complex Data as a Function of Length of the Damage using a Frequency of 1kHz While Keeping the Depth Fixed at $2mm$

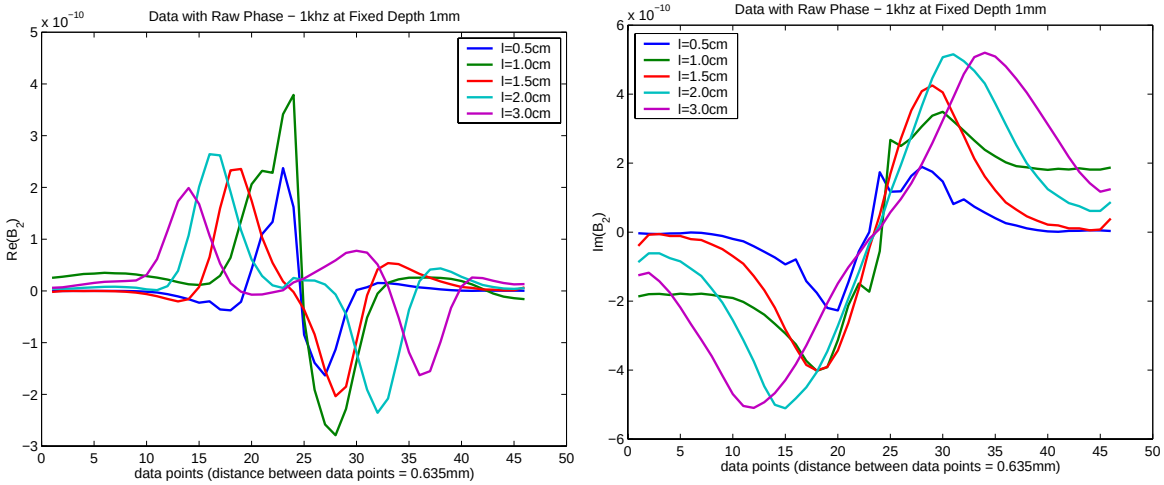

Figure 6.12: Variation in Complex Data as a Function of Length of the Damage using a Frequency of 1kHz While Keeping the Depth Fixed at $1mm$

Unlike the plots for the other frequencies, data taken at a source frequency of 2kHz (Figure 6.10) seems to be more random. There *is* some observable pattern between the location of the maximum and minimum of the imaginary portion of the data; however, the data still does not exhibit a consistent pattern even when the damage is closer to the surface, at $2mm$ (Figure 6.13) and $1mm$ (Figure 6.14). While this frequency may still be a viable frequency to use in the inverse problem, it is not clear from these plots.

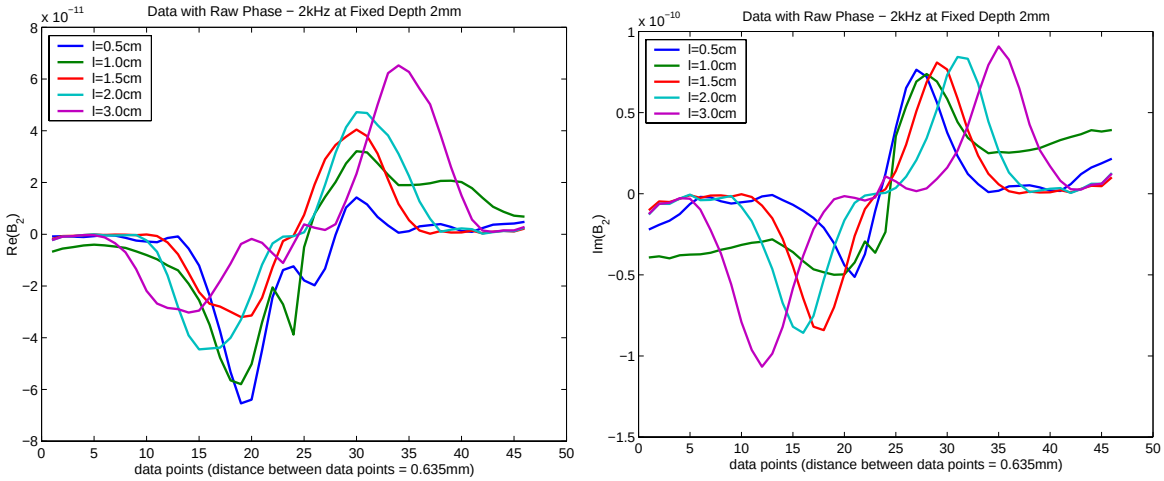

Figure 6.13: Variation in Complex Data as a Function of Length of the Damage using a Frequency of 2kHz While Keeping the Depth Fixed at $2mm$

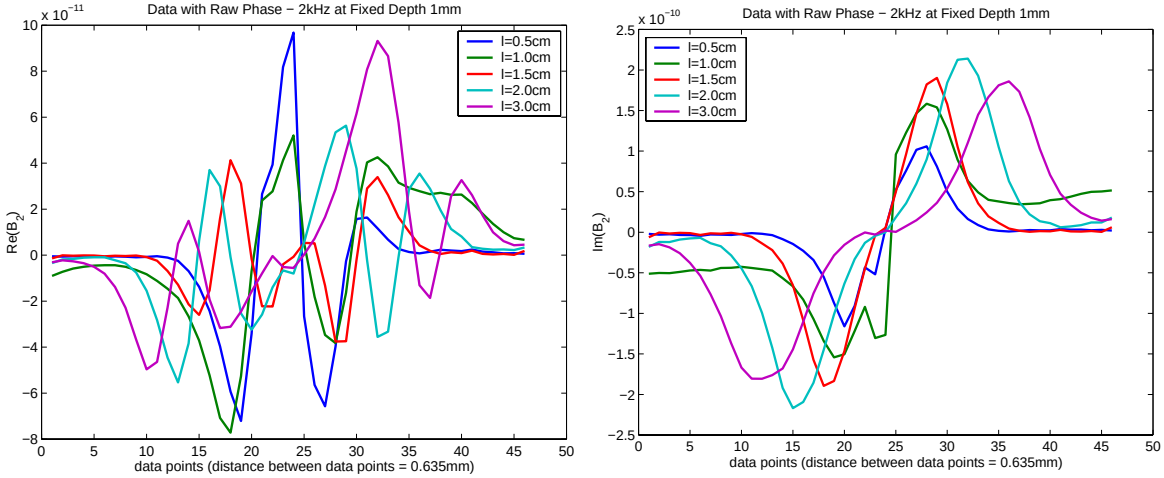

Figure 6.14: Variation in Complex Data as a Function of Length of the Damage using a Frequency of 2kHz While Keeping the Depth Fixed at $1mm$

Since we would like for the entire data to be used in the inverse problem, we explored the idea of shifting the phase to obtain a pattern in *both* the real and imaginary parts for all the frequencies.

6.2.3 Analysis of Data Using "Shifted" Phase Information

To determine the appropriate phase shift, we first examined the difference between the raw phase when using a source frequency of 500Hz and the raw phase using a source frequency of 1kHz, Figure 6.15. To understand the form of the phase, we recall the right hand rule depicted in Figure 6.16. If the current flows as depicted in the figure, the magnetic field circles around the current. In our case, the current is flowing into the paper, in the negative z direction and the magnetic field circles around the current in the xy plane. Therefore, at the ends of the sample, in an ideal setting, the phase should be 180 deg or π radians out of phase. In addition, in the middle of the sample there will be a jump in the phase when the magnetic field changes direction. These properties are depicted in Figure 6.15.

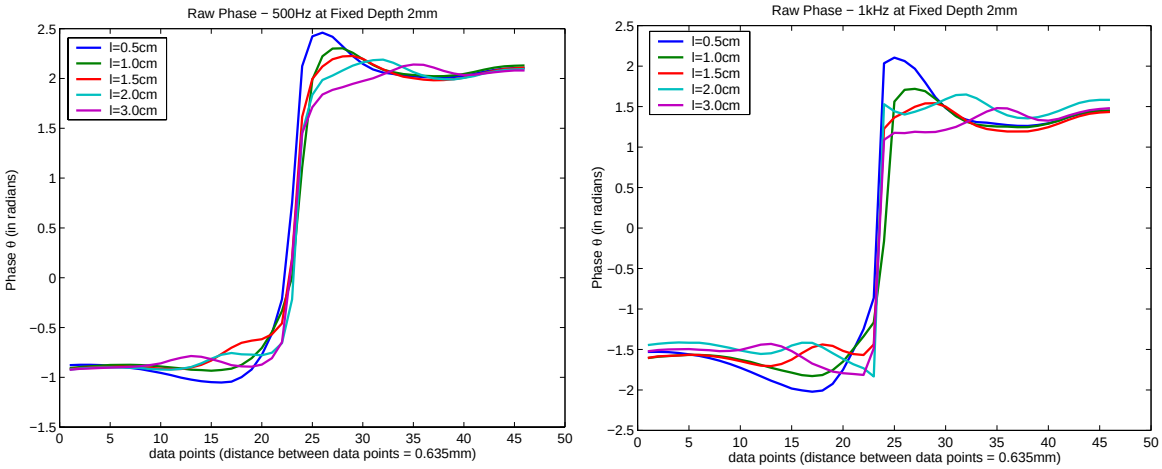

Figure 6.15: Comparison of Phase When Using a Frequency of 500Hz vs. 1kHz: The first plot shows the variation in phase as a function of length of the damage using a frequency of 500Hz while keeping the depth fixed at $2mm$. The second plot shows the variation in phase as a function of length of the damage using a frequency of 1kHz while keeping the depth fixed at $2mm$.

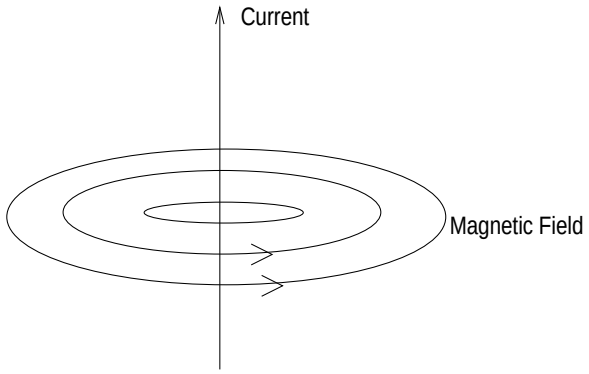

Figure 6.16: Schematic of Right Hand Rule

Examining the form of the phase more closely, if the phase to the left of the center is transversed and reflected across the line $y = \frac{1}{2}(\theta_n + \theta_1)$ (the difference between the end points), the phase to the left is approximately the phase to the right of the center. On average, the line about which the data is reflected for 500Hz is $y_{500} = 0.5942$ radians and for 1kHz, $y_{1000} = -0.0457$ radians.

From our observations, the difference in the line of reflection is the key to either having nicely patterned data for both real and imaginary components or random behavior in one of the components. Recall that the real part of the data is given by $|\hat{B}_2^j| \cos(\theta)$. Therefore, if the line of reflection is given by $y \approx 0$ (the case for 1kHz) and there is a 180 deg (or π radians) phase difference between the endpoints of the sample, for the majority of the data points x_j, $\theta_j \approx \pm\pi/2$ which implies $\cos(\theta_j) \approx 0$. This is true except in the center where $\theta \approx 0$ or $\cos(\theta) \approx 1$. However, the contribution of $\cos(\theta)$ at this point is counteracted by the amplitude which is approximately zero in the center of the damage. Consequently, the real part of the magnetic flux density would exhibit random behavior from the slight offset of θ_j from $\pi/2$. Shifting the data by exactly $\pi/2$ would only result in the interchange of the real and imaginary parts. Therefore, we want a phase shift which will give us significant information in *both* the real part and imaginary parts. In other words, we want data to exhibit the same pattern as that found when using 500Hz. When using a frequency of 500Hz, the line of reflection is approximately $\pi/6$. This was enough of an offset in the phase

to distribute the data between both the real and imaginary portion of the magnetic flux density. However, we choose to use a phase shift (for all frequencies) such that the final phase would have a line of reflection given by $y = \pi/4$. This is because, as we already noted, when the phase has a line of reflection given by $y = 0$, the data consequently exhibits random behavior in the real part. Similarly a line of reflection given by $y = \pi/2$ would result in random behavior in the imaginary portion of the data; therefore, we choose $y = \pi/4$ which is halfway between $y = 0$ and $y = \pi/2$. This evenly distributes the information. Hence, the shifted phase θ^{shift} is given by

$$\theta_j^{shift} = \theta_j - 1/2(\theta_n + \theta_1) + \pi/4. \tag{6.4}$$

Figures 6.17-6.20 give the resulting magnetic flux density for the various phases when the phase is shifted according to (6.4).

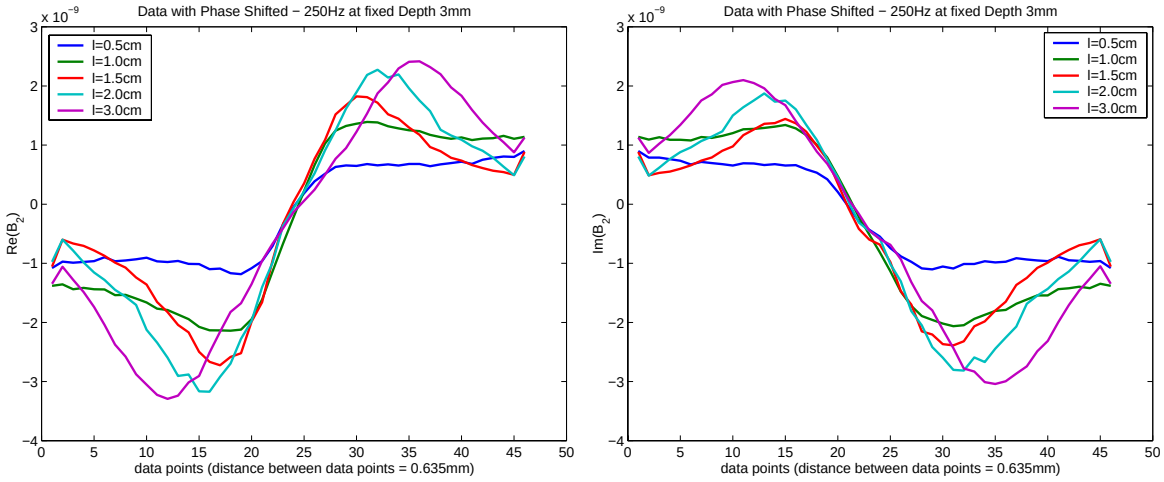

Figure 6.17: Variation in Complex Data using Shifted Phase Information as a Function of Length of the Damage using a Frequency of 250Hz While Keeping the Depth Fixed at $3mm$

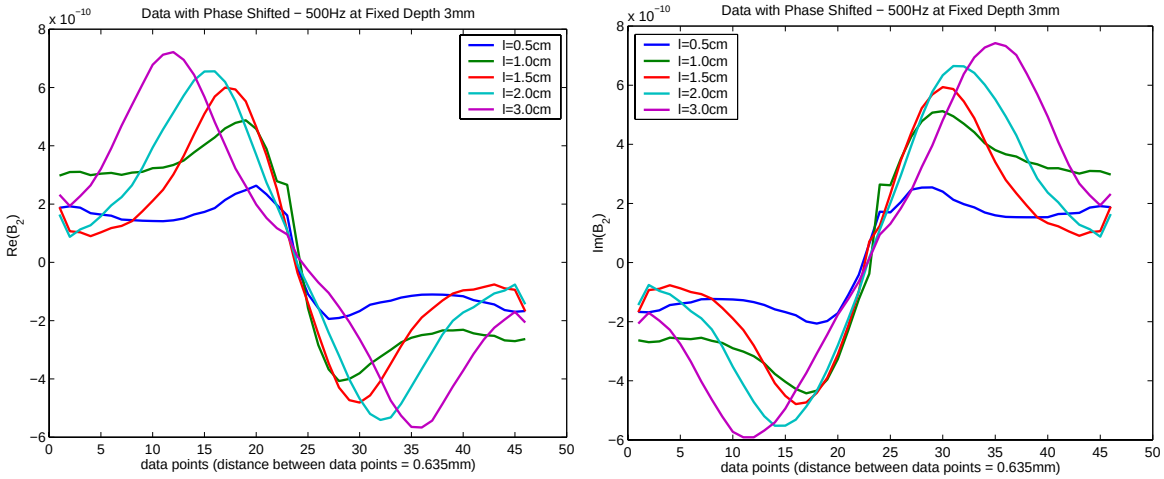

Figure 6.18: Variation in Complex Data using Shifted Phase Information as a Function of Length of the Damage using a Frequency of 500Hz While Keeping the Depth Fixed at $3mm$

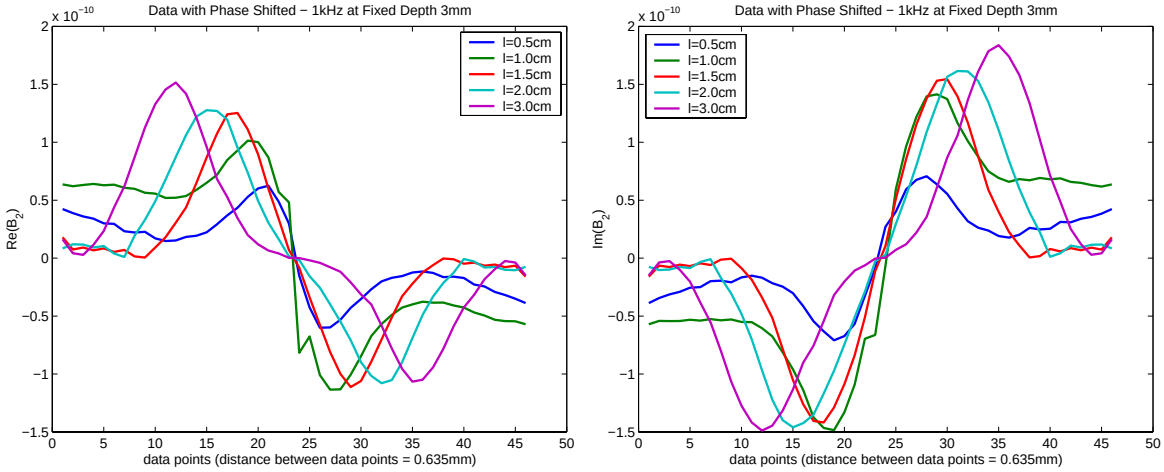

Figure 6.19: Variation in Complex Data using Shifted Phase Information as a Function of Length of the Damage using a Frequency of 1kHz While Keeping the Depth Fixed at $3mm$

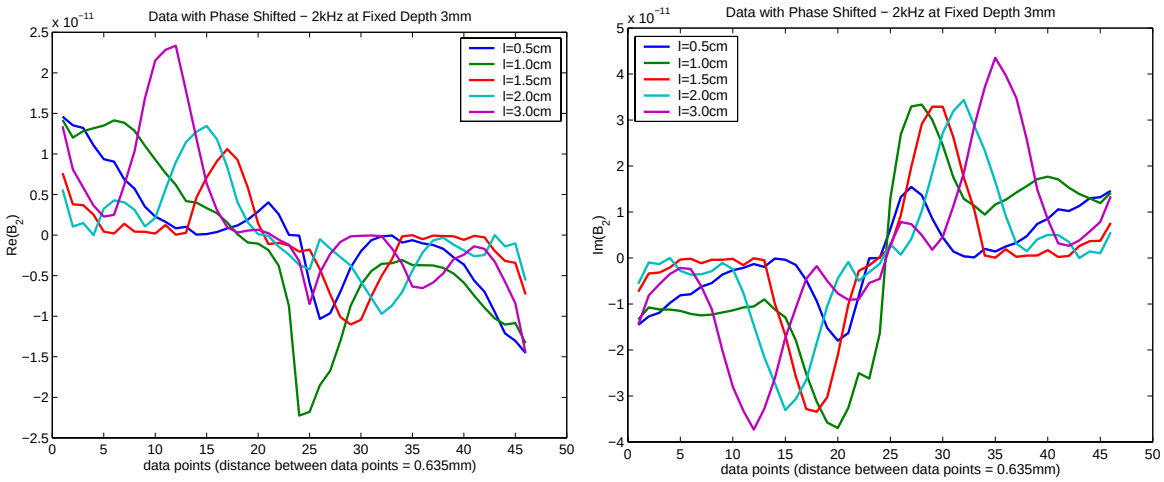

Figure 6.20: Variation in Complex Data using Shifted Phase Information as a Function of Length of the Damage using a Frequency of 2kHz While Keeping the Depth Fixed at $3mm$

In each case, except for 2kHz, both the real and imaginary parts of the data now show a discernible pattern. However, this does not assure us that results using the data with the shifted phase will be more accurate than data using the raw phase or the average phase. The next subsection discusses averaging the phase in the same manner in which we averaged the amplitude.

6.2.4 Analysis of Data Using "Averaged" Phase Information

Since we averaged the amplitude across the center of the sample, we also explored the idea of averaging the phase across the center of the damage as well. We average both the raw phase data and the shifted phase data and examine how averaging the phase effects the real and imaginary components of the magnetic flux density for the different frequencies.

We use the same technique for averaging the phase as we did when we averaged the amplitude, except we have to include the line of reflection. In other words, we reflect the data to the left of the center across the line $y = \frac{1}{2}(\theta_1 + \theta_n)$ and then average the reflected phase data to the left of the center with the phase data to the right of

the center. Thus, using raw phase data θ_j, we have average phase data given by the simplified formula

$$\theta_j^{avg} = \frac{1}{2}\left(-\theta_j + \theta_{n-j+1}\right) + \left|\frac{1}{2}(\theta_1 + \theta_n)\right|. \tag{6.5}$$

Figures 6.21-6.24 give the magnetic flux density determined using average phase information defined by (6.5).

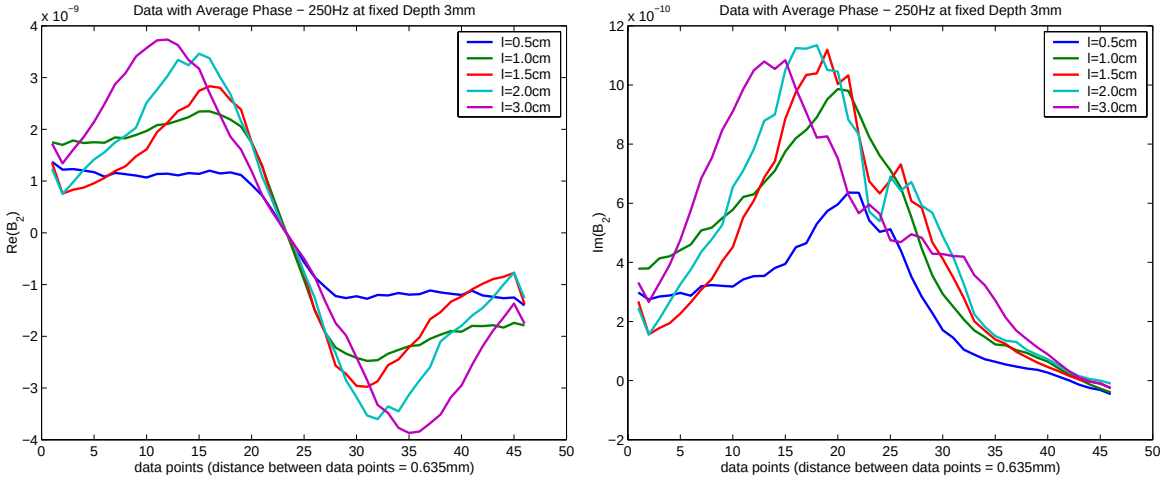

Figure 6.21: Variation in Complex Data using "Averaged" Phase Information as a Function of Length of the Damage using a Frequency of 250Hz While Keeping the Depth Fixed at $3mm$

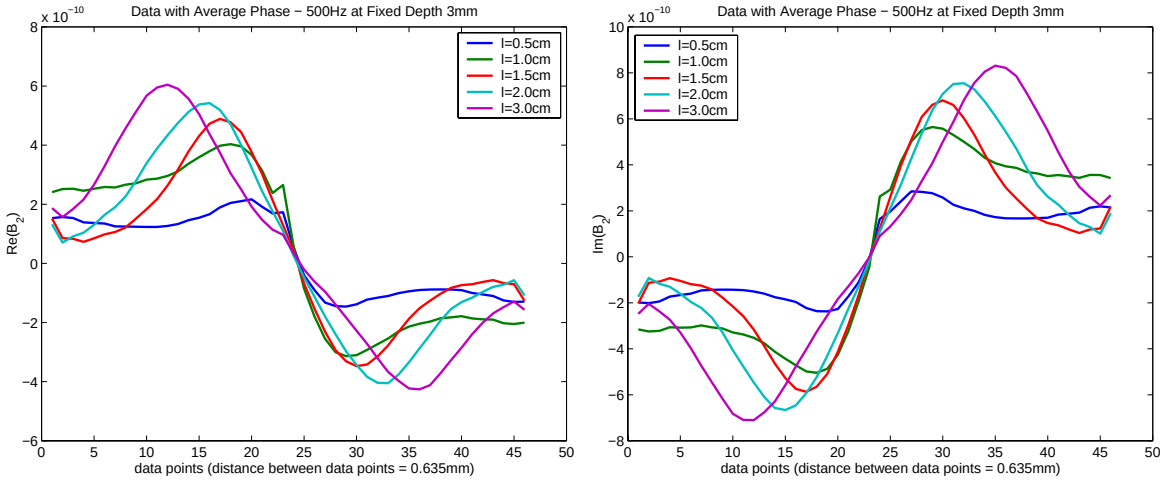

Figure 6.22: Variation in Complex Data using "Averaged" Phase Information as a Function of Length of the Damage using a Frequency of 500Hz While Keeping the Depth Fixed at $3mm$

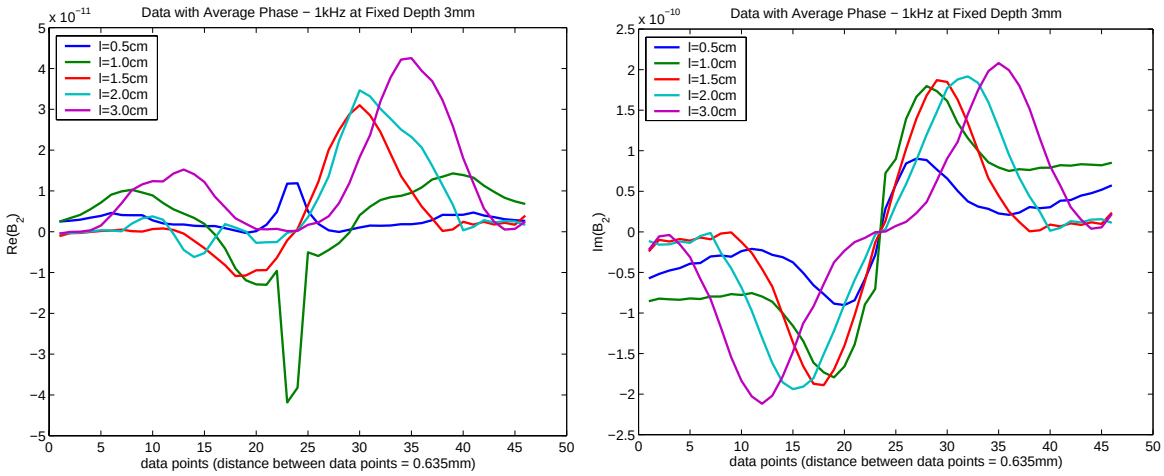

Figure 6.23: Variation in Complex Data using "Averaged" Phase Information as a Function of Length of the Damage using a Frequency of 1kHz While Keeping the Depth Fixed at $3mm$

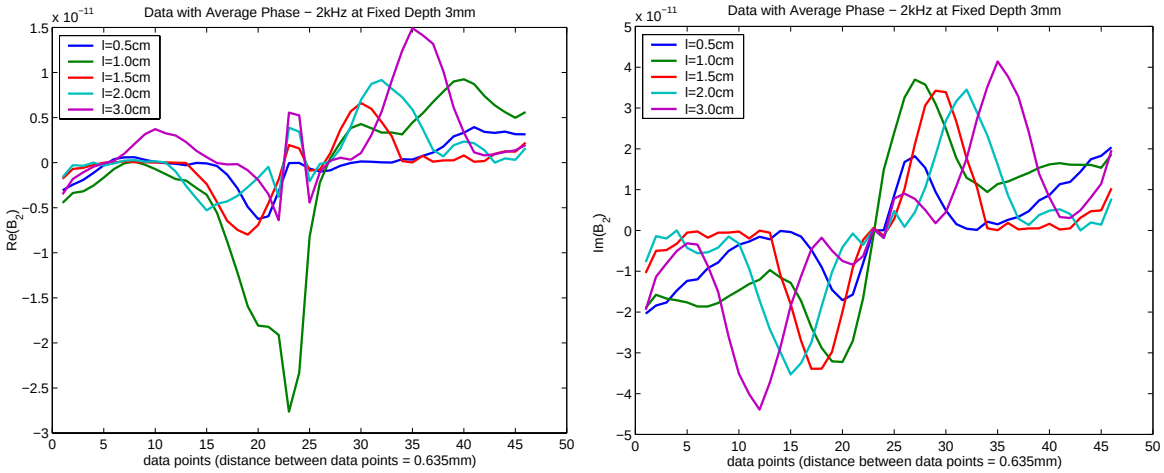

Figure 6.24: Variation in Complex Data using "Averaged" Phase Information as a Function of Length of the Damage using a Frequency of 2kHz While Keeping the Depth Fixed at $3mm$

Similarly, shifted and averaged phase data is given by

$$\theta_j^{shiftavg} = \frac{1}{2}\left(-\theta_j^{shift} + \theta_{n-j+1}^{shift}\right) + \left|\frac{1}{2}(\theta_1^{shift} + \theta_n^{shift})\right|. \tag{6.6}$$

Figures 6.25-6.28 give the calculated magnetic flux density when we use phase

information which has been both shifted by definition (6.4), and averaged by definition (6.6).

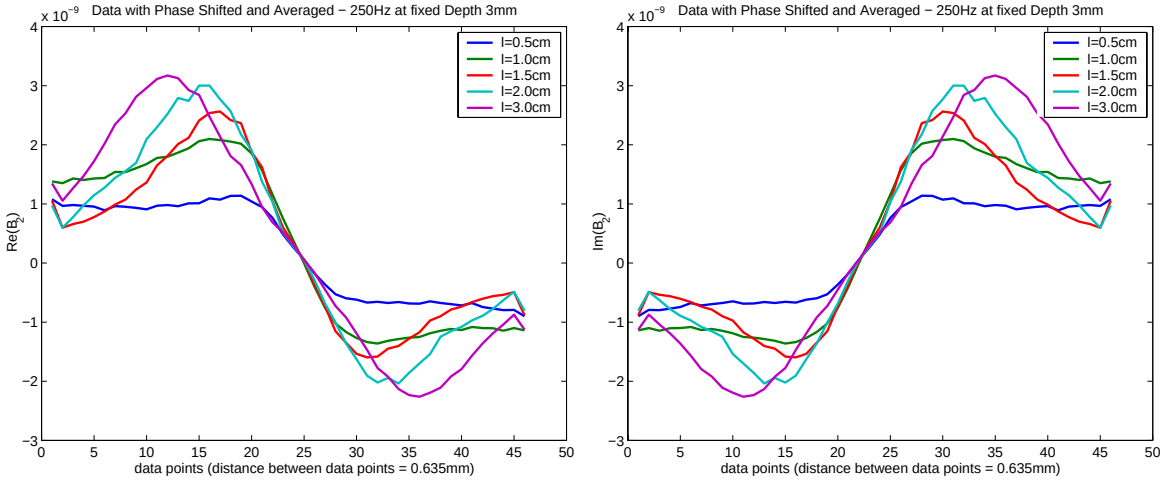

Figure 6.25: Variation in Complex Data using Shifted *and* Averaged Phase Information as a Function of Length of the Damage using a Frequency of 250Hz While Keeping the Depth Fixed at $3mm$

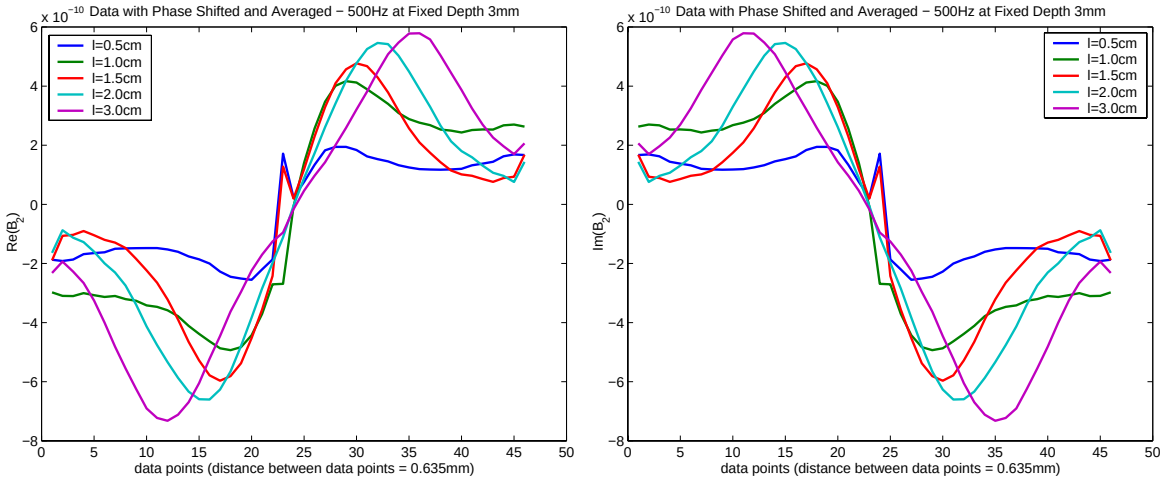

Figure 6.26: Variation in Complex Data using Shifted *and* Averaged Phase Information as a Function of Length of the Damage using a Frequency of 500Hz While Keeping the Depth Fixed at $3mm$

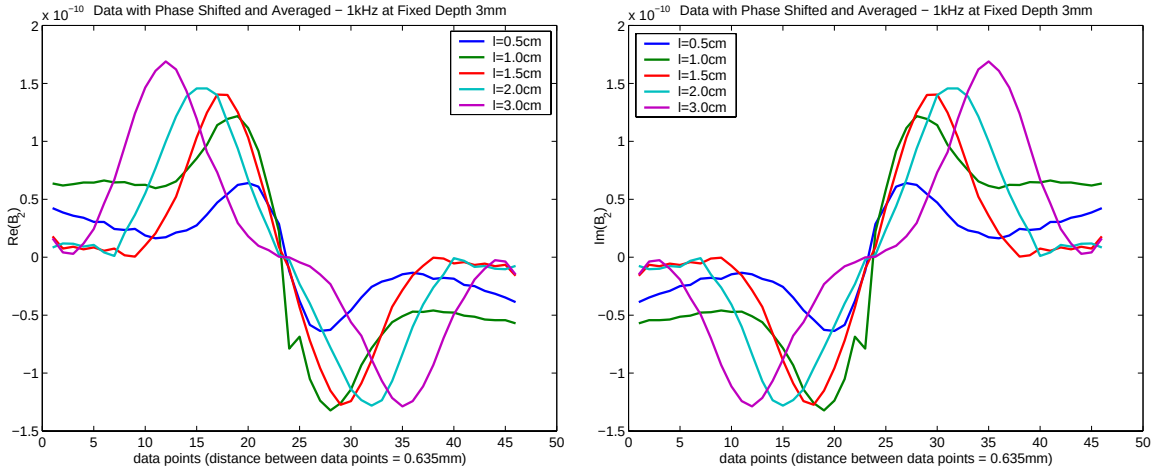

Figure 6.27: Variation in Complex Data using Shifted *and* Averaged Phase Information as a Function of Length of the Damage using a Frequency of 1kHz While Keeping the Depth Fixed at $3mm$

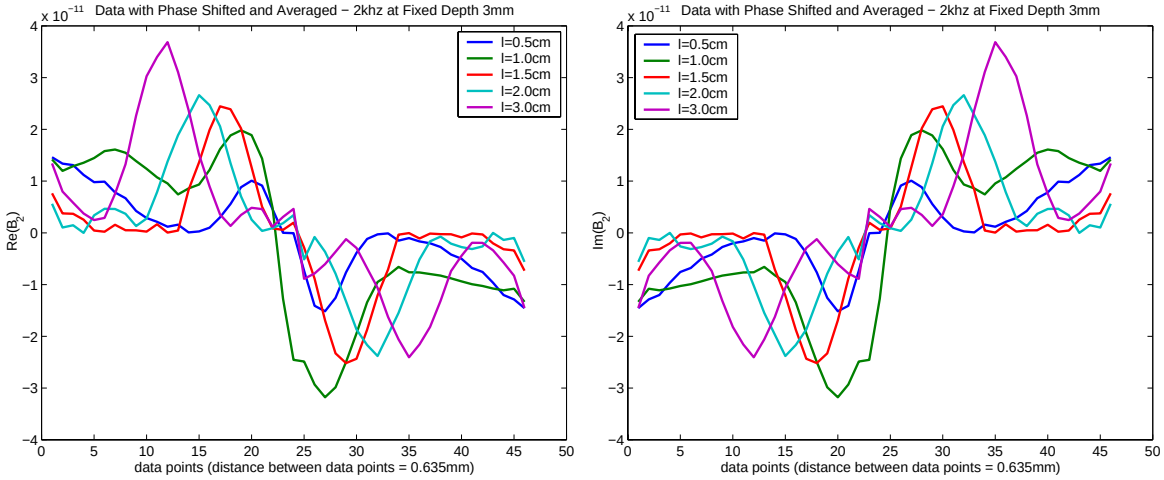

Figure 6.28: Variation in Complex Data using Shifted *and* Averaged Phase Information as a Function of Length of the Damage using a Frequency of 2kHz While Keeping the Depth Fixed at $3mm$

By only examining the plots without any other information, it appears as if averaging the phase alone produces a more consistent pattern across values of length in the magnetic flux density for frequencies 250Hz and 500Hz and 1kHz when comparing Figure 6.7 with 6.21, Figure 6.8 with 6.22, and Figure 6.9 with 6.23 respectively.

However, in all cases, even when using 2kHz, shifting and averaging the phase 'textitboth produced the most visible pattern in the data as a function of the length of the damage. In the next section we examine the POD approximations compared to the data to determine how the behavior of the data affects the ability to estimate the parameters describing the damage.

6.3 Estimating the Damage

In Section 4.2, we demonstrated two possible ways in which we could form the POD approximation of the solution, POD/Interpolation or POD/Galerkin. As discussed in Section 6.1, the model does not accurately describe the experimental design, therefore the POD/Galerkin method cannot be used. Consequently, as mentioned previously, we use the POD/Interpolation method for the results reported here. In the simulations performed in Chapter 5, the POD/Interpolation approximation used a built-in Matlab routine *interp1* or *interp2* with linear interpolation for the one parameter case and cubic spline interpolation for the two parameter case respectively. However, when using experimental data, we did not obtain accurate results with linear interpolation in either case and thus we have chosen to use cubic spline interpolation in both the one parameter and two parameter estimation problems.

6.3.1 Determining the Length of the Damage

In determining the length of the damage, we kept the depth fixed at $2mm$, $3mm$ and $4mm$ and estimated a length of either $1cm$, $1.5cm$ or $2cm$ (keeping the thickness fixed at $1mm$). When estimating a fixed length, snapshots for the POD basis elements incorporated data from samples with damages at the fixed depth with varying lengths, *excluding* the true length. In other words, in trying to estimate a length of $1cm$ at a fixed depth of $2mm$, we used data from samples with damages having lengths of $0.5cm$, $1.5cm$, $2cm$ and $3cm$ all at a depth of $2mm$ to form the snapshots. In addition, all the POD basis elements were used in the approximation since we had only 4 basis

elements. (Only a small amount of data was taken to establish proof-of-concept.)

Since 500Hz displayed the most uniform pattern across the length of the damage, we chose to try to estimate lengths $l = 1cm$, $l = 1.5cm$ and $l = 2cm$ fixed at a depth of $2mm$ using only the raw phase data (and, as always, the modified amplitude data). Using the cost criterion in (6.1) where the POD approximation $B_2^N(\mathbf{q})$ is formed using snapshots on the data modified in the exact same way as the data we wish to characterize (i.e. modified amplitude together with raw phase information - no phase shift or phase average), we obtained the results in Table 6.2.

Table 6.2: Determination of Length using (6.1) at a Depth of $2mm$ with Frequency 500Hz

Actual Length (cm)	1.0	1.5	2.0
Optimized Length (cm)	1.9000	0.7352	1.0431

Even though the data showed the pattern we would expect, we still could not estimate the length with any certainty. Therefore, we analyzed the difference between the POD approximations and the actual data for a damage at a depth of $3mm$ with a fixed length of $1.5cm$ in Figure 6.29.

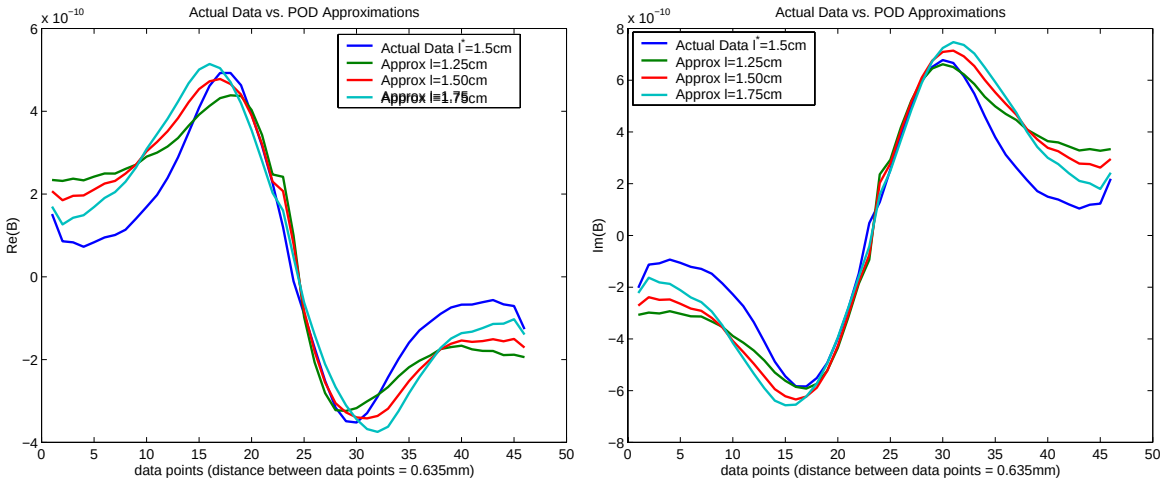

Figure 6.29: Comparison of POD Approximations for Varying Lengths to Data for a Sample Containing a Damage with Exact Length 1.5cm at a Fixed Depth of 3mm Using a Frequency of 500Hz

In Figure 6.29, we would ideally like for the POD approximation associated with length $1.5cm$ (the red curve) to match the actual data for a sample with a damage of length $1.5cm$ (the blue curve). Unfortunately none of the approximations match the actual data across the entire scan area; however, the maximum and minimum of the real part of the POD approximation associated with length $1.5cm$ matched the actual data considerably well. Therefore, it might be more appropriate (and more useful) to choose a cost criterion given by

$$\begin{aligned} J_{maxminRe}(\mathbf{q}) &= \frac{10^{24}}{2}\left|\max_{1\le j\le n} Re(B_2^N(x_j;\mathbf{q})) - \max_{1\le j\le n} Re(\hat{B}_2^j)\right|^2 \\ &\quad + \frac{10^{24}}{2}\left|\min_{1\le j\le n} Re(B_2^N(x_j;\mathbf{q})) - \min_{1\le j\le n} Re(\hat{B}_2^j)\right|^2 \end{aligned} \tag{6.7}$$

in which we only compare the maximum and minimum values of the data and POD approximation as opposed to comparing data across the entire scan area (10^{24} is a scale factor). Another option which takes into account the maximum and minimum values of the magnetic flux density but which also ignores the first and last portion of the data (that data which cannot be accurately approximated) is to compare data across the center of the sample. In other words, we can compare data between the maximum and minimum values. Let $x_{j_{maxRe}}$ and $x_{j_{minRe}}$ be the data points corresponding to maximum and minimum of the real part of the magnetic flux density respectively. Then, letting $a_{Re} = \min(j_{maxRe}, j_{minRe})$ and $b_{Re} = \max(j_{maxRe}, j_{minRe})$ the cost criterion

$$J_{midRe}(\mathbf{q}) = \frac{1}{2}\sum_{j=a_{Re}-2}^{b_{Re}+2}\left|10^9 Re(B_2^N(x_j;\mathbf{q})) - 10^9 Re(\hat{B}_2^j)\right|^2 \tag{6.8}$$

compares the difference in the real portion of the POD approximation and data across data points just to the left of the maximum or minimum and just to the right of the maximum or minimum. These are two cost criterions which seem like viable options for this particular problem; however, these cost criterions may not work for every frequency. Furthermore, modifying the phase data as discussed in the previous section may produce an even better approximation to the actual data.

Indeed, there was a noticeable improvement in the "pattern" of the data when the phase was shifted. Therefore, it may be more appropriate to use data with a phase shift and include both real and imaginary parts of the data in the cost function. In other words, instead of (6.7) and (6.8), it may be more appropriate to use

$$J^s_{maxmin} = J^s_{maxminRe} + J^s_{maxminIm} \tag{6.9}$$

and

$$J^s_{mid} = J^s_{midRe} + J^s_{midIm} \tag{6.10}$$

where $J^s_{maxminRe}$, $J^s_{maxminIm}$, J^s_{midRe} and J^s_{midIm} are defined by

$$\begin{aligned} J^s_{maxminRe}(\mathbf{q}) &= \frac{10^{24}}{2}\left|\max_{1\le j\le n} Re(B^N_{2s}(x_j;\mathbf{q})) - \max_{1\le j\le n} Re(\hat{B}^j_{2s})\right|^2 \\ &\quad + \frac{10^{24}}{2}\left|\min_{1\le j\le n} Re(B^N_{2s}(x_j;\mathbf{q})) - \min_{1\le j\le n} Re(\hat{B}^j_{2s})\right|^2, \end{aligned} \tag{6.11}$$

$$\begin{aligned} J^s_{maxminIm}(\mathbf{q}) &= \frac{10^{24}}{2}\left|\max_{1\le j\le n} Im(B^N_{2s}(x_j;\mathbf{q})) - \max_{1\le j\le n} Im(\hat{B}^j_{2s})\right|^2 \\ &\quad + \frac{10^{24}}{2}\left|\min_{1\le j\le n} Im(B^N_{2s}(x_j;\mathbf{q})) - \min_{1\le j\le n} Im(\hat{B}^j_{2s})\right|^2, \end{aligned} \tag{6.12}$$

$$J^s_{midRe}(\mathbf{q}) = \frac{1}{2}\sum_{j=a_{Re}-2}^{b_{Re}+2}\left|10^9 Re(B^N_{2s}(x_j;\mathbf{q})) - 10^9 Re(\hat{B}^j_{2s})\right|^2, \tag{6.13}$$

and

$$J^s_{midIm}(\mathbf{q}) = \frac{1}{2}\sum_{j=a_{Im}-2}^{b_{Im}+2}\left|10^9 Im(B^N_{2s}(x_j;\mathbf{q})) - 10^9 Im(\hat{B}^j_{2s})\right|^2. \tag{6.14}$$

In the above equations, B_{2s} denotes data with a phase shift (s) and $x_{j_{maxIm}}$, $x_{j_{minIm}}$ are the data points corresponding to maximum and minimum of the imaginary part of the magnetic flux density respectively with $a_{Im} = \min(j_{maxIm}, j_{minIm})$ and $b_{Im} = \max(j_{maxIm}, j_{minIm})$. However, even though there was a pattern in both the real and imaginary parts of the data when it was modified with a phase shift, the results were not as accurate as when we only use the portion of the data which originally showed

a pattern (except for $f_s = 1kHz$). For the interested reader, the results using (6.9) and (6.10) can be found in Appendix C.

In the next section we give the results of the estimation problem using a portion of the data, i.e., using either (6.11) and (6.13) or (6.12) and (6.14) depending on source frequency f_s (except for $f_s = 1$kHz). We further give graphical comparisons of the POD approximations for various lengths and magnetic flux density data using raw phase information, shifted phase information, averaged phase information and shifted and averaged phase information (the modifications discussed in Section 6.2) for a sample containing a damage with length $1.5cm$ at a fixed depth of $3mm$. The graphical representations show us that using only the real or imaginary part of the data with a phase shift is indeed the best choice for most of the frequencies considered.

Determination of Length Using 250Hz

In the previous section, Figure 6.7 showed a consistent pattern across the length of the damage in only the real part of the data; therefore, it seems feasible to use either the cost criterion given by (6.11) or (6.13). Using the optimization routine *nelder* with cost criterion (6.11), we obtained the results in Table 6.3. The results in Table 6.4 are associated with cost criterion (6.13). As discussed previously, when a frequency is used which has a deeper depth of penetration, there may be a loss in sensitivity to the damage. This could be a reason for the inaccuracies of the estimates (except for fixed depth of $3mm$). In this case, the most accurate estimates were obtained when considering only the maximum and minimum values.

Figures 6.30 - 6.33 give the comparison between the POD approximation and the actual data using a source frequency of 250Hz with raw phase information (Figure 6.30), shifted phase information (Figure 6.31), averaged phase information (Figure 6.32), and shifted and averaged phase information (Figure 6.33). The figures show that indeed the POD approximation matches the data best in the real portion of the data when the data has been modified with a phase shift.

Table 6.3: Determination of Length at a Frequency of 250Hz Using (6.11) when Modifications of Experimental Data include Averaging Magnitude, Filtering Out Background Noise, and Shifting Phase Data

Depth(mm)	Actual Length(cm)	Optimized Length(cm)	Relative Error
2	1.0	1.5068	50.68%
	1.5	2.5713	71.42%
	2.0	1.3143	34.28%
3	1.0	0.9254	7.46%
	1.5	1.3869	7.54%
	2.0	1.9845	0.78%
4	1.0	2.2422	124.22%
	1.5	1.7255	15.04%
	2.0	2.7649	38.24%

Table 6.4: Determination of Length at a Frequency of 250Hz Using (6.13) when Modifications of Experimental Data include Averaging Magnitude, Filtering Out Background Noise, and Shifting Phase Data

Depth(mm)	Actual Length(cm)	Optimized Length(cm)	Relative Error
2	1.0	-	-
	1.5	1.0618	29.21%
	2.0	1.2498	37.51%
3	1.0	1.0902	9.02%
	1.5	1.3866	7.56%
	2.0	1.6712	16.44%
4	1.0	0.8249	17.51%
	1.5	1.6610	10.73%
	2.0	1.2398	38.01%

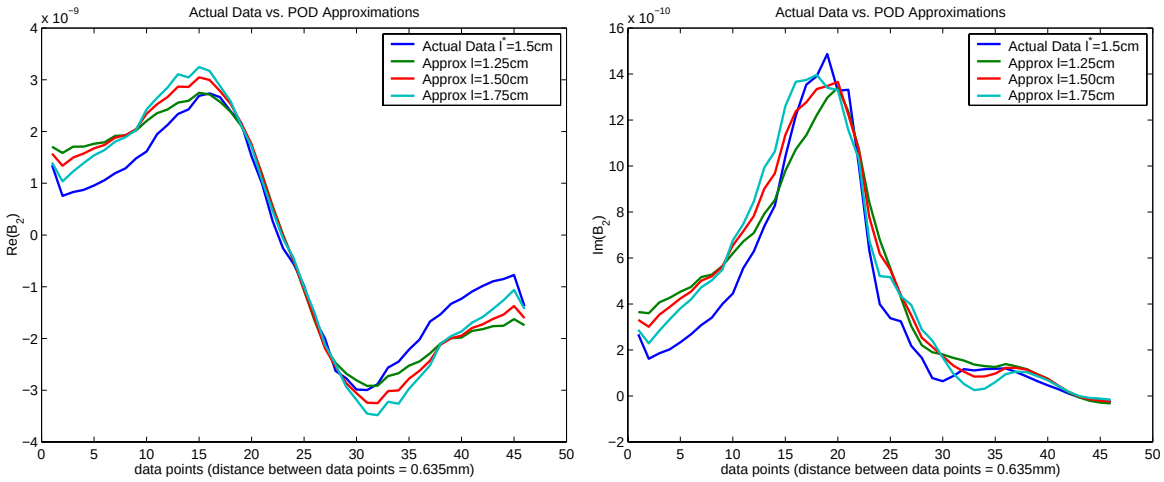

Figure 6.30: Comparison of POD Approximations for Varying Lengths to Data for a Sample Containing a Damage with Exact Length 1.5cm at a Fixed Depth of 3mm Using Raw Phase Information at a Frequency of 250Hz

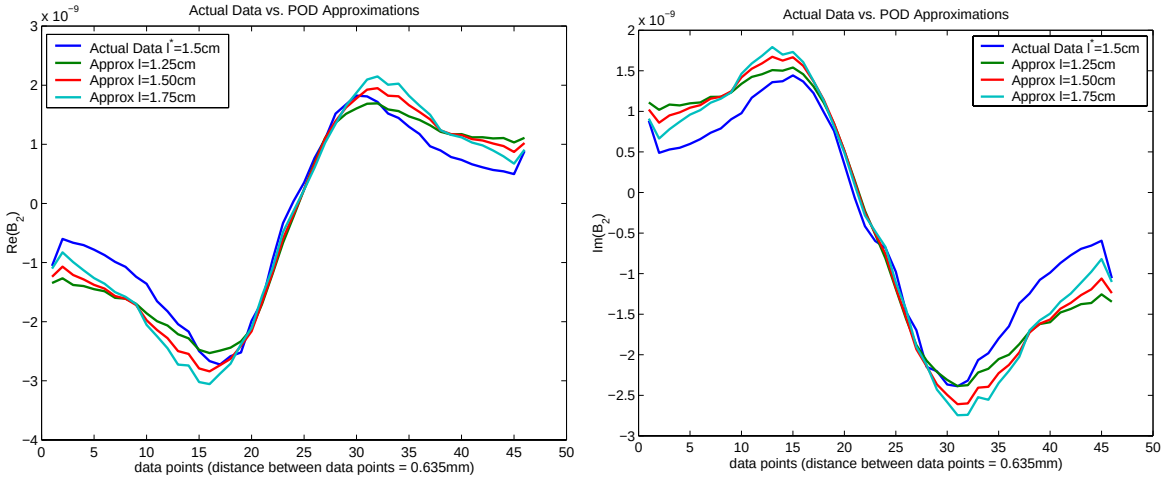

Figure 6.31: Comparison of POD Approximations for Varying Lengths to Data for a Sample Containing a Damage with Exact Length 1.5cm at a Fixed Depth of 3mm Using Shifted Phase Information at a Frequency of 250Hz

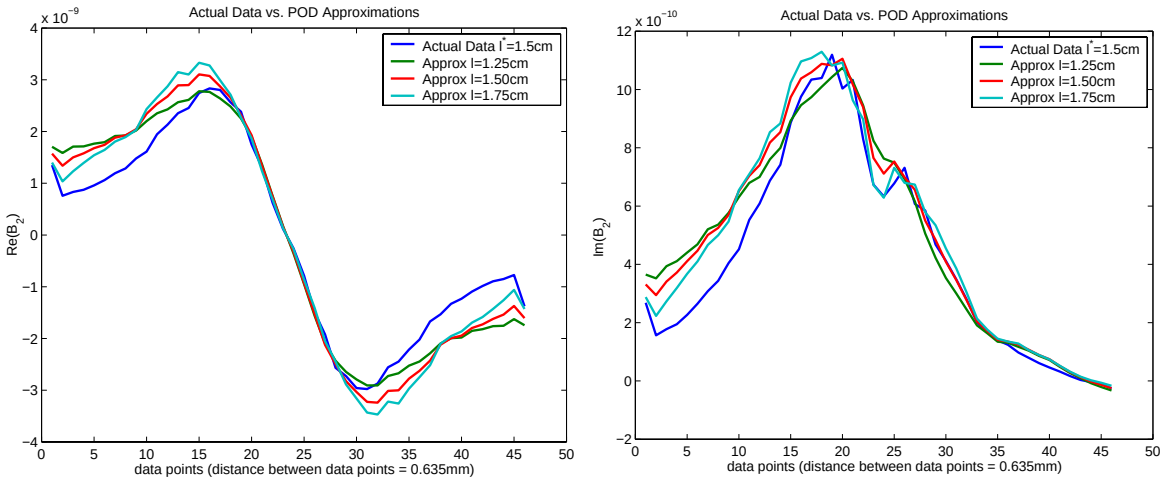

Figure 6.32: Comparison of POD Approximations for Varying Lengths to Data for a Sample Containing a Damage with Exact Length 1.5cm at a Fixed Depth of 3mm Using "Averaged" Phase Information at a Frequency of 250Hz

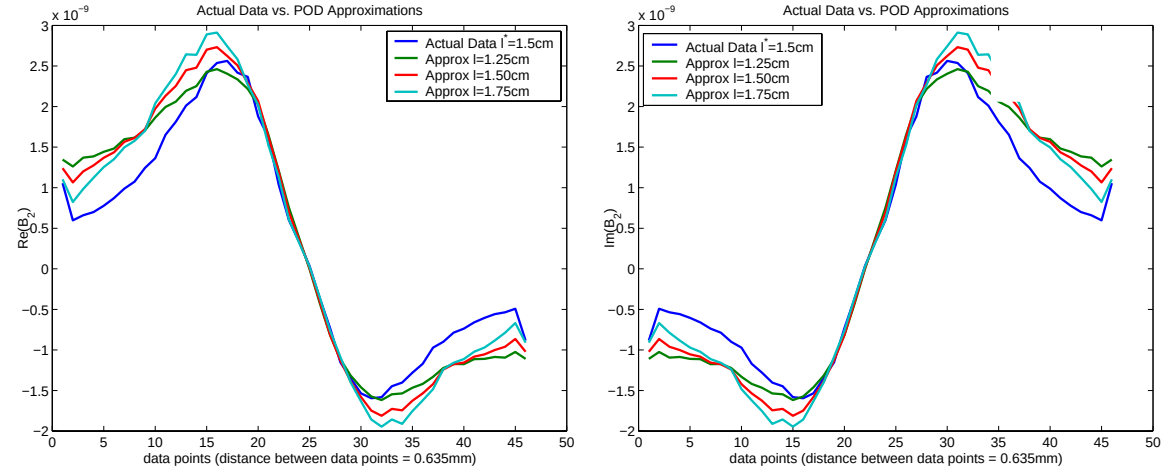

Figure 6.33: Comparison of POD Approximations for Varying Lengths to Data for a Sample Containing a Damage with Exact Length 1.5cm at a Fixed Depth of 3mm Using Shifted *and* Averaged Phase Information at a Frequency of 250Hz

Determination of Length Using 500Hz

With $500Hz$, both portions of the data showed a consistent pattern to the data as a function of the length of the damage. However, in initial trials (Appendix C), the best results again came from using the real part of the data. Using either cost criterion

(6.11) and (6.13) in the inverse problem with the optimization routine *nelder*, we obtained the results in Tables 6.5 and 6.6, respectively. We note that there is a significant improvement in the estimate. In most cases (with only a few exceptions) the relative error is below 10%. We can further conclude that the average relative error across the 9 estimations is 8.99% when using (6.11) and 8.97% when (6.13) is used. In either case, we obtain good parameter estimations.

Table 6.5: Determination of Length at a Frequency of 500Hz Using (6.11) when Modifications of Experimental Data include Averaging Magnitude, Filtering Out Background Noise, and Shifting Phase Data

Depth(mm)	Actual Length(cm)	Optimized Length(cm)	Relative Error
2	1.0	0.8002	19.98%
	1.5	1.6036	6.91%
	2.0	1.7319	13.40%
3	1.0	0.9225	7.75%
	1.5	1.5540	3.60%
	2.0	1.9259	3.70%
4	1.0	0.9202	7.98%
	1.5	1.7137	14.25%
	2.0	2.0676	3.38%

Table 6.6: Determination of Length at a Frequency of 500Hz using (6.13) when Modifications of Experimental Data include Averaging Magnitude, Filtering Out Background Noise, and Shifting Phase Data

Depth(mm)	Actual Length(cm)	Optimized Length(cm)	Relative Error
2	1.0	0.9397	6.03%
	1.5	1.6145	7.63%
	2.0	2.8560	42.80%
3	1.0	0.9428	5.72%
	1.5	1.4885	0.77%
	2.0	1.7553	12.23%
4	1.0	0.9807	1.93%
	1.5	1.5334	2.23%
	2.0	2.0275	1.37%

Figures 6.34 - 6.37 give the comparison between the POD approximation and the actual data using a source frequency of 500Hz with raw phase information (Figure 6.34), shifted phase information (Figure 6.35), averaged phase information (Figure 6.36), and shifted and averaged phase information (Figure 6.37). The figures graphically show that using a phase shift resulted in the best approximation.

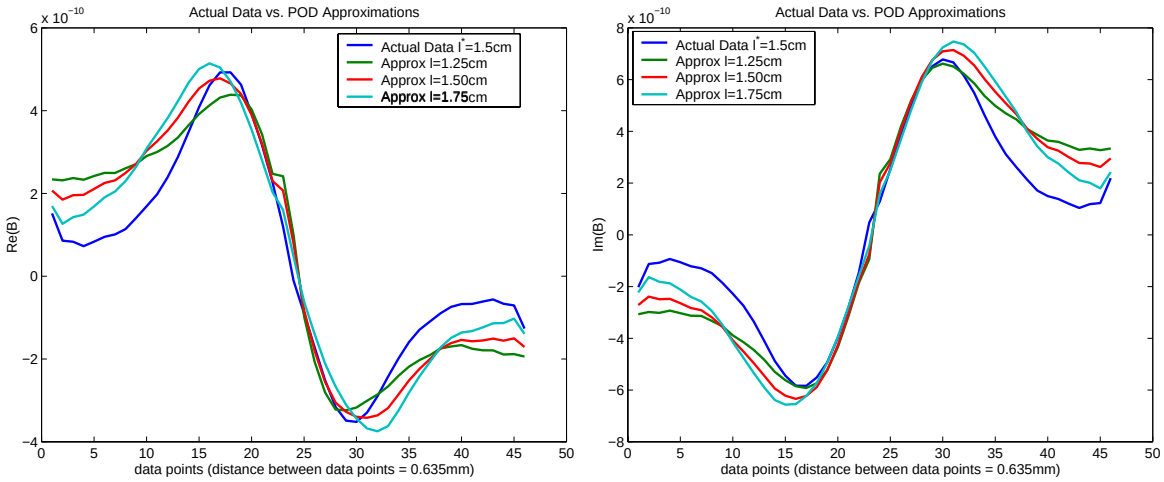

Figure 6.34: Comparison of POD Approximations for Varying Lengths to Data for a Sample Containing a Damage with Exact Length 1.5cm at a Fixed Depth of 3mm Using Raw Phase Information at a Frequency of 500Hz

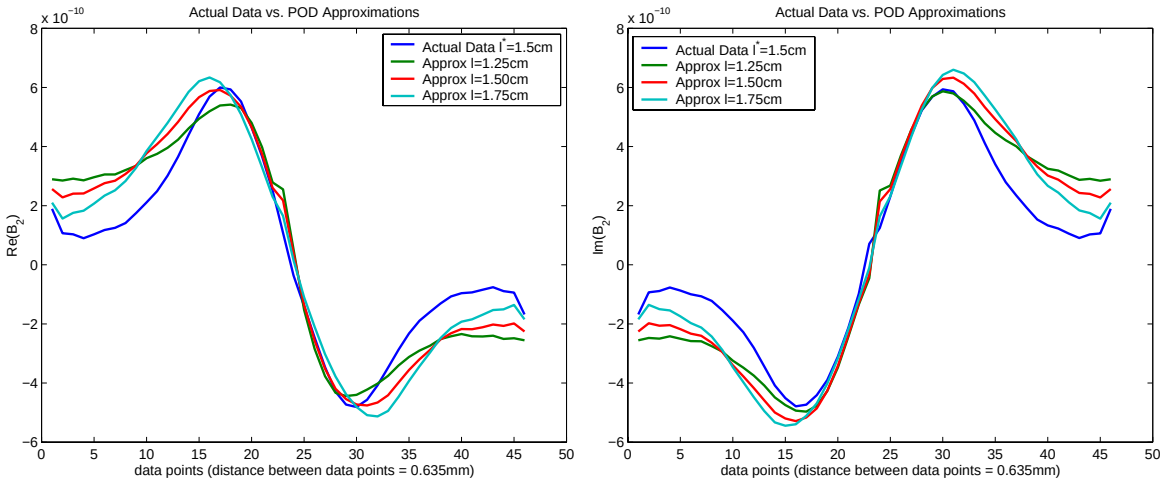

Figure 6.35: Comparison of POD Approximations for Varying Lengths to Data for a Sample Containing a Damage with Exact Length 1.5cm at a Fixed Depth of 3mm Using Shifted Phase Information at a Frequency of 500Hz

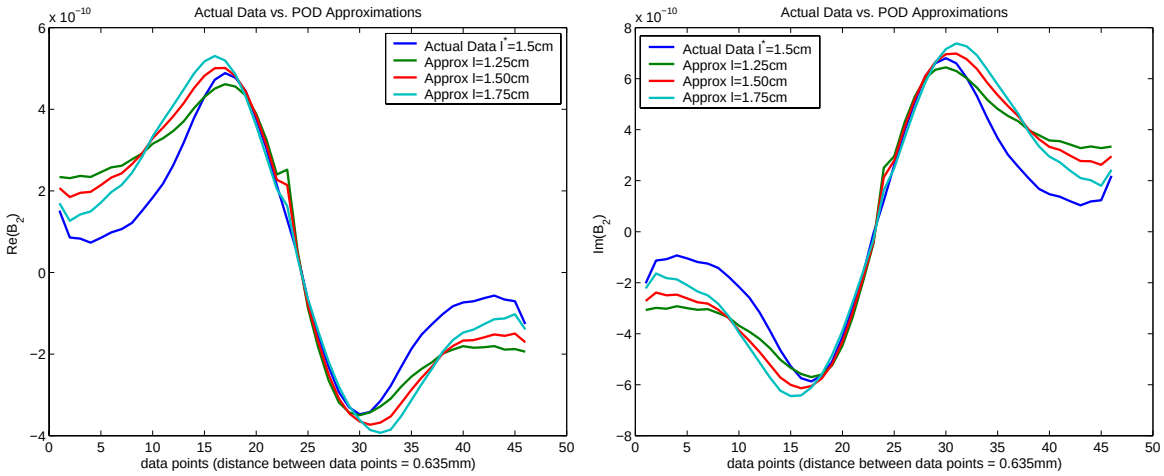

Figure 6.36: Comparison of POD Approximations for Varying Lengths to Data for a Sample Containing a Damage with Exact Length 1.5cm at a Fixed Depth of 3mm Using "Averaged" Phase Information at a Frequency of 500Hz

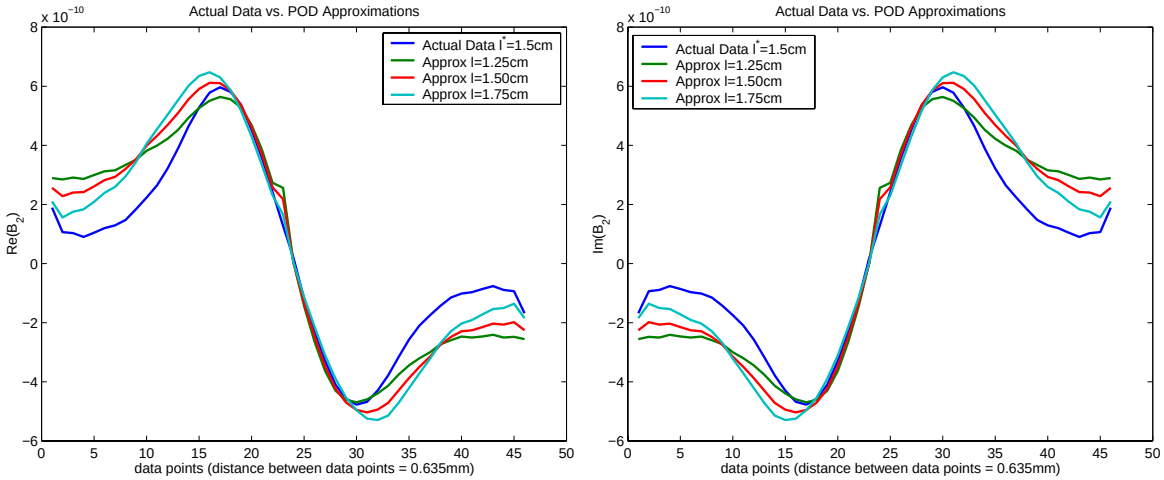

Figure 6.37: Comparison of POD Approximations for Varying Lengths to Data for a Sample Containing a Damage with Exact Length 1.5cm at a Fixed Depth of 3mm Using Shifted *and* Averaged Phase Information at a Frequency of 500Hz

Determination of Length Using 1kHz

The data corresponding to source frequency 1kHz does not follow the same pattern as that for the previous two frequencies considered. In this case, we could not obtain good estimates when using shifted phase data (results in Appendix C); therefore the

results reported below use raw phase data (no shift or average of the phase) for the imaginary part of the data (Figure 6.9 shows only a pattern in the imaginary portion). Thus, the cost criterion is given by either

$$\begin{aligned} J_{maxminIm}(\mathbf{q}) &= \frac{10^{24}}{2}\left|\max_{1\le j\le n} Im(B_2^N(x_j;\mathbf{q})) - \max_{1\le j\le n} Im(\hat{B}_2^j)\right|^2 \\ &\quad + \frac{10^{24}}{2}\left|\min_{1\le j\le n} Im(B_2^N(x_j;\mathbf{q})) - \min_{1\le j\le n} Im(\hat{B}_2^j)\right|^2 \end{aligned} \tag{6.15}$$

or

$$J_{midIm}(\mathbf{q}) = \frac{1}{2}\sum_{j=a_{Im}-2}^{b_{Im}+2}\left|10^9 Im(B_2^N(x_j;\mathbf{q})) - 10^9 Im(\hat{B}_2^j)\right|^2. \tag{6.16}$$

Table 6.7 gives the results for estimating length using the cost criterion defined by (6.15). The results in Table 6.8 lists those obtained using cost criterion (6.16). We note that in certain instances, the optimization routine "stagnates" (i.e., the number of new simplexes created exceeds the maximum number allowed - see Chapter 4) when using (6.15). This is probably due to the fact that we are only comparing data at two points. Furthermore, the data using $f_s = 1$kHz at a depth of $3mm$ only exhibits a consistent pattern in the *location* of the maximum and minimum as opposed to the *value* of the maximum and minimum (Figure 6.9). Therefore, to include the location of the peaks into the cost criterion, it is better to use (6.16). When we use (6.16) in the optimization algorithm, we obtain an average relative error of 10.91% for the nine lengths estimated. We note that it is difficult to obtain an accurate estimate for a length of $2cm$ at any depth. Furthermore, since a depth of $4mm$ is below the depth of penetration for 1kHz ($3.83mm$), the estimates should not be as accurate at this depth.

Figures 6.38-6.41 compares the POD approximations with the actual magnetic flux density data for a damage $2mm$ deep with length $1.5cm$ (since the data did not show a significant pattern at a depth of $3mm$ in the previous section). In this case, consistent with the results, the best match is found between the imaginary part of the POD and actual data when using only the raw phase information. None of the other cases considered even came close to giving a good approximation.

Table 6.7: Determination of Length at a Frequency of 1kHz using (6.15) when Modifications of Experimental Data include only Averaging Magnitude and Filtering Out Background Noise, i.e Using Raw Phase Data

Depth(mm)	Actual Length(cm)	Optimized Length(cm)	Relative Error
2	1.0	0.8169	18.31%
	1.5	1.4789	1.41%
	2.0	1.8391	8.05%
3	1.0	-	-
	1.5	-	-
	2.0	1.3915	30.43%
4	1.0	1.8282	82.82%
	1.5	1.7765	18.43%
	2.0	1.7949	10.26%

Table 6.8: Determination of Length at a Frequency of 1kHz using (6.16) when Modifications of Experimental Data include only Averaging Magnitude and Filtering Out Background Noise, i.e Using Raw Phase Data

Depth(mm)	Actual Length(cm)	Optimized Length(cm)	Relative Error
2	1.0	1.0012	0.12%
	1.5	1.5109	0.73%
	2.0	2.7692	38.46%
3	1.0	1.0090	0.90%
	1.5	1.6320	8.80%
	2.0	1.6589	17.06%
4	1.0	1.0910	9.10%
	1.5	1.6613	10.76%
	2.0	1.7541	12.29%

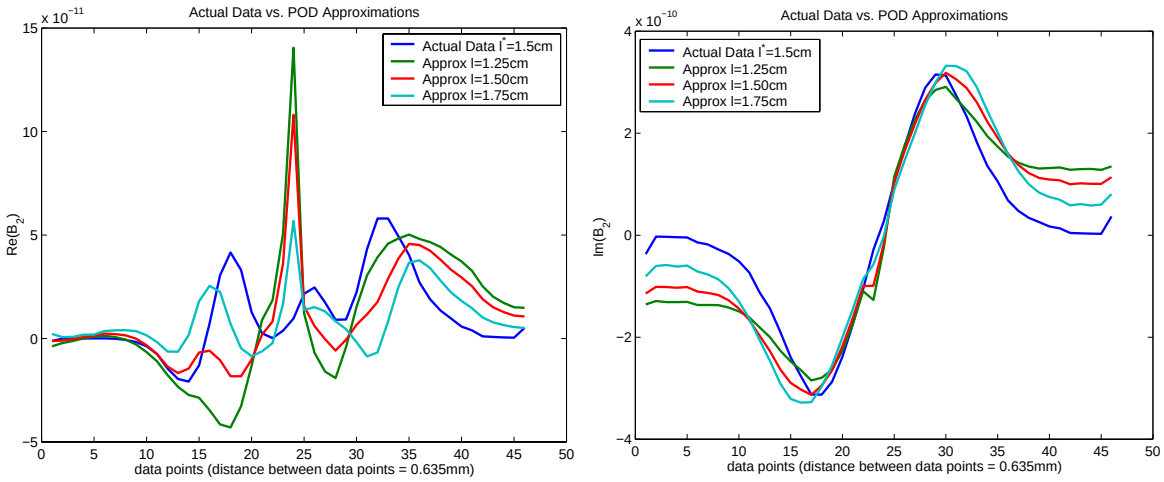

Figure 6.38: Comparison of POD Approximations for Varying Lengths to Data for a Sample Containing a Damage with Exact Length 1.5cm at a Fixed Depth of 2mm Using Raw Phase Information at a Frequency of 1kHz

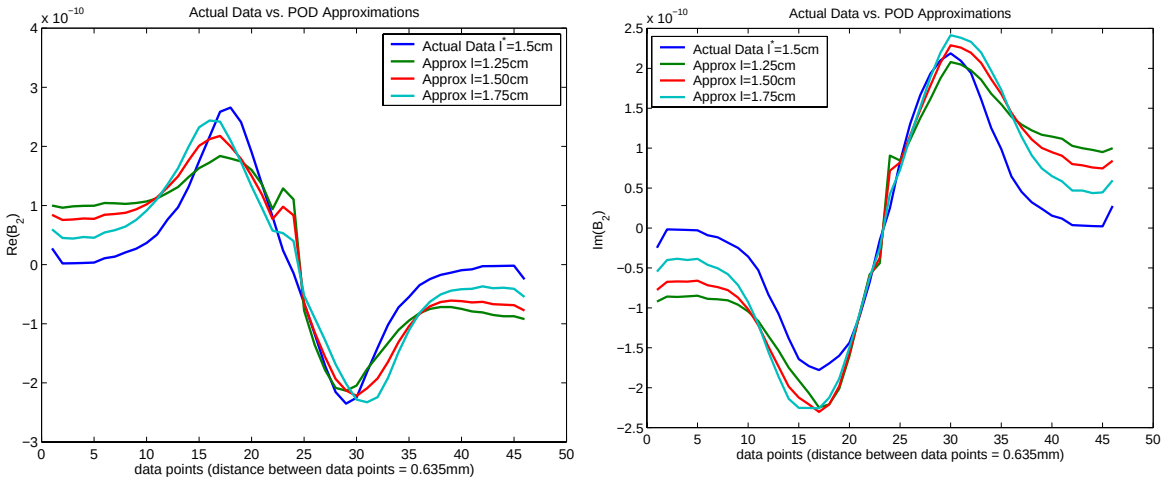

Figure 6.39: Comparison of POD Approximations for Varying Lengths to Data for a Sample Containing a Damage with Exact Length 1.5cm at a Fixed Depth of 2mm Using Shifted Phase Information at a Frequency of 1kHz

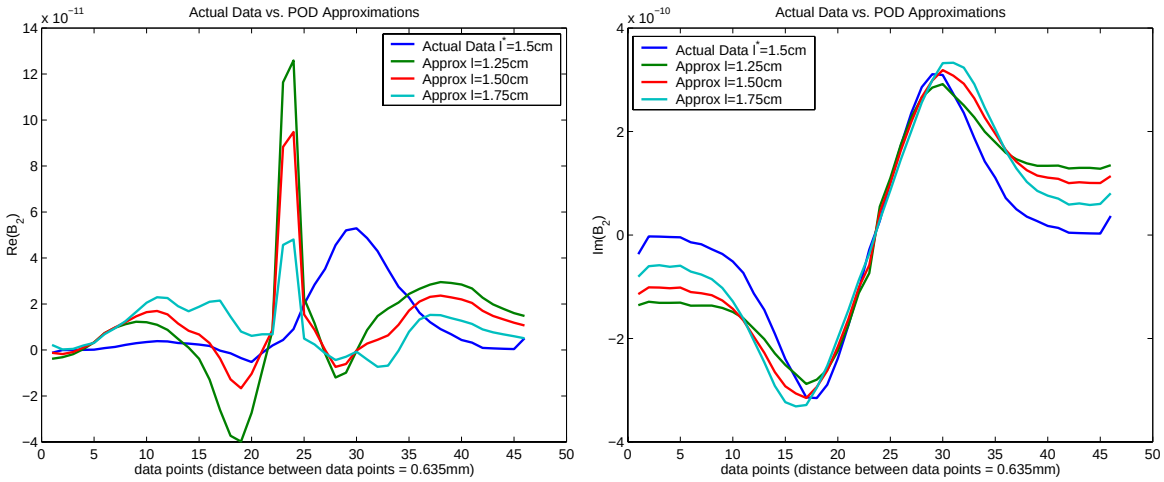

Figure 6.40: Comparison of POD Approximations for Varying Lengths to Data for a Sample Containing a Damage with Exact Length 1.5cm at a Fixed Depth of 2mm Using "Averaged" Phase Information at a Frequency of 1kHz

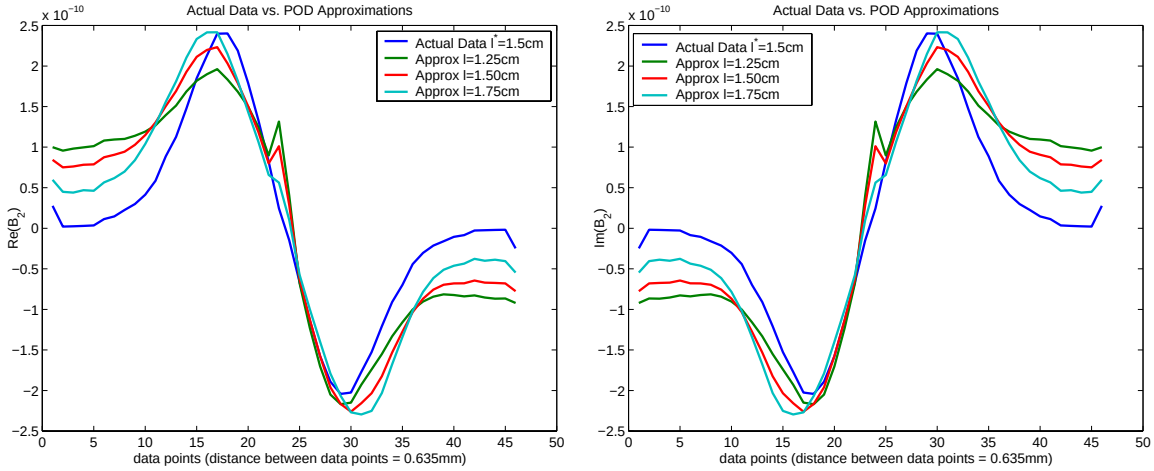

Figure 6.41: Comparison of POD Approximations for Varying Lengths to Data for a Sample Containing a Damage with Exact Length 1.5cm at a Fixed Depth of 2mm Using Shifted *and* Averaged Phase Information at a Frequency of 1kHz

Determination of Length Using 2kHz

Using a source frequency of 2kHz we use data with a phase shift as we did with 250Hz and 500Hz but compare the imaginary parts in this case since this was the part with the most consistent pattern (Figure 6.10). Thus, we use the cost criterion given by (6.12) and (6.14) and obtain the results in Tables 6.9 and 6.10, respectively. It is clear from the results that this frequency is not an appropriate choice when trying to estimate the length of a damage. We only get accurate results when trying to estimate shallow damages which are shorter in length using (6.14).

Table 6.9: Determination of Length at a Frequency of 2kHz using (6.12) when Modifications of Experimental Data include Averaging Magnitude, Filtering Out Background Noise, and Shifting Phase Data

Depth(mm)	Actual Length(cm)	Optimized Length(cm)	Relative Error
2	1.0	0.7566	24.34%
	1.5	2.7050	80.34 %
	2.0	1.4493	27.54 %
3	1.0	1.3782	37.82%
	1.5	1.3100	12.67 %
	2.0	1.6539	17.31 %
4	1.0	2.8246	182.46%
	1.5	2.0202	34.68%
	2.0	0.9327	53.36%

Table 6.10: Determination of Length at a Frequency of 2kHz using (6.14) when Modifications of Experimental Data include Averaging Magnitude, Filtering Out Background Noise, and Shifting Phase Data

Depth(mm)	Actual Length(cm)	Optimized Length(cm)	Relative Error
2	1.0	1.0441	4.41%
	1.5	1.6164	7.76 %
	2.0	1.5197	24.01 %
3	1.0	0.8586	14.14 %
	1.5	1.6926	12.84 %
	2.0	2.9426	47.13 %
4	1.0	1.7062	70.63%
	1.5	2.8723	91.48%
	2.0	1.1984	40.08%

Figures 6.42-6.45 compares the POD approximations with the actual magnetic flux density data for a damage $2mm$ deep with length $1.5cm$. None of the figures indicate that *any* modification of the data would result in a more accurate approximation.

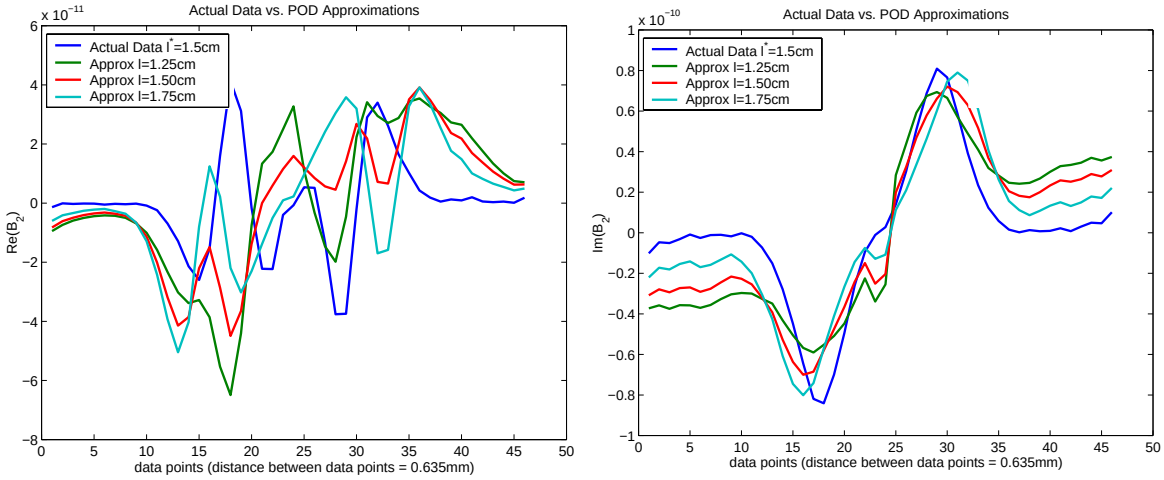

Figure 6.42: Comparison of POD Approximations for Varying Lengths to Data for a Sample Containing a Damage with Exact Length 1.5cm at a Fixed Depth of 2mm Using Raw Phase Information at a Frequency of 2kHz

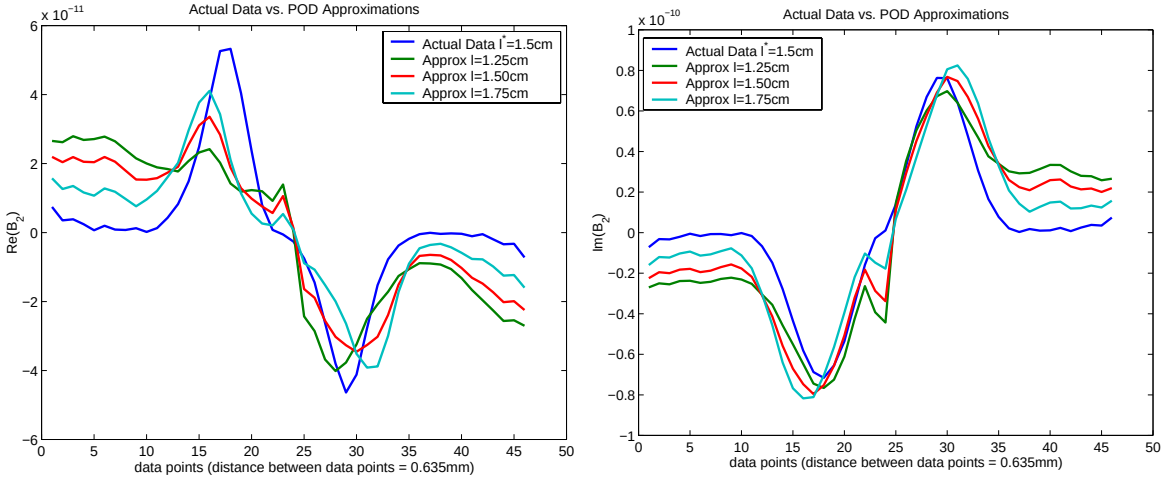

Figure 6.43: Comparison of POD Approximations for Varying Lengths to Data for a Sample Containing a Damage with Exact Length 1.5cm at a Fixed Depth of 2mm Using Shifted Phase Information at a Frequency of 2kHz

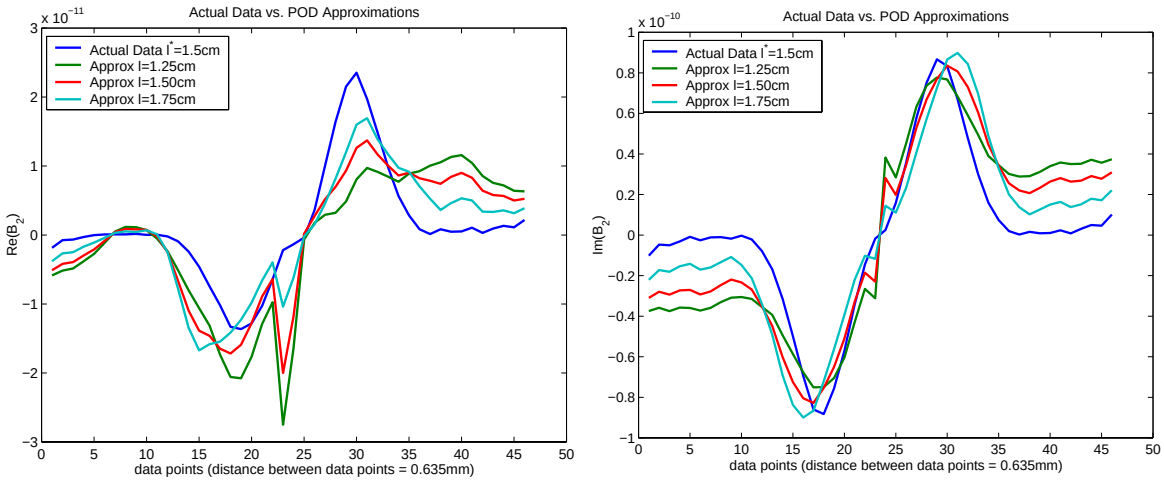

Figure 6.44: Comparison of POD Approximations for Varying Lengths to Data for a Sample Containing a Damage with Exact Length 1.5cm at a Fixed Depth of 2mm Using "Averaged" Phase Information at a Frequency of 2kHz

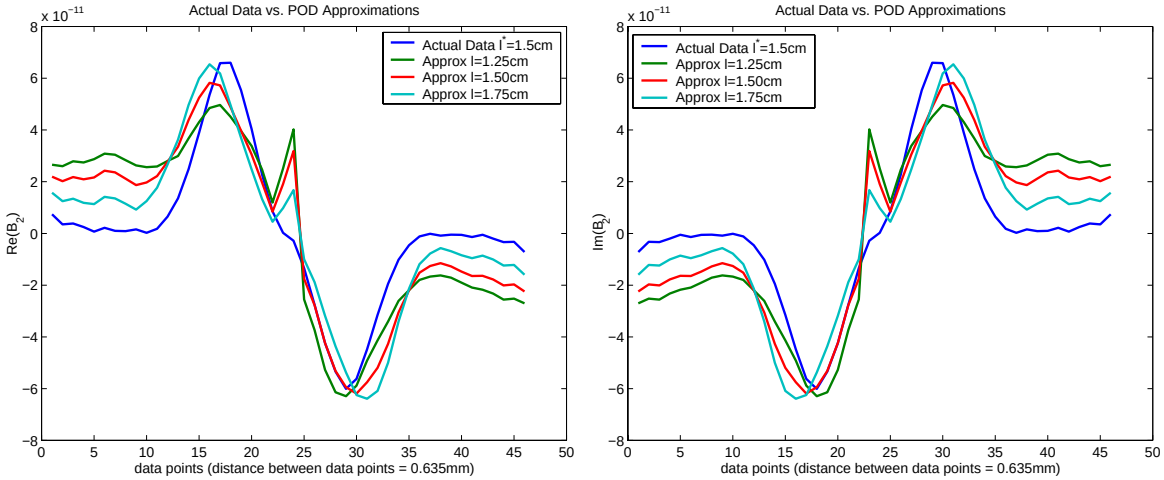

Figure 6.45: Comparison of POD Approximations for Varying Lengths to Data for a Sample Containing a Damage with Exact Length 1.5cm at a Fixed Depth of 2mm Using Shifted *and* Averaged Phase Information at a Frequency of 2kHz

6.3.2 Determining the Depth of the Damage

In determining the depth of the damage, we analyzed the results obtained when detecting the same depth using various frequencies at different fixed lengths. For

consistency, we used the cost criterions given above to estimate the depth of the damage. Comparing data across the center of the damage proved to be more robust and accurate in most cases when estimating length; hence, we only use these cost criterions for depth. In other words, we use cost criterion (6.13) for both 250Hz and 500Hz, (6.16) for 1kHz, and (6.14) for 2kHz.

In forming the snapshots, we did the same as with length where our snapshots were given by magnetic flux density data (modified in the same way the data is modified for the cost criterion) for samples with damages with the chosen fixed length (and fixed thickness of $1mm$) at all the depths ($1mm$, $2mm$, $3mm$, $4mm$, $6mm$, and $8mm$) *excluding* the depth we wish to estimate. Tables 6.11, 6.12, and 6.13 give the results for estimating various depths at different frequencies for fixed length values of $1cm$, $1.5cm$ and $2cm$ respectively.

Table 6.11: Determination of Depth with Fixed Length $1.0cm$,

Actual Depth(mm)	Frequency(Hz)	Optimized Depth(mm)	Relative Error
2	250	0.9411	52.95%
	500	2.1919	9.59%
	1000	2.1191	5.96 %
	2000	2.0479	2.39 %
3	250	3.4827	16.09%
	500	2.8047	6.51 %
	1000	2.9004	3.32 %
	2000	2.9127	0.91 %
4	250	3.4139	14.65%
	500	4.1277	3.19%
	1000	4.1865	4.66 %
	2000	5.0469	26.17%

Table 6.12: Determination of Depth with Fixed Length $1.5cm$

Actual Depth(mm)	Frequency(Hz)	Optimized Depth(mm)	Relative Error
2	250	1.5721	21.40%
	500	1.8979	5.10 %
	1000	1.8330	9.35 %
	2000	1.6484	17.58%
3	250	-	-
	500	3.1094	3.15%
	1000	3.1274	4.25%
	2000	3.2070	6.90%
4	250	2.3450	41.38 %
	500	3.8813	2.97 %
	1000	3.8691	3.27 %
	2000	6.2344	55.86%

Table 6.13: Determination of Depth with Fixed Length $2.0cm$

Actual Depth(mm)	Frequency(Hz)	Optimized Depth(mm)	Relative Error
2	250	2.0391	1.95%
	500	2.0630	3.15 %
	1000	1.9077	4.61%
	2000	1.7520	12.40%
3	250	2.9634	1.22%
	500	2.9429	1.90%
	1000	3.0625	2.08%
	2000	3.1982	6.61 %
4	250	3.8349	4.13 %
	500	4.0571	1.43 %
	1000	3.8213	4.47 %
	2000	2.9062	27.34 %

In all cases, using data obtained with source frequencies of either 500Hz or 1kHz gave quite accurate results with relative error less than 10% in each case. Between these two frequencies, there is no one best choice. Using data obtained with a source frequency of 2kHz, we achieved accurate estimates for depths $2mm$ and $3mm$ but not $4mm$. Again, as discussed previously, this is most likely due to skin effect.

The interesting case is when a frequency of 250Hz is used in obtaining the data. In this case, the estimates for depth are poor when the damage has length of either $1cm$ or $1.5cm$. However, using this frequency produces just as accurate results as those obtained with 500Hz and 1kHz when the damage has a fixed length of $2cm$. This seems to indicate that 250Hz would only be a viable frequency to use if we had some *a priori* knowledge that the damage was "long" enough. Of course, more testing must be done before making any definite conclusions. Overall, however, our trials indicate that estimating depth alone is quite feasible using the POD method.

6.3.3 Determining the Length *and* Depth of the Damage

In our final trials, we estimate both length and depth simultaneously. In order to implement the interpolation routine for our POD approximation of the magnetic flux density, we need to have a grid upon which we know the values of our coefficients for our POD approximations. Therefore, in forming our snapshots for a specific estimation, we *exclude all the data with either the same depth or length* as that we are attempting to estimate. For example, if we are estimating a length of $l^* = 1.5cm$ and a depth of $d^* = 2mm$, our snapshots consist of data for samples with damages having lengths $0.5cm$, $1cm$, $2cm$ and $3cm$ at depths $1mm$, $3mm$, $4mm$, $6mm$ and $8mm$ (all with fixed thickness of $1mm$).

Since 500Hz and 1kHz were the most consistent frequencies when estimating length and depth separately, we use these frequencies in the following trials. As before, we use cost criterions (6.13) and (6.16) for 500Hz and 1kHz respectively.

We estimated damages having a variety of combinations of depths $d^* = 2mm$, $d^* = 3mm$ and $d^* = 4mm$ and lengths $l^* = 1cm$, $l^* = 1.5cm$ and $l^* = 2cm$. The results are given in Tables 6.14 and 6.16 for 500Hz and 1kHz respectively. The associated relative errors are in Tables 6.15 and 6.17.

Table 6.14: Determination of Depth *and* Length Simultaneously with Frequency 500Hz

		Actual Length l		
		1cm	1.5cm	2cm
Actual Depth d	2mm	$l = 1.0635$ $d = 2.3097$	$l = 1.8080$ $d = 1.8403$	$l = 1.5568$ $d = 1.9946$
	3mm	$l = 0.9065$ $d = 2.9522$	$l = 1.4612$ $d = 2.9759$	$l = 2.8565$ $d = 2.5408$
	4mm	$l = 1.2421$ $d = 4.2047$	$l = 1.5849$ $d = 3.9282$	$l = 1.6908$ $d = 3.9983$

Table 6.15: Relative Error when Determining Depth (R_d) *and* Length (R_l) Simultaneously with Frequency 500Hz

		Actual Length l		
		1cm	1.5cm	2cm
Actual Depth d	2mm	$R_l = 6.35\%$ $R_d = 15.48\%$	$R_l = 20.53\%$ $R_d = 7.99\%$	$R_l = 22.16\%$ $R_d = 0.27\%$
	3mm	$R_l = 9.35\%$ $R_d = 1.59\%$	$R_l = 2.59\%$ $R_d = 0.80\%$	$R_l = 42.83\%$ $R_d = 15.31\%$
	4mm	$R_l = 24.21\%$ $R_d = 5.12\%$	$R_l = 5.66\%$ $R_d = 1.79\%$	$R_l = 15.46\%$ $R_d = 0.12\%$

Table 6.16: Determination of Depth *and* Length Simultaneously with Frequency 1kHz

		Actual Length l		
		1cm	1.5cm	2cm
Actual Depth d	2mm	$l = 1.1870$ $d = 2.2236$	$l = 1.6601$ $d = 1.8332$	$l = 1.5868$ $d = 1.8287$
	3mm	$l = 0.6632$ $d = 2.4911$	$l = 1.6439$ $d = 3.0283$	$l = 2.8304$ $d = 2.6181$
	4mm	$l = 0.6986$ $d = 3.5027$	$l = 1.7244$ $d = 3.8334$	$l = 1.6129$ $d = 4.0428$

Table 6.17: Relative Error when Determining Depth (R_d) *and* Length (R_l) Simultaneously with Frequency 1kHz

		Actual Length l		
		1cm	1.5cm	2cm
Actual Depth d	2mm	$R_l = 18.70\%$ $R_d = 11.18\%$	$R_l = 10.67\%$ $R_d = 8.34\%$	$R_l = 20.66\%$ $R_d = 8.56\%$
	3mm	$R_l = 33.68\%$ $R_d = 16.96\%$	$R_l = 9.59\%$ $R_d = 0.94\%$	$R_l = 41.52\%$ $R_d = 12.73\%$
	4mm	$R_l = 30.14\%$ $R_d = 12.43\%$	$R_l = 14.96\%$ $R_d = 4.16\%$	$R_l = 19.36\%$ $R_d = 1.07\%$

From Tables 6.14, 6.15, 6.16, and 6.17, we make a few observations. The results indicate that when estimating both length and depth simultaneously, estimating length becomes more difficult whether using 500Hz or 1kHz. It is not clear why this happens.

When using 1kHz, the only combination we could estimate accurately was $l^* = 1.5cm$ and $d^* = 2mm$, $d^* = 3mm$ or $d^* = 4mm$. In all other cases, the estimates were not accurate. This was not in line with the previous results when we were able to estimate both length and depth separately using 1kHz. It would be necessary to analyze the data more thoroughly to discern a reason for the failure in this case.

However, using 500Hz we obtained extremely accurate estimates for *both* length and depth when we were trying to estimate a depth of $d^* = 2mm$ and length $l^* = 1cm$, $d^* = 3mm$ and lengths $l^* = 1cm$ and $l^* = 1.5cm$ or $d^* = 4mm$ and lengths $l^* = 1.5cm$ or $l^* = 2cm$. Using a frequency of 500Hz typically failed when trying to estimate a length of $l^* = 2cm$ with any depth. This is consistent with the previous results when trying to estimate a length of $2cm$ alone. Nonetheless, we can conclude that although there were cases in which estimating depth and length simultaneously failed, this method is still a viable approach with a source frequency of 500Hz.

6.4 Conclusions

In this chapter, we have successfully demonstrated that the POD method can be used in an inverse problem methodology with experimental data. However, if we wish to

use simulations to form our snapshots, we have to provide a more realistic model of the physical setting. Even so, if "good" data is available, i.e., data which exhibits a discernible pattern, this data can be used as snapshots in forming the POD basis elements, freeing us from needing to accurately model the experimental design.

When comparing experimental data to Ansoft data it was readily noticed that we had to filter out the background noise and average the amplitude across the center to obtain data with a consistent pattern. After analyzing the data further, we also realized that only portions of the data showed a pattern (either the real part or imaginary part) except in the case of 500Hz. This was a result of the phase information. Therefore, we performed a thorough analysis of the phase data, including analyzing changes in data when a phase shift was incorporated, when the phase data was averaged across the center of the sample as was done with the amplitude and finally when using both a phase shift with averaging.

We then performed initial trials in detecting the length of the damage which resulted in extremely poor estimated parameters. When comparing the POD approximations to the actual data, it was apparent that on the ends of the sample, the data and approximations did not match. This is most likely to due to both boundary effects and the error induced when we filter out the background noise. Therefore, we considered alternative cost criterions which only took into account the important aspects of the data - the *location* and *values* of the maximum and minimum points of the data set. We provided comparisons of results using only the values of the maximum and minimum in the inverse problem as opposed to using the whole set of data between *and* including these peaks. We did this for each frequency.

After initial trials, included in Appendix C, we concluded that the most accurate results only took into account those portions of the data which originally displayed a pattern. This resulted in a different cost criterion for each frequency. However, even though we justified the choice of the respective cost criterions for each frequency through comparisons between the POD approximations for various lengths and the actual data, the decision of which cost criterion to use could be made by simply

examining the data. One would only need to discern whether or not the data exhibited a pattern in either the real portion of the data or the imaginary portion of the data. Furthermore, to apply these results in a practical setting, it would be necessary to either develop a model that accurately portrays the data (as discussed previously) or to collect data over a period of time, building a data base which inherently contained the variations in the data. With this extensive data set, we would be able to discern the pattern in the data *a priori* and thus use an automatic cost criterion for each source frequency.

Thus, assuming a fixed source frequency and its associated cost criterion, we were able to demonstrate that the POD method in conjunction with inverse problems is a viable method even with experimental data. Depending on the frequency used, we were able to quite accurately estimate the length and depth alone. Estimating the two parameters simultaneously was a little more difficult; however, we still obtained reasonable results. In estimating length alone, using either 500Hz with the phased shifted or 1kHz with raw phase produced accurate results when comparing data across all the data points between and including the maximum and minimum. In a few cases using 250Hz or 2kHz also produced fairly accurate; however, results using these frequencies were not consistent. In determining the depth of the damage alone, frequencies 500Hz and 1kHz again produced accurate results for any depth at any fixed length with less than 10% error. A frequency of 2kHz also produce accurate results except for a depth of $d^* = 4mm$ (probably due to skin depth). 250Hz only proved to be a viable frequency for detecting the depth of the damage when the damage had a fixed length of $2cm$. More trials would need to be performed to determine if it is necessary for a damage to be of a certain length before a frequency of 250Hz would be useful. When estimating length and depth simultaneously at a fixed frequency of 1kHz, the results were not accurate. However, using 500Hz produced accurate results in many cases. Therefore, the method again proved to be feasible.

In some cases, depending on the length or depth of the damage, certain frequencies were found to be more accurate than others; therefore, the most accurate results

may be found by using the reduced order POD methodology together with another NDE technique. For example, the magneto-optic/eddy current imager ([18, 47]) is a visually based technique which displays crack images or images of the magnetic fields surrounding the actual crack. An estimate of the crack length may be obtained from these images giving us *a priori* knowledge of the damage. Based upon these estimates, a source frequency as well as an initial guess for the optimization routine can be chosen giving us valuable information for use in the inverse problem.

In conclusion, given the data available, we have shown we can *successfully* use our proposed reduced order computational methodology to determine both the length and depth of a damage within a sample (both separately and simultaneously). Moreover, since we only used a few basis elements (due to the small sample size), the results were obtained quite quickly, giving us a method which is both fast and accurate on experimental data. Indeed this chapter gives concrete results indicating that the POD methodology in conjunction with appropriate least squares techniques is a practical approach to nondestructive damage detection.

Chapter 7

Conclusions and Future Research Directions

7.1 Concluding Remarks

In this dissertation, we began by introducing the concept of nondestructive evaluation (the process of examining a material or article without impairing its future usefulness) and its importance to industrial applications, such as in design, production, and especially in quality control and maintenance. We briefly mentioned the various types of nondestructive evaluation (NDE) techniques and then focused on a particular NDE method, called an eddy current method, in which a current (eddy current) is induced in the sample material by placing a conducting sheet or current carrying material in close proximity. When a flaw or damage is present, the flow of the eddy current will be disrupted causing a disruption in the resulting magnetic flux density detected by a sensor placed above the material.

In Chapter 2, we developed a model for this specific eddy current method making some simplifying assumptions reducing the three-dimensional problem to a two-dimensional problem. We utilized a mathematical tool called phasors where complex valued fields were employed allowing us to suppress the time-dependence. Furthermore, for computational purposes, we introduced two new quantities, a magnetic

vector potential and a scalar electric potential, deriving the boundary value problem for the magnetic vector potential with some additional constraints on the electric scalar potential. Given the magnetic vector potential, we could easily derive the magnetic flux density necessary for the parameter estimation problem.

In Chapter 3 we presented some theoretical results which established the existence and uniqueness of solutions as well as continuous dependence of the solution on the parameters which represent the damage. We further discussed theoretical issues concerning the least squares parameter estimation problem we used to identify the geometry of the damage.

Since the parameter estimation problem involves solving the forward problem numerous times, we needed extremely fast and accurate solution methods. Therefore, in Chapter 4, we introduced the reduced order POD method which allows one to create a set of basis elements spanning a data set consisting of either numerical simulations or experimental data. The POD method is unique in that the majority of information is captured in just a few basis elements, allowing us to use a smaller number of basis elements for each forward solution. This results in a substantial decrease in total computational time. In Chapter 4, we also investigated two different approaches in forming the POD approximation, a POD/Galerkin technique and a POD/Interpolation technique and concluded that in *this* problem, the POD/Interpolation method gave a much better approximation than the POD/Galerkin method. Furthermore, using only three basis elements with the POD/Galerkin method we still obtained an approximation with less than a 7% relative error when compared to a finite element solution using more than 7000 finite elements. Using the POD/Interpolation method, we achieved less than a 1% relative error using four or more POD basis elements.

In Chapter 5, we presented parameter estimation results when estimating one or two parameter values using simulated data. In both cases, we were able to achieve extremely accurate results even with 10% relative noise added. In addition, on average we estimated a total reduction in time of a factor ranging from 10^2 to 10^3.

Finally, in Chapter 6 we offered results of the parameter estimation problem when

using experimental data obtained from a giant magnetoresistive (GMR) sensor. The experimental results were based on successfully using actual experimental data to form the POD basis elements (instead of numerical simulations) and thus illustrated the effectiveness of this method on a wide range of applications. In other words, whenever it is difficult to model the physical process but "good" data is available, the POD method may be a viable option. Taken as a whole, our work here indicates that using a POD computational method in NDE research can be an attractive alternative to the standard finite element methods, offering the potential for substantial savings in total computational time.

7.2 Future Work

Throughout this dissertation we have mentioned areas where further work remains to be done. This section is a collection of those ideas.

7.2.1 Collection and Analysis of More Experimental Data

In Chapter 6, we analyzed experimental data obtained from a GMR sensor at various frequencies. In the parameter estimation problem, we determined that based upon the frequency, it was necessary to use only one component of the data (either real or imaginary part) with either raw phase data or phase data containing a phase shift in order to obtain the most accurate results. In order to conclude that the data will always behave in this manner, it would be necessary to obtain more data and compare it to the data presented in this dissertation. Furthermore, in order to implement this methodology in a practical setting, it would ultimately be necessary to create an extensive data base for magnetic flux density data detected by a sensor which is associated with some damage. Another possibility involves developing a model that accurately portrays the data (discussed below).

7.2.2 A Three-Dimensional Eddy Current Model

Another factor which was mentioned in Chapter 6 was the need for a full three-dimensional model. When using experimental data obtained from samples with damages, it was necessary to snapshot on the data itself since the two-dimensional model did not accurately portray the data. We suggested many reasons why the model may not have been appropriate; a main factor was that we were using a two-dimensional model to capture the effects of a three-dimensional problem. Therefore, a practical next step would be to develop a full three-dimensional model and to test the POD methodology on this model. However, the three-dimensional problem is more complicated. In the two-dimensional case, we assumed we had uniformity in the direction of the current flow and thus could conclude the gradient of the scalar potential was piecewise constant. This condition no longer holds in the three-dimensional case; hence, the derivation and computations become more difficult. As a final step in the modeling process, to implement the proposed methodology in a practical setting, it would be necessary to consider a sample which is not only rectangular but is in the shape of the structures examined in the field, such as airplanes and pipelines. Needless to say, this complicates the modeling and numerical process even further.

Appendix A

The POD/Galerkin vs POD/Interpolation Methods

Chapter 4 discuss two different methods for forming the reduced order POD approximation of the magnetic vector potential A. One technique uses a POD/Galerkin method and the other a POD/Interpolation method. This appendix gives full set of tables discussed in that chapter.

A.1 The POD/Galerkin Method - Condition of the Linear System

The table below is a table containing the full set of condition numbers for the linear system used in the POD/Galerkin method for all values of N, $N = 1, ..., 21$.

Table A.1: Condition Number of the Linear System, (4.5), Used in Solving for α

N	Condition Number for Linear System
1	1.0000
2	3.8635
3	80.7903
4	359.2911
8	2818.0875
9	2917.7668
10	3413.3963
11	3422.5847
12	3495.9801
13	3550.7914
14	3799.2777
15	4327.3755
16	4329.3495
17	5308.7529
18	7463.0225
19	9870.1694
20	12,145.8738
21	12,431.3195

A.2 Relative Error Depending on the Method

A.2.1 POD/Galerkin Method

The table below gives the average relative error in the POD approximation of the magnitude of B_2 along a line above the conducting sheet using the POD/Galerkin Method compared to finite element simulations using Ansoft Maxwell 2D Field Simulator for all values of N, $N = 1, ..., 21$.

Table A.2: Average Relative Error in the POD Approximation of the Magnitude of B_2 for Various Values of N across a Line Located $1mm$ above the Conducting Sheet using the POD/Galerkin Method

N	Average Relative Error
1	52.05%
2	7.16%
3	6.31%
4	10.97%
5	11.94%
6	15.70%
7	14.42%
8	15.15%
9	18.30%
10	26.92%
11	26.92%
12	29.23%
13	25.91%
14	28.03%
15	71.39%
16	97.38%
17	127.42%
18	104.21%
19	87.50%
20	209.25%
21	208.47%

A.2.2 POD/Interpolation Method

The table below gives the average relative error in the POD approximation of the magnitude of B_2 along a line above the conducting sheet using the POD/Interpolation Method compared to finite element simulations using Ansoft Maxwell 2D Field Simulator for all values of N, $N = 1, ..., 21$.

Table A.3: Average Relative Error in the POD Approximation of the Magnitude of B_2 for Various Values of N across a Line Located $1mm$ above the Conducting Sheet using the POD/Interpolation Method

N	Average Relative Error
1	51.69%
2	1.95%
3	1.14%
4	0.63%
5	0.55%
6	0.79%
7	0.79%
8	0.72%
9	0.72%
10	0.72%
11	0.74%
12	0.72%
13	0.51%
14	0.52%
15	0.56%
16	0.57%
17	0.70%
18	0.70%
19	0.74%
20	0.76%
21	0.91%

Appendix B

Simulated Results: Estimating Depth

B.1 Estimation of Depth Depending on the Number N of POD Basis Elements Used

Table B.1: Determination of Depth $d^* = 1mm$ with No Noise

N POD Basis Elements	Estimated Depth d	Relative Error
3	0.8591	14.09%
4	1.0190	1.90%
5	1.0603	6.03%
6	1.0636	6.36%
7	1.0530	5.30%
8	1.0386	3.86%
9	1.0262	2.62%
10	1.0103	1.04%
11	1.0005	0.05%
12	0.9984	0.16%
13	0.9946	0.54%
14	0.9941	0.59%
15	0.9905	0.95%
16	0.9868	1.32%
17	0.9872	1.28%
18	0.9822	1.78%
19	0.9843	1.57%
20	0.9830	1.70%

Table B.2: Determination of Depth $d^* = 2mm$ with No Noise

N POD Basis Elements	Estimated Depth d	Relative Error
3	2.2998	14.99%
4	2.2251	11.26%
5	2.1396	6.98%
6	2.0704	3.52%
7	2.0219	1.10%
8	1.9980	1.00%
9	1.9866	1.34%
10	1.9874	0.63%
11	1.9901	0.49%
12	1.9914	0.43%
13	1.9943	0.28%
14	1.9955	0.22%
15	1.9958	0.21%
16	2.0069	0.34%
17	2.0030	0.15%
18	2.0047	0.24%
19	2.0025	0.12%
20	2.0015	0.08%

Table B.3: Determination of Depth $d^* = 3mm$ with No Noise

N POD Basis Elements	Estimated Depth d	Relative Error
3	3.4306	14.35%
4	3.1829	6.10%
5	3.0359	1.20%
6	2.9631	1.23%
7	2.9490	1.70%
8	2.9629	1.24%
9	2.9882	1.18%
10	3.0145	0.48%
11	3.0347	1.16%
12	3.0383	1.28%
13	3.0391	1.30%
14	3.0355	1.18%
15	3.0294	0.98%
16	3.0150	0.50%
17	3.0201	0.67%
18	3.0191	0.64%
19	3.0234	0.78%
20	3.0282	0.94%

Table B.4: Determination of Depth $d^* = 4mm$ with No Noise

N POD Basis Elements	Estimated Depth d	Relative Error
3	4.3774	9.44%
4	4.0379	0.95%
5	3.9198	2.01%
6	3.9348	1.63%
7	3.9948	0.13%
8	4.0343	0.86%
9	4.0516	1.29%
10	4.0421	1.05%
11	4.0142	0.36%
12	4.0108	0.27%
13	4.0070	0.18%
14	4.0077	0.19%
15	4.0115	0.29%
16	4.0212	0.53%
17	4.0226	0.56%
18	4.0267	0.67%
19	4.0237	0.59%
20	4.0293	0.73%

Table B.5: Determination of Depth $d^* = 5mm$ with No Noise

N POD Basis Elements	Estimated Depth d	Relative Error
3	5.1894	3.79%
4	4.8124	3.75%
5	4.8333	3.33%
6	4.9628	0.74%
7	5.0294	0.59%
8	5.0458	0.92%
9	4.9993	0.01%
10	4.9800	0.40%
11	4.9994	0.01%
12	5.0446	0.89%
13	5.0796	1.59%
14	5.0797	1.59%
15	5.0652	1.30%
16	5.0434	0.87%
17	5.0530	1.06%
18	5.0542	1.08%
19	5.0568	1.14%
20	5.0595	1.19%

Table B.6: Determination of Depth $d^* = 6mm$ with No Noise

N POD Basis Elements	Estimated Depth d	Relative Error
3	5.9678	0.54%
4	5.6830	5.28%
5	5.9103	1.50%
6	6.0518	0.86%
7	6.0648	1.03%
8	5.9899	0.17%
9	5.9683	0.53%
10	5.9877	0.21%
11	6.0244	0.41%
12	6.0715	1.19%
13	6.0995	1.66%
14	6.1014	1.67%
15	6.0948	1.58%
16	6.1239	2.07%
17	6.1369	2.28%
18	6.1511	2.52%
19	6.1513	2.52%
20	6.1388	2.31%

Table B.7: Determination of Depth $d^* = 7mm$ with No Noise

N POD Basis Elements	Estimated Depth d	Relative Error
3	-	
4	6.5447	6.50%
5	7.0592	0.85%
6	7.0973	1.39%
7	6.9793	0.30%
8	6.9602	3.98%
9	6.9557	0.63%
10	7.0552	0.79%
11	6.9934	0.09%
12	7.0050	0.07%
13	7.0094	0.13%
14	7.0124	0.18%
15	6.9942	0.08%
16	7.0175	0.25%
17	7.0007	0.01%
18	6.9497	0.72%
19	6.9677	0.46%
20	6.9065	1.34%

Table B.8: Determination of Depth $d^* = 8mm$ with No Noise

N POD Basis Elements	Estimated Depth d	Relative Error
3	7.4288	7.14%
4	7.7596	3.01%
5	8.0659	0.82%
6	7.9768	0.29%
7	7.8358	2.05%
8	7.8698	1.63%
9	7.9477	0.65 %
10	7.9027	1.22%
11	7.8981	1.27%
12	7.8812	1.49%
13	7.8745	1.57%
14	7.9102	1.12%
15	7.9199	1.00%
16	7.9394	0.76%
17	7.9401	0.75%
18	7.9121	1.10%
19	7.9233	0.96%
20	7.9530	0.59%

Table B.9: Determination of Depth $d^* = 9mm$ with No Noise

N POD Basis Elements	Estimated Depth d	Relative Error
3	8.0435	10.63%
4	8.9726	0.30%
5	9.0200	0.22%
6	8.6932	3.41%
7	8.9102	1.00%
8	8.6772	3.59%
9	8.8674	1.47%
10	9.0400	0.45%
11	9.0083	0.09%
12	9.0153	0.17%
13	9.1707	1.90%
14	9.1842	2.05%
15	9.2360	2.62%
16	-	-
17	9.2522	2.80%
18	9.3223	3.58%
19	9.3080	3.42%
20	9.3300	3.67%

Table B.10: Determination of Depth $d^* = 10mm$ with No Noise

N POD Basis Elements	Estimated Depth d	Relative Error
3	9.2995	7.01%
4	9.8663	1.34%
5	9.9888	0.11%
6	9.7723	2.28%
7	9.8389	1.61%
8	9.9038	0.96%
9	9.8254	1.75%
10	9.8426	1.57%
11	9.9460	0.54%
12	9.8217	1.78%
13	9.8223	1.78%
14	9.8182	1.82%
15	9.6962	3.04%
16	9.8546	1.45%
17	9.6633	3.37%
18	9.6703	3.30%
19	9.6633	3.37%
20	9.6683	3.32%

Table B.11: Determination of Depth $d^* = 11mm$ with No Noise

N POD Basis Elements	Estimated Depth d	Relative Error
3	11.7091	6.45%
4	10.9988	0.01%
5	10.9199	0.73%
6	10.9923	0.07%
7	11.0924	0.84%
8	11.0632	0.58%
9	11.0189	0.17%
10	11.0770	0.70%
11	11.0406	0.37%
12	11.1338	1.22%
13	11.1514	1.38%
14	11.1383	1.26%
15	11.1592	1.45%
16	11.1888	1.72%
17	11.3571	3.25%
18	11.1792	1.63%
19	11.3225	2.93%
20	11.1132	1.03%

Table B.12: Determination of Depth $d^* = 12mm$ with No Noise

N POD Basis Elements	Estimated Depth d	Relative Error
3	13.2498	10.42%
4	12.2770	2.31%
5	11.8120	1.57%
6	11.8971	0.86%
7	12.0885	0.74%
8	11.9287	0.59%
9	11.9638	0.30%
10	12.0331	0.28%
11	11.9533	0.39%
12	11.9325	0.56%
13	11.9230	0.64%
14	11.9581	0.35%
15	11.9365	0.53%
16	11.4919	4.24%
17	11.4869	4.28%
18	11.9619	0.32%
19	11.9939	0.05%
20	12.0360	0.30%

Table B.13: Determination of Depth $d^* = 13mm$ with No Noise

N POD Basis Elements	Estimated Depth d	Relative Error
3	13.3379	2.60%
4	14.0154	7.81%
5	12.5207	3.69%
6	12.5946	3.12%
7	12.6677	2.56%
8	13.0364	0.23%
9	13.0666	0.51%
10	12.4272	4.41%
11	13.1376	1.06%
12	13.4361	3.35%
13	13.5157	3.97%
14	12.1873	6.25%
15	12.1595	6.47%
16	12.3647	4.89%
17	12.1267	6.72%
18	12.1190	6.78%
19	12.3530	4.98%
20	12.1478	6.56%

Table B.14: Determination of Depth $d^* = 14mm$ with No Noise

N POD Basis Elements	Estimated Depth d	Relative Error
3	13.8889	0.79%
4	14.6003	4.29%
5	14.0560	0.40%
6	14.4854	3.47%
7	13.8578	1.02%
8	13.8737	0.90%
9	13.9620	0.27%
10	13.9253	0.53%
11	13.6309	2.64%
12	13.8457	1.02%
13	13.9843	0.11%
14	14.1256	0.90%
15	14.1415	1.01%
16	14.0024	0.02%
17	13.9699	0.21%
18	14.0269	0.19%
19	14.0775	0.55%
20	14.2474	1.77%

Table B.15: Determination of Depth $d^* = 15mm$ with No Noise

N POD Basis Elements	Estimated Depth d	Relative Error
3	14.6353	2.43%
4	15.3833	2.56%
5	16.0989	7.33%
6	15.7500	5.00%
7	16.2500	8.33%
8	15.0237	0.16%
9	14.4594	3.60%
10	14.3702	4.20%
11	15.2817	1.88%
12	15.4066	2.71%
13	15.2710	1.81%
14	16.6563	11.04%
15	16.6580	11.05%
16	17.0658	13.77%
17	14.0907	6.06%
18	14.1732	5.51%
19	14.1860	5.43%
20	14.2696	4.87%

Table B.16: Determination of Depth $d^* = 16mm$ with No Noise

N POD Basis Elements	Estimated Depth d	Relative Error
3	14.7500	7.81%
4	15.9242	0.47%
5	16.0123	0.08%
6	16.6686	4.18%
7	16.5243	3.28%
8	17.5948	9.97%
9	17.7006	10.63%
10	17.7241	10.78%
11	15.4440	3.47%
12	17.8127	11.33%
13	17.6769	10.48%
14	17.4802	9.25%
15	17.4107	8.82%
16	17.4251	8.91%
17	17.4820	9.26%
18	17.4439	9.02%
19	17.4492	9.06%
20	17.4581	9.11%

Table B.17: Determination of Depth $d^* = 17mm$ with No Noise

N POD Basis Elements	Estimated Depth d	Relative Error
3	14.8315	12.76%
4	16.4707	3.11%
5	16.7500	1.47%
6	17.0528	0.31%
7	17.4689	2.76%
8	17.6896	4.06%
9	17.7260	4.27%
10	17.8303	4.88%
11	17.8460	4.98%
12	17.9433	5.55%
13	17.8679	5.11%
14	17.5136	3.02%
15	17.4356	2.56%
16	17.4531	2.67%
17	17.5005	2.94%
18	18.4670	8.63%
19	18.4562	8.57%
20	18.5091	8.88%

B.2 Estimation of Depth With 10% Relative Noise

Table B.18: Determination of Depth $d^* = 1mm$ with 10% Relative Noise Added Using $N = 5$

Trial	Est. Depth (mm)	Relative Error
1	1.0672	6.72%
2	1.0639	6.39%
3	1.0365	3.65%
4	1.0439	4.39%
5	1.0399	3.99%
6	1.0177	1.77%
7	1.0358	3.58%
8	1.0546	5.46%
9	1.0711	7.11%
10	1.0830	8.30%
Mean (mm)	Median (mm)	Average Relative Error
1.0514	1.0492	5.14%
Standard Deviation (mm)	Variance (mm^2)	
0.02	0.3992×10^{-3}	

Table B.19: Determination of Depth $d^* = 2mm$ with 10% Relative Noise Added Using $N = 5$

Trial	Est. Depth (mm)	Relative Error
1	2.1521	7.60%
2	2.1710	8.55%
3	2.1391	6.96%
4	2.1423	7.12%
5	2.1312	6.56%
6	2.1229	6.15%
7	2.1224	6.12%
8	2.1539	7.69%
9	2.1396	6.98%
10	2.1039	5.20%
Mean (mm)	Median (mm)	Average Relative Error
2.1378	2.1393	6.89%
Standard Deviation (mm)	Variance (mm^2)	
0.0190	0.3602×10^{-3}	

Table B.20: Determination of Depth $d^* = 4mm$ with 10% Relative Noise Added Using $N = 5$

Trial	Est. Depth (mm)	Relative Error
1	3.8985	2.54%
2	3.8967	2.58%
3	3.9175	2.06%
4	3.8879	2.80%
5	3.9300	1.75%
6	3.9229	1.93%
7	3.8952	2.62%
8	3.9420	1.45%
9	3.8969	2.58%
10	3.9207	1.98%
Mean (mm) 3.9108	Median (mm) 3.9080	Average Relative Error 2.23%
Standard Deviation (mm) 0.0181	Variance (mm^2) 0.3270×10^{-3}	

Table B.21: Determination of Depth $d^* = 5mm$ with 10% Relative Noise Added Using $N = 5$

Trial	Est. Depth (mm)	Relative Error
1	4.8431	3.14%
2	4.8393	3.21%
3	4.8485	3.03%
4	4.8241	3.52%
5	4.8268	3.46%
6	4.8565	2.87%
7	4.8268	3.46%
8	4.8402	3.20%
9	4.8539	2.92%
10	4.8410	3.18%
Mean (mm) 4.8400	Median (mm) 4.8406	Average Relative Error 3.20%
Standard Deviation (mm) 0.0113	Variance (mm^2) 0.1277×10^{-3}	

Table B.22: Determination of Depth $d^* = 6mm$ with 10% Relative Noise Added Using $N = 5$

Trial	Est. Depth (mm)	Relative Error
1	5.9001	1.67%
2	5.9022	1.63%
3	5.9064	1.56%
4	5.9206	1.32%
5	5.8831	1.95%
6	5.9291	1.18%
7	5.8884	1.86%
8	5.9168	1.39%
9	5.9098	1.50%
10	5.9081	1.53%
Mean (mm) 5.9065	Median (mm) 5.9073	Average Relative Error 1.56%
Standard Deviation (mm) 0.0140	Variance (mm^2) 0.1957×10^{-3}	

Table B.23: Determination of Depth $d^* = 7mm$ with 10% Relative Noise Added Using $N = 5$

Trial	Est. Depth (mm)	Relative Error
1	7.0482	0.69%
2	7.0597	0.85%
3	7.0249	0.36%
4	7.0680	0.97%
5	7.0821	1.17%
6	7.0767	1.10%
7	7.0647	0.92%
8	7.0748	1.07%
9	7.0455	0.65%
10	7.0416	0.59%
Mean (mm) 7.0586	Median (mm) 7.0622	Average Relative Error 0.84%
Standard Deviation (mm) 0.0182	Variance (mm^2) 0.3299×10^{-3}	

Table B.24: Determination of Depth $d^* = 9mm$ with 10% Relative Noise Added Using $N = 5$

Trial	Est. Depth (mm)	Relative Error
1	9.0240	0.27%
2	9.0537	0.60%
3	9.0259	0.29%
4	9.0512	0.57%
5	9.0149	0.17%
6	9.0321	0.36%
7	8.9939	0.07%
8	9.0053	0.06%
9	9.0183	0.20%
10	8.9949	0.06%
Mean (mm) 9.0214	Median (mm) 9.0211	Average Relative Error 0.26 %
Standard Deviation (mm) 0.0207	Variance (mm^2) 0.4273×10^{-3}	

Table B.25: Determination of Depth $d^* = 10mm$ with 10% Relative Noise Added Using $N = 5$

Trial	Est. Depth (mm)	Relative Error
1	9.9928	0.07%
2	9.9902	0.10%
3	10.0080	0.08%
4	9.9833	0.17%
5	10.0118	0.12%
6	10.0004	0.01%
7	9.9745	0.26%
8	10.0072	0.07%
9	9.9675	0.33%
10	9.9868	0.13%
Mean (mm) 9.9923	Median (mm) 9.9915	Average Relative Error 0.13%
Standard Deviation (mm) 0.0148	Variance (mm^2) 0.2180×10^{-3}	

Table B.26: Determination of Depth $d^* = 12mm$ with 10% Relative Noise Added Using $N = 5$

Trial	Est. Depth (mm)	Relative Error
1	11.8100	1.58%
2	11.8028	1.64%
3	11.8090	1.59%
4	11.822	1.48%
5	11.8100	1.58%
6	11.8101	1.58%
7	11.8206	1.50%
8	11.8123	1.56%
9	11.8211	1.49%
10	11.8235	1.47%
Mean (mm) 11.8142	Median (mm) 11.8112	Average Relative Error 1.55%
Standard Deviation (mm) 0.0071	Variance (mm^2) 0.5046×10^{-4}	

Appendix C

Supplementary Experimental Results

In Chapter 6 we analyzed data when the phase had been modified in various ways. Using a phase shift, we obtained data which showed a pattern in both the real *and* imaginary portions; however, the results of the inverse problem were better when using only one or the other (real or imaginary). Here we offer to the interested reader the results of the parameter estimation problem when both portions of data are used. These results can be compared with those presented in Chapter 6. Using the notation of Chapter 6, we define J^s_{maxmin} to be the cost criterion in which only the minimum and maximum values are compared using data containing a phase shift, and J^s_{mid} to be the cost criterion in which the entire center portion of the sample is considered (again using data containing a phase shift). In other words, we have

$$J^s_{maxmin} = J^s_{maxminRe} + J^s_{maxminIm} \tag{C.1}$$

and

$$J^s_{mid} = J^s_{midRe} + J^s_{midIm} \tag{C.2}$$

where $J^s_{maxminRe}$, $J^s_{maxminIm}$, J^s_{midRe} and J^s_{midIm} are defined as in Chapter 6 by

$$\begin{aligned} J^s_{maxminRe}(\mathbf{q}) &= \frac{10^{24}}{2}\left|\max_{1\le j\le n} Re(B^N_{2s}(x_j;\mathbf{q})) - \max_{1\le j\le n} Re(\hat{B}^j_{2s})\right|^2 \\ &\quad + \frac{10^{24}}{2}\left|\min_{1\le j\le n} Re(B^N_{2s}(x_j;\mathbf{q})) - \min_{1\le j\le n} Re(\hat{B}^j_{2s})\right|^2, \end{aligned} \tag{C.3}$$

$$J^s_{maxminIm}(\mathbf{q}) = \frac{10^{24}}{2}\left|\max_{1\le j\le n} Im(B^N_{2s}(x_j;\mathbf{q})) - \max_{1\le j\le n} Im(\hat{B}^j_{2s})\right|^2 + \frac{10^{24}}{2}\left|\min_{1\le j\le n} Im(B^N_{2s}(x_j;\mathbf{q})) - \min_{1\le j\le n} Im(\hat{B}^j_{2s})\right|^2, \quad \text{(C.4)}$$

$$J^s_{midRe}(\mathbf{q}) = \frac{1}{2}\sum_{j=a_{Re}-2}^{b_{Re}+2}\left|10^9 Re(B^N_{2s}(x_j;\mathbf{q})) - 10^9 Re(\hat{B}^j_{2s})\right|^2, \quad \text{(C.5)}$$

and

$$J^s_{midIm}(\mathbf{q}) = \frac{1}{2}\sum_{j=a_{Im}-2}^{b_{Im}+2}\left|10^9 Im(B^N_{2s}(x_j;\mathbf{q})) - 10^9 Im(\hat{B}^j_{2s})\right|^2. \quad \text{(C.6)}$$

Given the above notation, the results for 250Hz, 500Hz, 1kHz, and 2kHz is given below

C.1 Determination of Length with Frequency 250Hz

Table C.1: Determination of Length at a Frequency of 250Hz Using (C.1) when Modifications of Experimental Data include Averaging Magnitude, Filtering Out Background Noise, and Shifting Phase Data

Depth(mm)	Actual Length(cm)	Optimized Length(cm)	Relative Error
2	1.0	1.7249	72.49 %
	1.5	2.5475	69.84 %
	2.0	1.2444	37.78 %
3	1.0	1.0564	5.64 %
	1.5	1.3304	11.32 %
	2.0	2.9491	47.45 %
4	1.0	2.2292	122.92%
	1.5	1.7071	13.81%
	2.0	2.7698	38.49%

Table C.2: Determination of Length at a Frequency of 250Hz Using (C.2) when Modifications of Experimental Data include Averaging Magnitude, Filtering Out Background Noise, and Shifting Phase Data

Depth(mm)	Actual Length(cm)	Optimized Length(cm)	Relative Error
2	1.0	-	-
	1.5	2.1683	44.55%
	2.0	1.2699	36.51%
3	1.0	1.2073	20.73%
	1.5	1.2938	13.75%
	2.0	1.5160	24.20%
4	1.0	0.8325	16.75%
	1.5	1.6640	10.93%
	2.0	1.2369	38.16%

C.2 Determination of Length with Frequency 500Hz

Table C.3: Determination of Length at a Frequency of 500Hz Using (C.1) when Modifications of Experimental Data include Averaging Magnitude, Filtering Out Background Noise, and Shifting Phase Data

Depth(mm)	Actual Length(cm)	Optimized Length(cm)	Relative Error
2	1.0	0.9960	0.40%
	1.5	1.4378	4.14%
	2.0	2.2609	13.04%
3	1.0	1.0702	7.02%
	1.5	1.3873	7.51%
	2.0	1.6202	18.99%
4	1.0	-	-
	1.5	2.4930	66.20%
	2.0	2.0472	2.36%

Table C.4: Determination of Length at a Frequency of 500Hz Using (C.2) when Modifications of Experimental Data include Averaging Magnitude, Filtering Out Background Noise, and Shifting Phase Data

Depth(mm)	Actual Length(cm)	Optimized Length(cm)	Relative Error
2	1.0	1.1804	18.04%
	1.5	1.6450	9.67%
	2.0	2.9259	46.29%
3	1.0	1.1252	12.52%
	1.5	1.4162	5.59%
	2.0	1.5687	21.57%
4	1.0	1.0500	5.00%
	1.5	1.5275	1.83%
	2.0	1.8298	8.51%

C.3 Determination of Length with Frequency 1kHz

Table C.5: Determination of Length at a Frequency of 1kHz Using (C.1) when Modifications of Experimental Data include Averaging Magnitude, Filtering Out Background Noise, and Shifting Phase Data

Depth(mm)	Actual Length(cm)	Optimized Length(cm)	Relative Error
2	1.0	0.7114	28.86%
	1.5	-	-
	2.0	2.5115	25.57%
3	1.0	1.5198	51.98%
	1.5	-	-
	2.0	1.4732	26.34%
4	1.0	-	-
	1.5	1.8675	24.50%
	2.0	1.6224	18.88%

Table C.6: Determination of Length at a Frequency of 1kHz Using (C.2) when Modifications of Experimental Data include Averaging Magnitude, Filtering Out Background Noise, and Shifting Phase Data

Depth(mm)	Actual Length(cm)	Optimized Length(cm)	Relative Error
2	1.0	0.8493	15.07%
	1.5	1.6604	10.69%
	2.0	2.8942	44.71%
3	1.0	1.0432	4.32%
	1.5	1.6594	10.63%
	2.0	1.6350	18.25%
4	1.0	1.1496	14.96%
	1.5	1.7199	14.66%
	2.0	1.6818	15.91%

In the case of 1kHz, even when we use only the imaginary portion of the data, we still do not achieve accurate results.

Table C.7: Determination of Length at a Frequency of 1kHz Using Imaginary Part of (C.1) when Modifications of Experimental Data include Averaging Magnitude, Filtering Out Background Noise, and Shifting Phase Data

Depth(mm)	Actual Length(cm)	Optimized Length(cm)	Relative Error
2	1.0	1.4486	44.86%
	1.5	1.1247	25.02%
	2.0	2.3294	16.47%
3	1.0	1.1655	16.55%
	1.5	-	-
	2.0	1.4297	28.51%
4	1.0	-	-
	1.5	1.9075	27.16%
	2.0	1.6048	19.76%

Table C.8: Determination of Length at a Frequency of 1kHz Using Imaginary Part of (C.2) when Modifications of Experimental Data include Averaging Magnitude, Filtering Out Background Noise, and Shifting Phase Data

Depth(mm)	Actual Length(cm)	Optimized Length(cm)	Relative Error
2	1.0	1.2922	29.22%
	1.5	1.9289	28.59%
	2.0	1.3732	31.34%
3	1.0	1.1945	19.45%
	1.5	1.6574	10.49%
	2.0	1.6164	19.18%
4	1.0	1.2043	20.43%
	1.5	1.7189	14.60%
	2.0	1.7014	14.93%

C.4 Determination of Length with Frequency 2kHz

Table C.9: Determination of Length at a Frequency of 2kHz Using (C.1) when Modifications of Experimental Data include Averaging Magnitude, Filtering Out Background Noise, and Shifting Phase Data

Depth(mm)	Actual Length(cm)	Optimized Length(cm)	Relative Error
2	1.0	0.7519	24.81%
	1.5	2.5556	70.37%
	2.0	1.4257	28.71%
3	1.0	0.9192	8.08%
	1.5	1.8967	26.45%
	2.0	1.6208	18.96%
4	1.0	2.7496	174.96%
	1.5	2.7041	80.27%
	2.0	0.9322	53.39%

Table C.10: Determination of Length at a Frequency of 2kHz Using (C.2) when Modifications of Experimental Data include Averaging Magnitude, Filtering Out Background Noise, and Shifting Phase Data

Depth(mm)	Actual Length(cm)	Optimized Length(cm)	Relative Error
2	1.0	0.6662	33.38%
	1.5	1.5939	6.26%
	2.0	2.8935	44.68%
3	1.0	0.8156	18.44%
	1.5	1.7346	15.64%
	2.0	2.9504	47.52%
4	1.0	1.7570	75.70%
	1.5	2.8586	90.57%
	2.0	1.2219	38.91%

List of References

[1] Ansoft Corporation. *Maxwell 2D Field Simulator - Technical Notes*, 1995-1999.

[2] J.A. Atwell and B.B. King. Reduced order controllers for spatially distributed systems via proper orthogonal decomposition. ICAM Report 99-07-01, Virginia Polytechnic Institute and State University, Blacksburg, VA, July 1999.

[3] H.T. Banks, R.C. del Rosario, and R.C. Smith. Reduced order model feedback control design: Numerical implementation in a thin shell model. *IEEE Trans. Auto. Control*, 45:1312–1324, July 2000.

[4] H.T. Banks, M.L. Joyner, B. Wincheski, and W.P. Winfree. Evaluation of material integrity using reduced order computational methodology. CRSC Tech. Rep. CRSC-TR99-30, North Carolina State University, 1999.

[5] H.T. Banks and F. Kojima. Boundary shape identification in two-dimensional electrostatic problems using SQUIDs. *J. Inv. Ill-Posed Problems*, 8(5):487–504, 2000.

[6] H.T. Banks and K. Kunisch. *Estimation techniques for distributed parameter systems*. Birkhauser, Boston, 1989.

[7] G. Berkooz. Observations on the proper orthogonal decomposition. In *Studies in Turbulence*, pages 229–247. Springer-Verlag, New York, 1992.

[8] G. Berkooz, P. Holmes, and J.L. Lumley. The proper orthogonal decomposition in the analysis of turbulent flows. *Annual Review of Fluid Mechanics*, 25(5):539–575, 1993.

[9] Don E. Bray. *Nondestructive Testing Techniques.* John Wiley & Sons, New York, 1992.

[10] C.F. Bryant, C.R.I. Emson, and C.W. Trowbridge. A comparison of lorentz gauge formulations in eddy current computations. *IEEE Transactions on Magnetics*, 26(2):430–433, 1990.

[11] Louis Cartz. *Nondestructive Testing.* ASM International, Materials Park, OH, 1995.

[12] David K. Cheng. *Field and Wave Electromagnetics.* Addison-Wesley, Reading, MA, second edition, 1992.

[13] A. Cochran, G.B. Dondaldson, C. Carr, D. McA. McKirdy, M.E. Walker, U. Klein, J. Kuznik, and A. McNab. Advances in the theory and practice of SQUID NDE. *Review in Progress in QNDE*, 15:1151–1158, 1996.

[14] R.C. del Rosario. *Computational Methods for Feedback Control in Structural Systems.* PhD thesis, North Carolina State University, 1998.

[15] G.B. Donaldson and D. McA. McKirdy. The use of SQUIDs for nondestructive evaluation. In *SQUID Sensors: Fundamentals, Fabrication and Application*, pages 599–628. Kluwer Academic Publishing, Boston, 1996.

[16] Robert S. Elliott. *Electromagnetics: History, Theory, and Applications.* IEEE Press, New York, 1993.

[17] Lawrence C. Evans. *Partial Differential Equations.* American Mathematical Society, Providence, 1991.

[18] G.L. Fitzpatrick, D.K. Thorne, R.L. Skaugset, E.Y.C. Shih, and W.C.L. Shih. Magneto-optic/eddy current imaging of aging aircraft: A new NDI technique. *Materials Evaluation*, 51:1402–1407, 1993.

[19] T.W. Guettinger, K. Grotz, and H. Wezel. Eddy current imaging. *Materials Evaluation*, 51:444–451, April 1993.

[20] R. Halmshaw. *Non-Destructive Testing.* Edward Arnold, London, second edition, 1991.

[21] N.C. Haywood and J.R. Bowler. Eddy-current imaging of buried cracks by inverting field data. *IEEE Trans. On Magnetics*, 28(2):1336–1339, 1992.

[22] C. A. Hogarth and J. Blitz, editors. *Techniques of Non-Destructive Testing.* Butterworths, London, 1960.

[23] J. D. Jackson. *Classical Electrodynamics.* John Wiley & Sons, New York, 2nd edition, 1975.

[24] W.G. Jenks and J.P. Wikswo Jr. Review article: SQUIDs for nondestructive evaluation. *Journal of Physics D: Applied Physics*, 30:293–323, 1997.

[25] K. Karhunen. Zur spektral theorie stochasticher prozesse. *Ann. Acad. Sci. Fennicae*, 37(A1), 1946.

[26] C.T. Kelley. *Iterative Methods for Optimization.* Society for Industrial and Applied Mathematics, Philadelphia, PA, 1999.

[27] G.M. Kepler, H.T. Tran, and H.T. Banks. Reduced order model compensator control of species transport in a CVD reactor. *Optimal Control: Applications and Methods*, 21(4):143–160, 2000.

[28] M. Kirby, J.P. Boris, and L. Sirovich. A proper orthogonal decomposition of a simulated supersonic shear layer. *International Journal for Numerical Methods in Fluids*, 10:411–428, 1990.

[29] M. Kirby and L. Sirovich. Application of the Karhunen-Loeve procedure for the characterization of human faces. *IEEE Transactions on Pattern Analysis and Machine Intelligence*, 12(1):103–108, 1990.

[30] A. Konrad. Integrodifferential finite element formulation of two-dimensional steady-state skin effect problems. *IEEE Transactions on Magnetics*, 18(1):284–292, 1981.

[31] A. Konrad. The numerical solution of steady-state skin effect problems - an integrodifferential approach. *IEEE Transactions on Magnetics*, 17(1):1148–1152, 1981.

[32] Andrzej Krawczyk and John A. Tegopoulos. *Numerical Modelling of Eddy Currents*. Oxford University Press, Oxford, 1993.

[33] E. E. Kriezis, Theodoros D. Tsiboukis, Stavros M. Panas, and Jon A. Tegopoulos. Eddy currents: Theory and applications. *Proceedings of the IEEE*, 80(10):1559–1589, 1992.

[34] K. Kunisch and S. Volkwein. Control of Burgers' equation by a reduced-order approach using proper orthogonal decomposition. *J. Optimization Theory and Applic.*, 102(2):345–371, 1999.

[35] M. Loeve. *Functions aleatoire de second ordre*. Compte rend. Acad. Sci., Paris, 1945.

[36] J.L. Lumley. The structure of inhomogeneous turbulent flows. *Atmospheric Turbulence and Radio Wave Propagation*, pages 166–178, 1967.

[37] J.L. Lumley. *Stochastic Tools in Turbulence*. Academic Press, New York, 1970.

[38] H.V. Ly and H.T. Tran. Proper orthogonal decomposition for flow calculations and optimal control in a horizontal cvd reactor. CRSC Tech. Rep. CRSC-TR98-13, North Carolina State University, 1998.

[39] Y.P. Ma and Jr. J.P. Wikswo. Imaging subsurface defects using a SQUID magnetometer. *Review of Progress in QNDE*, 12A:1137–1143, 1993.

[40] Warren J. McGonnagle. *Nondestructive Testing*. McGraw-Hill, New York, 1961.

[41] D. McA. McKirdy, A. Cochran, G.B. Donaldson, and A. McNab. Forward and inverse processing in electromagnetic NDE using SQUIDs. *Review of Progress in QNDE*, pages 347–354, 1996.

[42] Patrick O. Moore and Paul McIntire, editors. *Nondestructive Testing Overview*, volume Ten of *Nondestructive Testing Hanbook*. American Society for Nondestructive Testing, Inc., second edition, 1996.

[43] J.A. Nelder and R. Mead. A simplex method for function minimization. *Comput. J.*, 7:308–313, 1965.

[44] Alfio Quarteroni, Riccardo Sacco, and Fausto Saleri. *Numerical Mathematics*. Springer-Verlag, New York, 2000.

[45] J. Stoer and R. Burlisch. *Introduction to Numerical Analysis*. Springer-Verlag, New York, 2nd edition, 1993.

[46] Richard L. Stoll. *The Analysis of Eddy Currents*. Clarendon Press, Oxford, 1974.

[47] D.K. Thorne, G.L. Fitzpatrick, E.Y.C. Shih, and W.C.L. Shih. Aircraft inspection with the magneto-optic/eddy current imager - a new technology. In *ATA NDT Forum*, Long Beach, CA, Sept. 1991.

[48] I.A. Tsukerman, A. Konrad, and J.D. Lavers. A method for circuit connections in time-dependent eddy current problems. *IEEE Transactions on Magnetics*, 28(2):1299–1302, 1992.

[49] M. Vauhkonen, J.P. Kaipio, E. Somersalo, and P.A. Karjalainen. Electrical impedance tomography with basic constraints. *Inverse Problems*, 13:523–530, 1997.

[50] J. Weiss and Z. J. Csendes. A one-step finite element method for multiconductor skin effect problems. *IEEE Transactions on Power Apparatus and Systems*, 101(10):3796–3803, 1982.

[51] H. Wienstock. A review of SQUID magnetometry applied to nondestructive evaluation. *IEEE Transactions on Magnetics*, 27(2):3131–3236, 1991.

[52] B. Wincheski, J. Fulton, S. Nath, M. Namking, and J. Simpson. Self-nulling eddy current probe for surface and subsurface flaw detection. *Materials Evaluation*, 52(1):22–26, 1994.

[53] B. Wincheski, J. Fulton, S. Nath, and M. Namkung. Analysis of eddy current distribution and resulting flaw detection mechanism for self-nulling probe. *Review of Progress in Quantitative NDE*, 14A:291–298, 1995.

[54] Buzz Wincheski and Min Namkung. Development of very low frequency self-nulling probe for inspection of thick layered aluminum structures. In *1998 Review of Progress in Quantitative NDE*, Snowbird, Utah, Aug. 1998.

[55] Buzz Wincheski and Min Namkung. Deep flaw detection with giant magnetoresistive (GMR) based self-nulling probe. In *1999 Review of Progress in Quantitative NDE*, Montreal, Canada, July 1999.

[56] J. Wloka. *Partial Differential Equations*. Cambridge University Press, Cambridge, 1987.